

Electronic Thesis and Dissertation Repository

5-28-2021 10:00 AM

MRI of structural & functional changes associated with Western diet consumption

Lauren M. Smith, *The University of Western Ontario*

Supervisor: McKenzie, Charles A., *The University of Western Ontario*

A thesis submitted in partial fulfillment of the requirements for the Doctor of Philosophy degree in Medical Biophysics

© Lauren M. Smith 2021

Follow this and additional works at: <https://ir.lib.uwo.ca/etd>



Part of the [Medical Biophysics Commons](#)

Recommended Citation

Smith, Lauren M., "MRI of structural & functional changes associated with Western diet consumption" (2021). *Electronic Thesis and Dissertation Repository*. 7821.
<https://ir.lib.uwo.ca/etd/7821>

This Dissertation/Thesis is brought to you for free and open access by Scholarship@Western. It has been accepted for inclusion in Electronic Thesis and Dissertation Repository by an authorized administrator of Scholarship@Western. For more information, please contact wlsadmin@uwo.ca.

Abstract

The Western diet (WD) is a high-fat, high-sugar diet increasingly common in the Western world and is associated with adverse effects in many organs, though the mechanisms behind these changes are unclear. Magnetic resonance imaging (MRI) techniques that provide structural and functional information non-invasively were used to investigate the effect of the WD on the liver and placenta in a guinea pig model.

The WD leads to a manifestation of the metabolic syndrome in the liver known as non-alcoholic fatty liver disease (NAFLD). Fat-fraction MRI was used to confirm the onset of NAFLD in a guinea pig model fed a lifelong WD, and hyperpolarized [1-¹³C]pyruvate magnetic resonance spectroscopy (MRS) was used to observe abnormal pyruvate metabolism in the liver. Importantly, this study included *ex vivo* enzyme measurements that correlated with the MRS results, further validating its use in identifying potential biomarkers of metabolic disease.

While hyperpolarized MRS techniques were successfully applied in the liver, investigation of the placenta requires imaging, especially in the guinea pig where multiple fetoplacental units are common. A technical improvement to the hyperpolarized MRI acquisition technique involving an optimized flip angle scheme was shown to improve the signal-to-noise ratio, enabling it to be used more effectively for *in vivo* evaluation of pyruvate metabolism in pregnancy research.

Continuing to investigate the effect of the WD, diffusion-weighted MRI and T₂* maps were used to measure blood perfusion and oxygenation of the placenta in a guinea pig model. Lifelong maternal WD consumption led to decreased oxygen saturation in the placenta in conjunction with increased blood perfusion at mid-gestation, which eventually improved blood oxygenation in the placenta near term. Similar placental adaptations have previously been reported in other models, but this is the first study to propose a connection with maternal diet.

In conclusion, this dissertation contains applications of advanced MRI techniques to study the effect of the WD in multiple organs and provides an improved acquisition strategy for hyperpolarized MRI relevant to the study of metabolic disease. The findings presented here

validate and further motivate the use of hyperpolarized and diffusion-weighted MRI in studies of metabolic disease.

Keywords: Western diet, magnetic resonance imaging, hyperpolarized MRI, pyruvate, metabolism, intravoxel incoherent motion, oxygen saturation, proton density fat fraction, non-alcoholic fatty liver disease, placenta

Summary for Lay Audience

A high-fat and high-sugar diet, known as the Western diet (WD), is common in Western society and may lead to poor health outcomes. In this thesis, the effect of diet on the liver and placenta is investigated using magnetic resonance imaging (MRI) techniques.

The effect of diet on liver function was chosen as a focus because it is known that diets high in fat lead to the accumulation of fat in the liver and poor liver function. A specialized MRI technique was used in an animal model to investigate how diet affects the liver's ability to break down simple sugars to generate energy. It was found that guinea pigs fed a WD had fatty livers and displayed a metabolism pattern that has previously been associated with liver damage.

The MRI technique used to gain information on metabolism in the body is an emerging method that suffers from poor image quality and difficulty in image acquisition. Part of this thesis aimed to improve image quality using a modified version of this technique. The new method was shown to produce higher quality images in our guinea pig experiments.

Poor diet during pregnancy has been shown to lead to poorer outcomes for the infant. One way this happens is through placental damage that limits the placenta's ability to function properly. To measure the effect of diet on placental function, advanced MRI techniques were used to measure oxygenation and blood flow in a guinea pig model. Mothers fed a WD had less oxygen in the placenta but, interestingly, more blood flow than mothers fed a control diet. This data may suggest that the placenta recognizes the low oxygen levels associated with poor diet and reacts by increasing blood flow through the placenta in an attempt to provide the fetus with sufficient oxygen.

The research in this thesis is important for demonstrating advanced MRI techniques to study changes associated with poor diet. These results promote more investigation using these techniques that may eventually be incorporated into clinical examinations.

Co-Authorship Statement

Chapters 2, 3, and 4 of this thesis contain original research studies completed in collaboration with other authors. Acknowledgement of the contributions from myself and others to this work is described below for each project.

Chapter 2 was adapted from an original research manuscript accepted for publication in *Journal of Magnetic Resonance Imaging* in 2021 entitled “In vivo magnetic resonance spectroscopy of hyperpolarized [1-¹³C]pyruvate and proton density fat fraction in a guinea pig model of non-alcoholic fatty liver disease development after lifelong Western diet consumption”, DOI: 10.1002/jmri.27677¹. It was authored by Lauren M. Smith, Conrad B. Pitts, Lanette J. Friesen-Waldner, Neetin H. Prabhu, Katherine E. Mathers, Kevin J. Sinclair, Trevor P. Wade, Timothy R.H. Regnault, and Charles A. McKenzie. As first author, I was involved in imaging experiments, data analysis, interpretation, and preparation and submission of the manuscript. Lanette Friesen-Waldner was involved in imaging data collection and animal care. Conrad Pitts, Neetin Prabhu, and Katherine Mathers were involved in *ex vivo* tissue collection and analysis. Kevin Sinclair was involved in imaging data collection. Trevor Wade assisted with software involved in analysis of spectroscopy data. Timothy Regnault and Charles McKenzie were responsible for study conception and design and provided guidance on data interpretation and revisions of the manuscript.

Chapter 3 was adapted from an original technical development manuscript published in *Magnetic Resonance in Medicine*, Volume 83, Issue 3, pages 1510-1517, DOI:10.1002/mrm.28194. This work, entitled “Optimizing SNR for multi-metabolite hyperpolarized carbon-13 MRI using a hybrid flip-angle scheme”, was published in 2020 and authored by Lauren M. Smith, Trevor P. Wade, Lanette J. Friesen-Waldner, and Charles A. McKenzie². As first author, I was involved in study design, implementation, data collection, data analysis, interpretation, and preparation and submission of the manuscript. Trevor Wade was involved in the implementation of pulse sequence changes and data collection. Lanette Friesen-Waldner was involved in data collection and animal care. Charles McKenzie was responsible for study conception and provided guidance on revisions of the manuscript.

Chapter 4 was adapted from an original research manuscript prepared for submission to the *Journal of Magnetic Resonance Imaging* entitled “Perfusion and oxygenation of the mid-pregnancy and near-term placenta measured by magnetic resonance imaging in a guinea pig model of pregnancy following lifelong Western diet consumption” and authored by Lauren M. Smith, Lanette J. Friesen-Waldner, Conrad P. Rockel, Flavien Delhaes, Timothy R.H. Regnault, and Charles A. McKenzie. As first author, I was involved in study design, data collection, data analysis, interpretation, and preparation of the manuscript. Lanette Friesen-Waldner was involved in data collection and animal care. Conrad Rockel was involved in data collection and initial implementation of the diffusion-weighted imaging experiment. Flavien Delhaes was involved in study conception and design. Timothy Regnault and Charles McKenzie were responsible for study conception and design and provided guidance on data interpretation and revisions of the manuscript.

Dedicated to my mother and father.

Acknowledgements

It feels surreal to be at the end of my PhD journey after five years at Western in the McKenzie lab. I have so much to be thankful for, including the opportunity to work with wonderful people over the years and all the skills and lessons, both professional and personal, I've learned along the way.

I'd like to begin by thanking my supervisor, Dr. Charles McKenzie, for providing me with the opportunity to pursue a graduate degree in his lab. I feel truly lucky to have benefited from your dedicated mentorship that has been invaluable to my growth as a scientist. Thank you for sending me around the world, from Hawaii to Paris to Israel, to present my work and expand my research horizons. Thank you for encouraging me, believing in me, and for always making sure there were board games to play during Friday "meetings".

I want to thank my advisory committee members, Dr. Jean Théberge and Dr. Rob Bartha, for their enthusiasm for my work and for providing thoughtful feedback and guidance over the course of my PhD.

Next, I would like to thank Dr. Tim Regnault for sharing his vast knowledge of physiology and, despite his busy schedule, being available to answer all my questions about the guinea pig placenta. Thank you for your involvement in my work and your patience in editing my manuscripts many times over.

I would like to thank Dr. Lanette Friesen-Waldner for her support, input, advice, and friendship during my time in the lab. I enjoyed all of our conversations and laughs during the many hours spent at the MR scanner. I'll miss those little guinea pigs too.

I want to thank Dr. Trevor Wade for his technical support and patience in helping me with EPIC, as he is a pulse programming guru and also the fastest runner for our ^{13}C experiments.

I would also like to thank Cheryl vander Tuin for her vital work in providing animal care and preparation.

To all the members of the McKenzie lab, past and present, who I've had the pleasure to work alongside: Stephanie Giza, Simran Sethi, Lindsay Morris, Mary-Ellen Empey, Kevin

Sinclair, Dr. Conrad Rockel, Dr. Alireza Akbari, Amanda MacConnell, Daniel McCooney, and Dr. Takashi Hashimoto, you all made the lab a great place to be. Thank you for your friendships, collaboration, and willingness to take a walk for coffee when I didn't feel like working.

I want to thank all my family and friends for their unending support over the years, even if they didn't really understand what my research was about. Thank you KZP for providing fun nights out that let me completely forget about my PhD.

To my partner, Jason, thank you for being by my side throughout this journey and for always supporting and believing in me. Thank you for cooking all our meals when I was writing my thesis, for helping make my code run, and for dealing with my weekly freak-outs. I can't wait for our future adventures in California.

To Finnegan, I know you are a dog and cannot read this, but you helped me get through the end of this PhD. Thank you for taking me on daily walks and for giving me all the puppy kisses.

Of course, I would not have made it here without the love and encouragement of my parents, to whom I dedicate this thesis. Thank you for your unwavering support in all of my endeavours and for putting up with me when I said I wanted to go to school forever (this time I'm done for real)!

Finally, I would like to acknowledge the various sources of funding that have supported my research over the years: the Natural Sciences and Engineering Research Council of Canada (NSERC), the National Institutes of Health (NIH), the Children's Health Research Institute (CHRI), and Mitacs.

Table of Contents

Abstract.....	ii
Summary for Lay Audience.....	iv
Co-Authorship Statement.....	v
Acknowledgements.....	viii
Table of Contents.....	x
List of Tables.....	xiv
List of Figures.....	xv
List of Appendices.....	xix
List of Symbols, Acronyms, and Abbreviations.....	xx
Chapter 1.....	1
1 Introduction.....	1
1.1 Western Diet.....	1
1.1.1 Metabolic Syndrome.....	5
1.1.2 Effects of the Western Diet on the Liver.....	7
1.1.2.1 Non-alcoholic fatty liver disease.....	10
1.1.3 Effects of the Western Diet in Pregnancy.....	15
1.1.3.1 Developmental Origins of Health and Disease (DOHaD).....	16
1.1.3.2 Effects of the Western Diet on the Placenta.....	20
1.2 Guinea Pig Model.....	23
1.3 Magnetic Resonance Imaging.....	25
1.3.1 Nuclear Magnetic Resonance.....	25
1.3.2 Magnetic Resonance Spectroscopy.....	29
1.3.3 Magnetic Resonance Imaging.....	33
1.3.4 Chemical Shift-Encoded MRI.....	40
1.3.5 Diffusion-Weighted Imaging.....	43
1.3.5.1 Intravoxel Incoherent Motion (IVIM).....	47
1.3.6 T ₂ * MRI.....	50
1.3.7 Hyperpolarized MRI.....	52
1.3.7.1 Hyperpolarized Pyruvate MRI.....	57
1.4 Thesis Outline.....	61
Chapter 2.....	64

2 In vivo magnetic resonance spectroscopy of hyperpolarized [1-¹³C]pyruvate and proton density fat fraction in a guinea pig model of non-alcoholic fatty liver disease development after lifelong Western diet consumption	64
2.1 Introduction.....	64
2.2 Methods.....	65
2.2.1 Ethical Approval	65
2.2.2 Animal Model and Welfare	66
2.2.3 In Vivo Proton MRI Determination of Fat Content and In Vivo Measurements of Hepatic Metabolism with Hyperpolarized ¹³ C MRS....	67
2.2.4 Ex Vivo Hepatic Determinations	68
2.2.4.1 Triglyceride Content.....	68
2.2.4.2 Liver Cholesterol Content	69
2.2.4.3 Western Blot.....	69
2.2.4.4 Enzyme Activity Assays.....	70
2.2.5 Statistical Analysis.....	71
2.3 Results.....	71
2.3.1 Animal Body Weights and Food Intake.....	71
2.3.2 Blood Profiles Show Elevated Indicators of Liver Damage in Western Diet Animals.....	72
2.3.3 Impact of Lifelong Western Diet on Body and Organ Fat Content.....	73
2.3.4 Western Diet Feeding Results in Accelerated Hepatic Lactate Production Rate	75
2.3.5 Lifelong Western Diet Alters Body and Liver Weights	76
2.3.6 Triglyceride and Cholesterol Levels are Elevated in WD-exposed Livers	77
2.3.7 Altered PDH and LDH Activity in WD-exposed Livers	77
2.3.8 Correlations.....	79
2.4 Discussion.....	79
2.4.1 PDFF Findings Consistent with Lean NAFLD Phenotype.....	79
2.4.2 Altered Pyruvate Metabolism and Evidence of Damaged Livers Found in WD-fed Animals.....	81
2.4.3 Limitations	82
2.4.4 Conclusion	83

Chapter 3.....	84
3 Optimizing Signal-to-noise Ratio for Multi-metabolite Hyperpolarized Carbon-13 Magnetic Resonance Imaging using a Hybrid Flip Angle Scheme.....	84
3.1 Introduction.....	84
3.2 Methods.....	86
3.2.1 Simulations	86
3.2.2 msVFA Implementation and Verification	88
3.2.3 Animal Experiments	89
3.2.4 Signal-to-Noise Ratios	91
3.3 Results.....	91
3.4 Discussion and Conclusions	95
Chapter 4.....	99
4 Perfusion and oxygen saturation of the mid-pregnancy and near-term placenta measured by magnetic resonance imaging in a guinea pig model of pregnancy following lifelong Western diet consumption	99
4.1 Introduction.....	99
4.2 Methods.....	101
4.2.1 Animals.....	101
4.2.2 Imaging and Analysis	101
4.3 Results.....	102
4.3.1 Volumes and Volume Ratios	103
4.3.2 Oxygen Saturation	105
4.3.3 Placental Microstructure	106
4.4 Discussion.....	106
4.4.1 Volumes and Volume Ratios	107
4.4.2 Oxygen Saturation	108
4.4.3 Placental Microstructure	109
4.4.4 Limitations, Future Work, and Conclusions.....	111
Chapter 5.....	113
5 Conclusions.....	113
5.1 Thesis Summary.....	113
5.1.1 Significance and Impact.....	114

5.2 Future Directions	115
5.2.1 Longitudinal Studies	115
5.2.2 Diet Intervention and Exercise Studies.....	115
5.2.3 HP [2- ¹³ C]pyruvate MRI/MRS	116
5.2.4 HP ³¹ P MRI.....	117
5.2.5 Human studies.....	118
References.....	120
Appendices.....	136
Curriculum Vitae	138

List of Tables

Table 1.1: Image weighting via manipulation of TE, TR, and α^{124}	35
Table 2.1: Antibodies used in Western blot analysis	70
Table 2.2: Liver function and tissue profiles	72
Table 4.1: Fetal and placental volumes for each diet and gestational age group.....	104

List of Figures

Figure 1.1: Components of the control and Western diet used in Chapters 2 and 4 of this thesis.	2
Figure 1.2: Subcutaneous vs visceral fat storage	7
Figure 1.3: The progression of NAFLD	11
Figure 1.4: The DOHad Hypothesis	17
Figure 1.5: Representation of the net magnetization M_0 in an external magnetic field B_0	26
Figure 1.6: Graphical representation of the longitudinal (T_1) and transverse (T_2) relaxation times.....	29
Figure 1.7: Visual representation of the Fourier transform	32
Figure 1.8: Formation of a spin echo. (A) Magnetization is in the M_z direction (B) A 90° RF pulse tips the magnetization into the xy-plane (C) Spins begin to de-phase with each other (D) A 180° RF pulse is applied to flip the spins about the y-axis (E) Spins move back into phase with each other (F) An echo is formed.	34
Figure 1.9: Schematic of slice selection using an RF pulse with a bandwidth from f_1 to f_2 applied in combination with a gradient in the z-direction. Only spins within the bandwidth are selectively excited by the RF pulse.....	37
Figure 1.10: An example of a basic gradient echo pulse sequence diagram showing the slice selection (G_{SS}), phase encoding (G_{PE}), and frequency encoding (G_{FE}) gradients at work to encode the spatial location of the echo.	39
Figure 1.11: An example of the MR signal from fat and water coming in and out of phase with each other at different TEs. Images may be acquired at the TEs that correspond to the purple boxes for a two-point Dixon acquisition.	41
Figure 1.12: Semi-log plot of signal attenuation against b-value demonstrating the IVIM effect at low b-values.....	48
Figure 1.13: Graph of T_2 and T_2^* relaxation curves.....	50
Figure 1.14: Example of the enrichment of NMR-sensitive nuclei followed by hyperpolarization	55
Figure 1.15: Schematic of pyruvate metabolism highlighting the fate of the $[1-^{13}\text{C}]$ pyruvate nuclei.....	59
Figure 1.16: Venn diagram of major themes of this thesis represented in each project	62

Figure 2.1: Total volumes estimated from MRI for the whole body (A), liver (B), and hind limbs (C). WD-fed animals displayed a significantly decreased whole-body volume and increased liver volume compared to the CD-fed animals. Median PDFF percentages of the liver (D) and hind limbs (E) show a significantly elevated PDFF in the livers and lower PDFF in the hind limbs of WD-fed animals compared to CD. * indicates $p < 0.05$, **** indicates $p < 0.0001$. (F) Examples of proton-density fat fraction image slices from an animal in the CD (left) and WD (right) groups. The livers and hind limbs are outlined in red and yellow, respectively, in both images. The PDFF is visibly elevated in the WD-exposed liver, as indicated by a lighter colour, and visibly reduced in the WD hind limb. In the box-and-whisker plots, the boxes extend from the 25th to 75th percentiles, the middle line is the median, and the whiskers extend from the smallest to the largest value in the data set. 74

Figure 2.2: Adipose tissue volumes as a percentage of total body volume for the subcutaneous adipose tissue (A), visceral adipose tissue (B), and the sum of subcutaneous and visceral adipose tissue (C). The SAT+VAT as a percentage of total body volume was significantly elevated in CD-fed animals. * indicates $p < 0.05$ 75

Figure 2.3: (A) Examples of hyperpolarized $[1-^{13}\text{C}]$ pyruvate magnetic resonance spectra (left) and stack plots (right) from one CD (top) and one WD (bottom) fed guinea pig liver. Frequency is relative to the center of the pyruvate peak. Stack plots display spectra from the first 60 seconds of acquisition with a 1 second time resolution. Mean time to peak (TTP) measured from the time of the pyruvate peak for lactate (B) and alanine (C) in both diet groups. WD ($n = 13$) animals show a significant decrease in lactate TTP compared to CD ($n = 13$) animals.* indicates $p < 0.05$ 76

Figure 2.4: Liver triglyceride concentrations plotted against PDFF in the liver. There is a moderate positive correlation ($r = 0.6917$, $p = 0.0001$) between TG and PDFF for all animals. The linear fit line is shown with 95% confidence intervals. There is a non-significant weak correlation between TG and PDFF when only considering animals from the WD group ($r = 0.311$, $p = 0.301$). 77

Figure 2.5: Liver enzyme protein levels for pyruvate dehydrogenase (PDH; A), lactate dehydrogenase (LDH; B), and phosphorylated PDH (pPDH; C). Enzyme activity measured from liver tissue for PDH (D), LDH (E), and citrate synthase (CS; F). * indicates $p < 0.05$, ** indicates $p < 0.01$ 78

Figure 2.6: (A) Liver PDFF plotted against LDH activity displays a strong positive correlation ($r = 0.8289$, $p = 0.0016$). (B) Liver PDFF plotted against PDH activity displays a very strong negative correlation ($r = -0.8350$, $p = 0.0026$). (C) LDH enzyme activity plotted against lactate TTP displays a moderate negative correlation ($r = -0.6004$, $p = 0.0508$). Linear fit lines are shown with 95% confidence intervals 79

Figure 3.1: The desired flip angle trajectories for each metabolite are shown for CFA (top) and msVFA (bottom) strategies. These flip angles were achieved using a double Gaussian RF pulse. Dotted vertical lines indicate the start time of each acquisition. 87

Figure 3.2: The double Gaussian RF spectral profile used in each msVFA acquisition is shown here, centered on the pyruvate peak. The resonant frequency of each metabolite is indicated by vertical dashed lines. The magnitude and shape of the RF profile progressively changes with each acquisition to follow the msVFA trajectory. 89

Figure 3.3: The mean SNR for each metabolite averaged over all (A) placenta, (B) maternal liver, and (C) maternal kidney ROIs are plotted here. The mean SNR at each time point may be compared between msVFA (red squares) and CFA (blue circles) acquisitions. A: The increased SNR provided by the msVFA acquisition is apparent for all metabolites, except alanine. This is likely due to limited production of alanine in the placenta providing very little metabolite signal that could be increased by the use of msVFA. B: The increased SNR provided by the msVFA acquisition is apparent for pyruvate and lactate, while there is limited improvement for alanine and bicarbonate. C: There appears to be increased mean SNR using msVFA for all metabolites in maternal kidney ROIs; however, these trends were not found to be significant. Note for all ROIs, the y-axis SNR scale is larger for pyruvate due to larger amount of signal from pyruvate compared to other metabolites. 94

Figure 3.4: Typical hyperpolarized ^{13}C metabolite images overlaid on axial T_1 of the same animal at 30s post injection. Four pairs of images are shown here for each metabolite: pyruvate shown in magenta (top left), lactate in yellow (top right), alanine in green (bottom left), and bicarbonate in cyan (bottom right). For each pair of images, the image on the left was acquired using CFA and the image on the right acquired using msVFA. The image pairs have identical window and level for each metabolite. Placentae are indicated by blue arrows and outline; fetal livers are indicated by red arrows and outline. A different slice is shown for alanine and bicarbonate to show increased bicarbonate signal in the placenta using msVFA. 95

Figure 4.1: Fetal liver to fetal body (A), fetal brain to fetal body (B), fetal brain to fetal liver (C), and placenta to fetus (B) volume ratios measured for animals in each diet and gestational age group. The violin plots show the empirical distribution of the data, with a bold dashed line at the median and dotted lines at the first and third quartile. Horizontal lines indicate measurements that are different from each other, pronged horizontal lines indicate differences between gestational age disregarding maternal diet, and pronged vertical lines indicate differences between diet groups disregarding gestational age. Significance is denoted by: * $p < 0.05$, ** $p < 0.01$, and *** $p < 0.001$ 104

Figure 4.2: Mean T_2^* measurement in placentae (A), fetal liver (B) and fetal brain (C) in each diet and gestational age group. Horizontal lines indicate measurements that are different from each other, pronged horizontal lines indicate differences between gestational age disregarding maternal diet, and pronged vertical lines indicate differences between diet groups disregarding gestational age. Significance is denoted by: * $p < 0.05$, ** $p < 0.01$, and *** $p < 0.001$ 105

Figure 4.3: Mean diffusion parameters from all placentae: (A) apparent diffusion coefficient, (B) pseudodiffusion coefficient, and (C) perfusion fraction in each diet and gestational age group. Horizontal lines indicate measurements that are different from each other, pronged horizontal lines indicate differences between gestational age disregarding maternal diet, and pronged vertical lines indicate differences between diet groups disregarding gestational age. Significance is denoted by: * $p < 0.05$, ** $p < 0.01$, and *** $p < 0.001$ 106

Figure 4.4: Summary of measurements (A) in the WD group compared to CD group at MT and NT and (B) from MT to NT in CD and WD animals. The red “up” arrows indicate a decrease in the measurement, green “down” arrows indicate an increase in the measurement, and blue equals signs indicate no change in the measurement. All changes presented here are significant. 107

List of Appendices

Appendix A: Ethics Approvals	136
------------------------------------	-----

List of Symbols, Acronyms, and Abbreviations

α	Flip angle ($^{\circ}$)
γ	Gyromagnetic ratio ($\text{rad}\cdot\text{s}^{-1}\cdot\text{T}^{-1}$)
ϕ	Initial angle of the net magnetization in the transverse plane
ω_0	Larmor frequency (Hz)
^1H	Hydrogen-1
^{13}C	Carbon-13
^{15}N	Nitrogen-15
^{19}F	Flourine-19
^{29}Si	Silicon-29
^{31}P	Phosphorus-31
^{129}Xe	Xenon-129
2D	Two dimensional
3D	Three dimensional
Acetyl-coA	Acetyl coenzyme A
ADC	Apparent diffusion coefficient
ALB	Albumin
ALP	Alkaline phosphatase
ALT	Alanine transaminase
ATP	Adenosine triphosphate
ANOVA	Analysis of variance
b	b-value (s/mm^2)
B_0	Main magnetic field strength (T)
B_1	RF pulse magnetic field strength (T)
BA	Blood ammonia
BMI	Body mass index
BOLD	Blood oxygen level dependent
BUN	Blood urea nitrogen
BW	Bandwidth
CD	Control diet
CFA	Constant flip angle

CHOL	Cholesterol
CS	Citrate synthase
CSE-MRI	Chemical shift-encoded MRI
CT	Computed tomography
CVD	Cardiovascular disease
D	Diffusion coefficient (mm ² /s)
D*	Perfusion coefficient (mm ² /s)
d-DNP	Dissolution dynamic nuclear polarization
DNL	De novo lipogenesis
DOHaD	Developmental origins of health and disease
DTI	Diffusion tensor imaging
DWI	Diffusion weighted imaging
EPI	Echo planar imaging
ETL	Echo train length
f	Perfusion fraction
FFA	Free fatty acid
FGR	Fetal growth restriction
FID	Free induction decay
fMRI	Functional MRI
FOV	Field of view
FT	Fourier transform
GE	Gradient echo
G _{FE}	Frequency encoding gradient
GGT	Gamma glutamyl-transferase
G _{PE}	Phase encoding gradient
G _r	Gradient applied along the r direction (mT/m)
G _{SS}	Slice selection gradient
HDL	High-density lipoprotein
HP ¹³ C MRI	Hyperpolarized carbon-13 MRI
HP MRI	Hyperpolarized MRI
HPA	Hypothalamic-pituitary-adrenal

IDEAL	Iterative decomposition of water and fat with echo asymmetry and least-squares estimation
IVIM	Intravoxel incoherent motion
LDH	Lactate dehydrogenase
LDL	Low-density lipoprotein
LGA	Large for gestational age
M_0	Net magnetization
MAFLD	Metabolic dysfunction-associated fatty liver disease
MetS	Metabolic syndrome
MRI	Magnetic resonance imaging
MRS	Magnetic resonance spectroscopy
msVFA	Multi-spectral variable flip angle
MT	Mid-term
MUFA	Monounsaturated fatty acids
M_{xy}	Transverse magnetization
M_z	Longitudinal magnetization
NAD ⁺	Nicotinamide adenine dinucleotide
NADH	Nicotinamide adenine dinucleotide + hydrogen
NAFLD	Non-alcoholic fatty liver disease
NASH	Non-alcoholic steatohepatitis
NEX	Number of excitations
NMR	Nuclear magnetic resonance
NT	Near-term
PD	Proton density
PDFF	Proton density fat fraction
PDH	Pyruvate dehydrogenase
PET	Positron emission tomography
pH	Power of hydrogen
PHIP	Parahydrogen induced polarization
PN	Postnatal
pPDH	Phosphorylated pyruvate dehydrogenase
ppm	Parts per million

PRESS	Point resolved spectroscopy
PUFA	Poly-unsaturated fatty acid
RF	Radiofrequency
ROI	Region of interest
SABRE	Signal amplification by reversible exchange
S	MRI signal
S ₀	Original MRI signal
SAT	Subcutaneous adipose tissue
SE	Spin echo
SEOP	Spin exchange optical pumping
SFA	Saturated fatty acid
SGA	Small for gestational age
SNR	Signal-to-noise ratio
T	Tesla
T ₁	Longitudinal relaxation time
T ₂	Transverse relaxation time
T ₂ *	Apparent transverse relaxation time
TBIL	Bilirubin
TCA	Tricarboxylic acid
TE	Echo time
TG	Triglyceride
TR	Repetition time
TTP	Time-to-peak
US	Ultrasound
VAT	Visceral adipose tissue
VFA	Variable flip angle
WD	Western diet

Chapter 1

1 Introduction

This introductory chapter provides information necessary to understand topics related to the following chapters of the thesis. A definition of the Western diet (WD) is provided with insight into the impact of the WD on the liver and placenta, two systems studied in detail in Chapters 2 and 4. Magnetic resonance imaging (MRI) techniques used in this thesis are explained in adequate detail for the reader to appreciate the technical details, advantages, and limitations of these imaging strategies.

1.1 Western Diet

The increasing trend of obesity and metabolic syndrome in North American society is due in part to the high-fat and high-sugar diets common to the Western world, referred to as the “Western diet” (WD) in this thesis. Hallmarks of the WD include high glycemic load, fatty acid composition, macronutrient composition, micronutrient density, acid-base balance, fibre content, and sodium-potassium ratio³. There is a theory that humans were not able to genetically adapt quickly enough to the changes in diet and lifestyle that began with the rise of agricultural society, and these changes over time have led to an increased incidence of chronic metabolic diseases observed in modern societies³. This concept is related to the hypothesis of a “thrifty phenotype” where the human body evolved to preserve glucose via insulin resistance in times of food deprivation and develop a robust immune system to defend against infectious disease⁴. In the absence of our ancestors’ survival pressures, physiological stress may cause these adaptations to instead lead to the development of Western metabolic diseases, due in part to establishing a state of chronic metabolic inflammation^{4,5}. This chronic inflammation may be related to structural and behavioural changes to the microbiome brought on by WD consumption, highlighting the complex and multifaceted nature of the body’s response to the WD⁶. The WD may also impact sex steroids which regulate both reproductive function and energy metabolism, potentially contributing to reproductive conditions such as hypogonadism and sex hormone imbalance⁷. Many chronic non-communicable diseases in Western

societies can be partially attributed to diet, including diabetes, hypertension, obesity, cardiovascular disease (CVD), osteoporosis, and cancer³. This post-agricultural diet primarily consists of foods humans have not evolved to consume, including dairy products, cereal grains, refined sugars, refined vegetable oils, excess salt, and alcohol. The WD is energy-dense, emphasizing saturated fats and simple sugars as a primary energy source with low nutritional quality⁸. Studies have shown that diet composition is more important than caloric intake in the risk of developing metabolic syndrome⁹. Western diets, high in processed food, red meat, and sugar, have been associated with an increased risk of metabolic syndrome, even when controlled for other factors such as age, sex, education, physical activity, and body mass index (BMI)⁹.

In this thesis, I focus on the fatty acid composition, glycemic load, macronutrient composition, and micronutrient density aspects of the WD, using a diet particularly high in fat and sugar. The main aspects of the WD presented here that affect physiology are increased saturated fatty acids and significant fructose content, as seen in Figure 1.1.

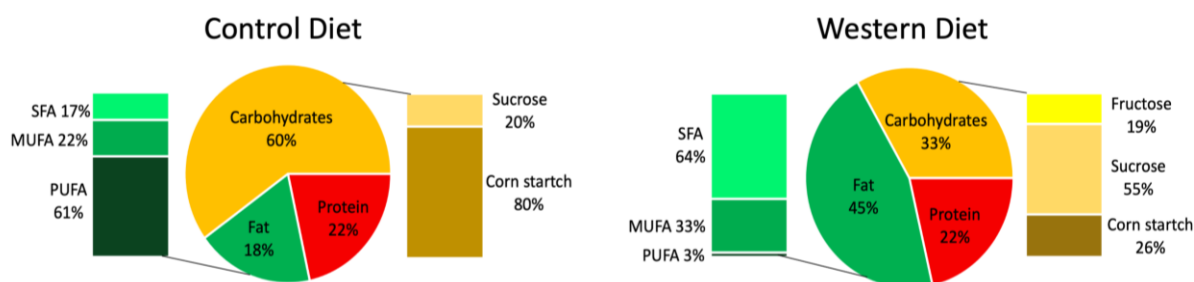


Figure 1.1: Components of the control and Western diet used in Chapters 2 and 4 of this thesis.

Dietary fat can primarily be categorized as triglycerides (TG), which are three fatty acid molecules bound to a single glycerol molecule. Fatty acids fall into three categories: saturated fatty acids (SFAs), monounsaturated fatty acids (MUFAs) and polyunsaturated fatty acids (PUFAs). Current evidence suggests that the risk of chronic disease is more impacted by the type of fat than the absolute amount of dietary fat, as MUFAs and some PUFAs are more beneficial than SFAs and trans fatty acids, which are detrimental in excessive quantities. Trans fatty acids, particularly industrial trans fatty acids found in fast foods and baked goods, increase cardiovascular disease risk through proinflammatory properties⁴. The WD contains excessive SFA and trans fatty acids,

which increase the risk of CVD by elevating blood concentration of total cholesterol and low-density lipoprotein (LDL) cholesterol. High cholesterol has been associated with arterial lesions and may contribute to the risk of CVD⁴. High-fat diets, particularly those high in SFAs, can induce weight gain, insulin resistance, and hyperlipidemia¹⁰.

The overconsumption of sugar is associated with obesity, non-alcoholic fatty liver disease (NAFLD), insulin resistance, and CVD¹¹. Glycemic load is the potential of a food to increase blood glucose levels based on the quality and quantity of dietary carbohydrate³. Carbohydrates with high glycemic loads elevate TGs and small-dense LDLs while reducing high-density lipoprotein (HDL) cholesterol³. High glycemic load diets also promote C-reactive protein, which is an inflammatory marker and may be a strong predictor of CVD³. Refined sugar products have high glycemic loads that lead to elevations in blood glucose and insulin concentrations after repeated exposure. In the long term, these changes may result in adverse metabolic effects that promote insulin resistance through hormonal and physiological changes. Though glycemic load is a helpful measure related to insulin resistance, it is not always an indication of “healthy” foods. For example, fructose has a low glycemic load but is known to induce insulin resistance. This may be due to its ability to cause a shift in balance from oxidation to the esterification of free fatty acids, which other sugars cannot do³.

The liver takes up fructose rapidly, where it is phosphorylated and may be used to produce glucose, glycogen, lactate, and pyruvate¹⁰. Fructose also plays a role in increasing hepatic gluconeogenesis and *de novo* lipogenesis (DNL), leading to increased plasma glucose, TG levels, and blood pressure^{12,13}. Compared to glucose, fructose consumption results in a larger production of lactate¹³, which is related to liver damage and other conditions¹⁴. Long-term exposure to a high fructose diet can cause muscle tissue to increase fatty acid oxidization and lead to decreased uptake and oxidation of glucose¹⁵. Fructose lowers insulin and leptin blood concentrations, which increases the likelihood of weight gain and associated metabolic consequences¹⁰. Insulin resistance, impaired glucose tolerance, adiposity, and hypertension result from high fructose diets in animal models¹⁰. All this considered, the full metabolic effects of dietary fructose in humans remain unclear, though existing data suggests fructose may be detrimental in

terms of body weight, adiposity, and metabolic disease¹⁰. The use of non-invasive techniques such as magnetic resonance spectroscopy (MRS) and MRI will allow us to learn more about the metabolic influence of high fructose dietary consumption¹⁵.

The macronutrient composition of a diet also affects physiology and is a hallmark of the Western diet³. The three major macronutrient groups are carbohydrates, fat, and protein. To maintain a healthy diet, the World Health Organization recommends that fat should not exceed 30% of total energy intake, with protein maintained at 15%¹⁶. Although it is difficult to determine the historical macronutrient composition of our hunter-gatherer ancestors' diets, it is likely humans evolved eating significantly elevated portions of protein (19-35%) with fewer carbohydrates (22-40%) compared to typical diets of today³. There is evidence that high-protein diets are beneficial for a variety of reasons. One of these benefits is the improvement of blood lipid profiles, associated with lowering CVD risk. High-protein diets also decrease LDL cholesterol while increasing HDL cholesterol. Dietary protein has been linked to improvements in glucose and insulin metabolism in individuals with diabetes and lower blood pressure. Lastly, protein has a higher satiety value than fat or carbohydrates, so a high-protein diet may reduce caloric intake and be effective as a weight-loss strategy for individuals at risk due to being overweight or obese³.

This section has highlighted aspects of the WD relevant to the studies presented in this thesis; however, there are additional aspects to the WD. These include low micronutrient density, where refined sugars and foods are void of essential vitamins and minerals. The replacement of nutrient-dense foods (fruit, vegetables, lean meats, seafood) with less nutrient-dense foods (refined sugars, grains, vegetable oils, dairy products) in the modern WD exacerbates the failure to meet the daily micronutrient requirements. The acid-base balance of the diet also impacts health as a typical WD has net acidity, leading to chronic, low-grade metabolic acidosis over time. In contrast, pre-agricultural diets tended to be base yielding. Another factor of the WD is the sodium-potassium ratio. Modern WDs typically have a higher sodium content than potassium content due to the addition of manufactured salt to foods and the displacement of potassium-rich foods with refined oils and sugars. These factors cause the WD to be high in sodium and low in potassium, the

inverse of our prehistoric ancestors' diets. Lastly, the fibre content in the WD is significantly lower than recommended values (15.1g/d vs 25-30g/d). Soluble fibres, found in fruits and vegetables, have been found to reduce total and LDL cholesterol³.

1.1.1 Metabolic Syndrome

Metabolic syndrome (MetS), also known as syndrome X or the insulin resistance syndrome, is a collection of metabolic abnormalities that include insulin resistance, visceral adiposity, atherogenic dyslipidemia, and endothelial dysfunction¹⁷. Elevated levels of TGs and small-dense LDL and decreased levels of HDL cholesterol define atherogenic dyslipidemia¹⁸. The small-dense LDL are susceptible to oxidation and promote atherosclerotic plaque formation, related to increased CVD risk⁴. The features of MetS are interrelated, and the presence of more than one metabolic abnormality is necessary for the diagnosis of metabolic syndrome. MetS is related to the shared pathophysiological mechanisms of these abnormalities that may not be present in cases of isolated symptoms¹⁷. Globally, it is estimated that 20-25% of the adult population has metabolic syndrome, which increases the lifetime likelihood of diseases such as stroke, heart attack, and type II diabetes¹⁹. These conditions cause shortened lifespans in otherwise healthy individuals and contribute to socioeconomic pressure on regions with ageing populations⁵. Diet-related chronic diseases are the largest cause of morbidity and mortality in most Western countries³. Though metabolic syndrome has a broad definition and is difficult to diagnose, screening variables can be used to identify individuals at risk, including waist circumference, BMI, the concentration of TGs and HDL cholesterol in the blood, fasting glycemia, and blood pressure²⁰. Waist circumference is a more accurate variable to use instead of BMI to highlight the specific impact of visceral adipose tissue (VAT), which results in a combination of factors that are not always present in all individuals that are overweight or obese. While MetS is associated with poor diet, there has not been a single aspect of the diet identified as a sole risk factor for MetS. Instead, MetS is a result of the complex interactions of multiple nutritional factors characteristic of the WD³.

While obesity is closely related to metabolic syndrome, there are also incidences of lean (BMI < 25 kg/m²) individuals who are not metabolically healthy⁹. It is important to consider that obesity, measured by BMI, is not a necessary criterion for metabolic syndrome, even though it is commonly used as part of the description of metabolic syndrome⁹. A study investigating ~800 young adults and the link between diet quality and MetS found that almost a third of the metabolically healthy group was overweight or obese while almost a third of individuals with MetS had a normal weight as defined by BMI⁹. A similar prevalence of lean individuals with MetS has been previously reported and is likely to rise with the increasing consumption of the WD in Western society²¹. Individuals who are lean but have MetS are at a higher risk of developing diabetes, coronary heart disease, and stroke than individuals who are obese but metabolically healthy⁹. The cause of this lean MetS phenotype may be related to high volumes of VAT that are not easily measured using traditional anthropometric methods such as BMI, which does not provide information about fat distribution in the body⁹. Thus, common clinical assessments of obesity do not fully identify the risk associated with VAT in diagnoses. High volumes of VAT are associated with increased metabolic risk and may represent dysfunctional adipose tissue that cannot store energy excess appropriately^{20,22}. Although both VAT and subcutaneous adipose tissue (SAT) are associated with metabolic syndrome, VAT is more strongly related to an adverse metabolic risk profile regardless of BMI or waist circumference (Figure 1.2)²². The metabolically active nature of VAT may explain this result. VAT secretes vasoactive substances such as inflammatory markers, adipocytokines, and growth factors that can increase cardiometabolic disease risk and drain directly into the liver^{22,23}. Visceral obesity may also be a marker of defective fat being distributed between the adipose tissue, skeletal muscle, liver, and heart²⁰. VAT is a unique pathogenic fat deposit, and measuring its volume with imaging can provide additional information about the risk of metabolic disease compared to solely BMI and waist circumference measurements²². To accomplish this, imaging modalities including ultrasound, x-ray, CT, MRI, and PET can be used to quantify regional fat deposits with varying degrees of accuracy²⁴.

The importance of VAT in the context of metabolic disease highlights the need to recognize biomarkers of metabolic health that are independent of obesity. Related to this, diet quality, rather than caloric intake, is possibly a more important factor in the development of metabolic syndrome²². Poor diet quality, evident in the WD, is associated with increased risk of metabolic syndrome^{25,26} and may be used as a predictor of metabolic health independent of body size and fat content measured by BMI⁹. People with metabolic syndrome are more likely to consume a WD and have poor diet quality than metabolically healthy people across all BMI categories⁹. It has been suggested that the excessive consumption of sugar and saturated fatty acids can trigger pathogenic mechanisms while not affecting adiposity, leading to a lean metabolically unhealthy phenotype in individuals who can maintain a healthy energy balance while still suffering from increased risk of metabolic and cardiovascular disease⁹.



Figure 1.2: Subcutaneous vs visceral fat storage

As stated above, metabolic syndrome is a multifaceted collection of diseases with diverse effects on physiology and is strongly linked to modern WD trends in the developed world. Below, I will discuss the effects of the WD on the body systems focused on in this thesis.

1.1.2 Effects of the Western Diet on the Liver

The liver is a vital organ that regulates TG and cholesterol metabolism, among other functions²⁷. Perhaps the most evident structural change in the liver caused by poor diet quality is fat accumulation, otherwise known as steatosis²⁸. Steatosis gives rise to the NAFLD spectrum, discussed in section 1.1.2.1. The WD, inherently high-fat and calorie-

dense, typically results in weight gain, which generally drives hepatic fat accumulation, though this trend is not present in the proportion of metabolically healthy obese individuals²⁹. Hepatic fat accumulation is a result of an imbalance between lipid deposition and removal in the liver²⁹. Lipid intake, TG secretion, DNL, and mitochondrial fatty acid oxidation are the main factors that influence hepatic lipid accumulation and are themselves impacted by external factors including diet²⁷. The amount of dietary fat consumed has a positive correlation with liver fat content³⁰. Synthesis of TG in the liver is a mechanism used to store cytotoxic free fatty acids (FFAs)²⁹; however, excess TG forms lipid droplets in hepatocytes that contribute to metabolic abnormalities²⁸. Vessels of fat accumulate in the liver within hepatocyte cells, displacing the cytoplasm and eventually the nucleus to the edge of the cell³¹. FFAs are introduced into the liver from the diet, lipolysis of visceral fat, and DNL – the process by which excess carbohydrates are converted into fatty acids²⁹. Excessive FFAs in the liver may result from insulin resistance, which is associated with obesity, type 2 diabetes, and the WD^{28,29}. If the liver's capacity to handle carbohydrates and fatty acids is overwhelmed, toxic lipid species can accumulate in the liver and induce hepatocellular stress, injury, and death²⁸. Fibrogenesis and predisposition to cirrhosis and hepatocellular carcinoma are long-term consequences of this devastated state²⁸.

The high-sugar WD contains glucose and fructose that both synthesize fatty acids via DNL²⁹. Fructose, in particular, has a large impact on hepatic fat accumulation as fructose is shunted to the liver and undergoes unregulated DNL, contributing to increased liver fat and cellular stress^{29,32}. Like fructose, alcohol and carbohydrates tend to be converted into fat in the liver⁴. Diets rich in MUFA and PUFA tend to reduce liver fat, whereas the WD is high in SFAs and leads to increased liver fat²⁹. Exposure to the WD has been shown to induce pronounced steatosis and fibrosis in the liver of mice³³. In a study using a rat model of pre-steatosis, animals exposed to the WD showed a larger number of lipid droplets with larger diameters than those fed a control diet, though there were no macroscopic histological differences observed at this stage³⁴. In this pre-steatosis model of NAFLD, the WD was shown to increase cholesterol and the concentration of enzymes involved in the synthesis of TG, fatty acids, and cholesterol³⁴. This study provided evidence that DNL, TG, LDL cholesterol, and body weight are increased early in

NAFLD disease progression following exposure to the WD³⁴. In the same study, the WD was found to increase hepatic cells involved in fibrosis, as well as aspartate aminotransferase and bilirubin levels, both indicators of liver disease³⁴. Fibrosis, a symptom of advanced NAFLD, is the accumulation of extracellular matrix in the liver and may lead to cirrhosis, portal hypertension, and liver failure²⁸. Fibrogenesis is driven by signalling from stressed or injured hepatocytes and leads to the rapid production of matrix proteins that cannot be degraded as rapidly, leading to their accumulation in the liver²⁸.

Aside from altering liver architecture, several functional changes to the liver are also associated with the WD. In a mouse model, the WD was shown to increase inflammatory cell infiltration and proinflammatory gene expression in the liver³³. The presence of steatosis is strongly associated with chronic inflammation in the liver, and steatosis induced by a high-fat diet has been shown to elevate the hepatic expression of inflammatory cytokines³⁵. A fructose-rich WD has been shown to induce hepatic inflammation and significantly increase markers of fibrogenesis in a mouse model³⁶. Excessive fructose intake causes a gut microbiota imbalance, triggering macrophages in the liver²⁷. A high-fat diet is associated with mitochondrial dysfunction, which results in increased production of reactive oxygen species, leading to issues including oxidative stress and cell damage³⁷. Chronic exposure to the high-fat, high-fructose WD has shown to result in an imbalance of antioxidants, causing oxidative stress and contributing to liver damage in a mouse model³⁸. WDs lead to an increase in endoplasmic reticulum stress in the liver, which causes hepatocyte apoptosis and contributes to the development of hepatic steatosis^{39–41}. Oxidative stress contributes to inflammation and fibrogenesis in the liver, which ultimately results in the development of non-alcoholic steatohepatitis (NASH)⁴². These changes also likely play a key role in the inhibition of fatty acid oxidation³⁷. Fructose causes immediate increases in pyruvate and lactate production in the liver, as it is rapidly taken up and metabolized in the liver⁹. Additionally, long-term exposure to a high fructose diet results in a decreased ability to metabolize glucose in the liver¹⁵.

It is important to note that a diet high in fat, not necessarily a WD, is known to cause simple steatosis, insulin resistance, and expansion of adipose tissue in the liver but is unlikely to induce hepatic inflammation and fibrosis²⁷. On the other hand, diets high in fat and high in fructose, components of a typical WD, induce a more serious pathology of NAFLD, including extensive inflammation, fibrosis, and liver injury in addition to steatosis^{27,39}. Dietary cholesterol exacerbates the accumulation of free cholesterol in the liver and is an independent risk factor for the development of NASH and hepatocellular carcinoma²⁷. It is hypothesized that in addition to steatosis, multiple “hits” to liver health, including oxidative stress, endoplasmic reticulum stress, mitochondrial dysfunction, insulin resistance, inflammation, and gut microbiota imbalance, all potentially impacted by the WD, drive the progression of NAFLD into NASH and carcinoma²⁷. Most of the evidence for the pathogenesis of diet-induced NAFLD comes from animal studies with limitations in representing the full spectrum of disease⁴³. More accurate models and further research is warranted to elucidate details surrounding the mechanisms of these architectural and functional changes⁴³.

1.1.2.1 Non-alcoholic fatty liver disease

Non-alcoholic fatty liver disease is defined by fat accumulation in the liver exceeding 5-10% of the total liver weight³¹. NAFLD differs from alcoholic-related fatty liver disease as individuals with NAFLD accumulate fat in the liver in the absence of alcohol abuse, though the distinction between these definitions is controversial as there is no universally accepted threshold for alcohol consumption³¹. The prevalence of NAFLD is increasing globally with an estimated worldwide prevalence of ~25%²⁸ and is the most common cause of chronic liver disease in the Western world^{31,44}.

NAFLD exists on a spectrum of liver disease and may progress to NASH and eventually liver fibrosis, cirrhosis, failure, or hepatocellular carcinoma, as seen in Figure 1.3³¹. Hepatic steatosis is the primary indicator of NAFLD and involves vesicles of fat, primarily TGs, accumulating within hepatocytes without causing scarring, inflammation, or cell death^{31,45}. Steatosis may be either macrovesicular (related to an imbalance of hepatic synthesis and export of lipids) or microvesicular (related to defects in

mitochondrial function)³¹. NAFLD is generally considered benign²⁸, though patients with NAFLD have greater overall mortality than healthy populations⁴⁵. NAFLD may exacerbate previous liver damage caused by alcohol, industrial toxins, or hepatotropic viruses³¹. Fatty livers are the most common symptom of the NAFLD spectrum, and only a percentage of patients experience progression of disease to advanced fibrosis (~20%) and cirrhosis (~3%)³¹, though methods of identifying this progression remain challenging²⁸. NASH, a more advanced stage of NAFLD, is defined by inflammation (hepatitis) and hepatocyte damage in addition to steatosis^{28,31} and has an increased liver-related mortality rate⁴⁵ and risk of disease progression to cirrhosis (~21-16%)⁴⁴. Hepatocellular ballooning is a key feature of NASH associated with cell swelling and rounding of the cytoplasm²⁸. At the most extreme end of the spectrum, progressive fibrosis and cirrhosis in the liver cause irreversible damage and significantly increase the risk of developing hepatocellular carcinoma³⁵. Unlike other liver diseases, a large percentage of NASH patients develop hepatocellular carcinomas before cirrhosis and routine cancer screening²⁸. Features of NASH and advanced fibrosis are associated with a worse prognosis compared to individuals with just steatosis³¹. At this point, there is no longer fat accumulating in the liver, and the steatosis may disappear³¹. NAFLD can be further described by grade (severity) and stage (degree of fibrosis) to clearly express the progression of disease³¹.

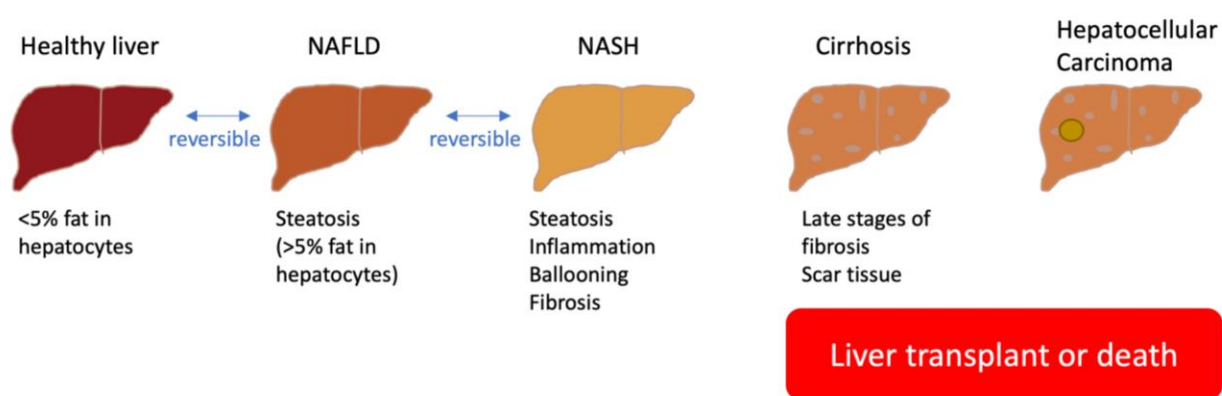


Figure 1.3: The progression of NAFLD

The majority of NAFLD patients are asymptomatic, and when symptoms do occur, they are usually non-specific³¹. Many NAFLD patients display normal lab profiles and may

progress to liver cirrhosis undiagnosed²⁸. Liver enzyme levels of aspartate aminotransferase and alanine aminotransferase (ALT), measured via blood test, are abnormal in patients with NAFLD, but the degree and patterns of these changes are nonspecific and cannot reliably be used to distinguish between NAFLD and NASH²⁸. Additionally, liver enzymes can be intermittently normal during any NAFLD stage and do not correlate with the degree of steatosis or fibrosis²⁸. Cytokeratin-18 fragment level is another serum biomarker related to hepatocyte apoptosis that has been externally validated but displays only modest accuracy in identifying NASH^{46,47}. Non-invasive imaging using ultrasound (US), computed tomography (CT), or MRI may be used to detect fat in the liver with limited sensitivity³¹. US and CT can reliably detect liver fat of >20% liver mass which may not be sensitive enough for detection of NAFLD in patients with a lesser degree of steatosis^{28,31}. MRI is a more sensitive technique, able to detect fat as little as 5% liver mass and is considered the gold standard to quantify hepatic steatosis^{28,47}. Liver stiffness measurements using US (Fibroscan) or MRI (elastography) show promise in estimating the presence of fibrosis, with MR elastography being the most accurate but limited by cost and availability^{46,47}. No imaging technique can reliably distinguish simple steatosis from NASH or distinguish between NASH cases with and without fibrosis, limiting the use of imaging for diagnosing the severity of disease³¹. Liver biopsy is the most reliable diagnostic technique for NAFLD and can identify steatohepatitis and fibrosis, making it the only accurate technique for diagnosing NASH⁴⁵. While biopsy remains the gold standard for NASH diagnosis, it is limited by cost, sampling error, and biopsy-related morbidity and mortality⁴⁵. Considering these limitations, the diagnostic value of liver biopsy in routine clinical practice is debated since most patients with NAFLD have a good prognosis, and there is a lack of established, effective therapy for the NAFLD-spectrum of disease³¹. Research and clinical trials currently focused on identifying novel serum biomarkers and developing imaging techniques to diagnose and monitor NASH may ultimately negate the need for liver biopsy in the future²⁸.

There are multiple causes of NAFLD, ranging from genetic risk factors to health-related behaviour³¹. Further, the heterogeneity in the clinical presentation of NAFLD is likely influenced by many factors, including age, sex, ethnicity, diet, alcohol use, environmental

pollutants, microbiota, metabolic health, and epigenetics^{28,48}. Chapter 2 is focused on diet-related NAFLD and uses a high-fat, high-sugar Western diet to promote fatty livers in a guinea pig model. Metabolic dysfunction-associated fatty liver disease (MAFLD) has recently been proposed as a more accurate term to describe NAFLD associated with metabolic dysfunction⁴⁸. This proposed MAFLD nomenclature should be used to describe disease in patients with evidence of hepatic steatosis in addition to the presence of overweight/obesity, type 2 diabetes mellitus, or metabolic dysregulation⁴⁹. This nomenclature allows for a more comprehensive definition of the disease, recognizes a greater number of patients at risk of disease progression, and encourages holistic treatment that focuses on the overall metabolic health of the patient instead of solely liver function⁵⁰. While we recognize the purpose of the MAFLD definition and its relevance to work in this thesis, we will continue to use the term NAFLD to define the disease as it is more generally recognized and we have not confirmed evidence of metabolic dysregulation, as defined by Eslam et al., in our guinea pig model.

Diets high in fructose, sucrose, and saturated fats, combined with sedentary lifestyles, have been associated with NAFLD²⁸. One particular aspect of the WD that may contribute to NAFLD development is fructose consumption, as fructose has been shown to promote DNL in the liver, where DNL is the enzymatic pathway that converts dietary carbohydrates into fatty acids and eventually TGs⁵¹. Dietary factors not related to the Western diet, including protein-calorie malnutrition, starvation, and rapid weight loss, have also been reported as secondary causes of steatosis³¹.

NAFLD is a manifestation of the metabolic syndrome and is frequently associated with obesity (particularly central abdominal obesity), dyslipidemia, and insulin resistance^{31,44}. The rising incidence of NAFLD mirrors the rising prevalence of obesity and type 2 diabetes worldwide⁴⁴, and these diseases were found to be independent predictors of fibrosis and cirrhosis in NAFLD patients³¹. The presence of MetS is a strong predictor of steatohepatitis in NAFLD patients and could be used to identify patients who would benefit from a liver biopsy⁴⁵. The relationship between MetS and the NAFLD spectrum is possibly bi-directional as NAFLD has been found to enhance features of MetS such as hypertension²⁸. The NAFLD spectrum has a substantial impact on cardiovascular disease,

and surprisingly the most common cause of death in these patients is CVD-related⁴⁵, followed by malignancy and then liver disease²⁸.

Due to the relationship between NAFLD and obesity and the lack of sensitive non-invasive diagnostic tests, NAFLD is often diagnosed on a presumptive basis when liver enzyme abnormalities are noticed in overweight or obese individuals³¹. It should be noted that liver enzyme abnormalities are not consistent in all patients with NAFLD and often present differently in lean patients, limiting the reliability of this diagnostic measurement²⁸. Because of this, NAFLD patients in the normal BMI range (18.5-25 kg/m²) represent a lean phenotype of NAFLD that is underrecognized⁵², despite making up a significant percentage of patients with NAFLD (~15-20%)^{48,53}, NASH (~60%) and fibrosis (55%)⁵⁴. This underdiagnosis of lean NAFLD may contribute to increased mortality reported in these patients compared to their overweight or obese counterparts⁵⁵. Lean NAFLD patients do not display the same risk factors of NAFLD, with lower insulin resistance levels and ALT but increased lobular inflammation compared to overweight/obese individuals, making the lean phenotype more difficult to diagnose⁵². In Chapter 2 of this thesis, the effect of the WD on the liver is investigated in a lean phenotype of NAFLD using MRI to contribute to the identification of biomarkers associated with this disease in lean individuals.

Simple steatosis in early-stage NAFLD is reversible with diet intervention and gradual weight loss³¹, though rapid weight loss can lead to liver damage and should be avoided⁵⁶. Although there is currently no proven effective therapy for NASH, research into pharmacological treatments is advancing rapidly, and numerous clinical trials are underway^{28,31}. Treatment targets include hepatic metabolism, cell stress and apoptosis, immune response, fibrosis, the microbiome, and combination therapies²⁸. Antioxidants, insulin-sensitizing drugs, lipid-lowering drugs, and ursodeoxycholic acid are examples of pharmaceutical treatments being investigated for use in NAFLD, though their efficacy and mechanisms of action require further study³¹. A challenge of this research is assessing the survival benefit in patients with pre-cirrhotic disease as they are not usually at risk for short-term adverse outcomes²⁸. The interconnected relationship of NAFLD and

MetS suggests therapeutic interventions may alleviate symptoms and features of both diseases²⁸.

1.1.3 Effects of the Western Diet in Pregnancy

As of 2018, 22.7% of child-bearing-aged women (18-34) were obese according to the clinically relevant BMI definition¹⁵. A significant contributor to obesity is the regular consumption of a high-fat and high-sugar Western diet⁵⁷. Diets high in saturated fats, refined carbohydrates, and low nutrient-dense foods were found to be commonly consumed by pregnant women in America⁵⁸. This finding is especially relevant in Western society as an increasing number of people are obese, accounting for 16% of pregnant mothers in Canada between 2009-2011⁵⁹. Mothers who are obese experience a higher rate of stillbirth^{60,61} and are at higher risk for maternal and fetal complications than mothers with a normal BMI^{62,63}. WD consumption also contributes to the risk of folate deficiency⁶⁴, abnormal fetal brain development⁶⁵, and fetal predisposition to type II diabetes⁶⁶.

It has been hypothesized that WD consumption, which leads to obesity and MetS, harms placental function during pregnancy⁶⁷. Mothers with MetS exhibit a higher risk of impaired fetal growth and intrauterine fetal death⁶⁷. Animal studies have shown that consumption of high-fat diets during pregnancy can lead to many issues for offspring, including but not limited to cardiovascular dysfunction, mitochondrial abnormalities⁶⁸, and the development of type II diabetes⁶⁹. Metabolic syndrome has also been shown to increase the risk of placental dysfunction and pre-eclampsia, with individuals exhibiting a higher number of MetS characteristics having a higher risk of placental dysfunction⁶⁷. The placenta is responsible for transferring nutrients from the maternal blood to fetal blood and excretion from the fetus back to the mother⁷⁰. Any disruption to these functions may lead to adverse outcomes for the fetus.

Placental dysfunction is the leading cause of stillbirth, with rates of approximately 8/1000 pregnancies in Canada⁷¹. Clinical studies have found that placental dysfunction can lead to major morbidities and is a primary cause of fetal growth restriction (FGR)^{72,73}. Further details of the fetal consequences of FGR are explained in Section 1.1.3.1. Chronic

hypoxia and hypoglycemia are also outcomes of placental insufficiency, with hypoxia being related to failed oxygen transfer between the placenta and fetus^{73,74}. Finally, metabolic dysfunction in the placenta could lead to a buildup of excess lactic or carbonic acid relative to homeostasis, leading to abnormal changes in placental pH and eventually fetal acidosis⁷⁴.

1.1.3.1 Developmental Origins of Health and Disease (DOHaD)

The developmental origins of health and disease (DOHaD), also known as the fetal origins hypothesis, suggests that the environment a fetus is exposed to *in utero* impacts the lifelong health of the individual⁷⁵. Specifically, the theory states that adverse influences in early development may result in permanent changes in individuals' physiology and metabolism that predispose them to non-communicable diseases later in life (Figure 1.4)⁷⁶. This approach evolved from the Barker hypothesis, first proposed by Dr. David Barker in the 1980s after studying correlations between low birth weight and incidence of coronary heart disease⁷⁷. The theory relies on assumptions that fetal adaptations persist into adulthood, are latent for long periods, and are caused by genetic programming due to the *in utero* environment⁷⁵. Undernutrition is one of the main maternal factors involved in the fetal origins hypothesis and is believed to lead to fetal programming that increases the future risk of developing metabolic disease in adulthood⁷⁸. Birth weight, an early focus of DOHaD research, has been shown to have a direct correlation with adult BMI that has been demonstrated in more than 20 studies⁷⁹. Though details on the mechanisms underlying fetal programming are unclear and warrant further research, the "thrifty phenotype hypothesis" (introduced in Section 1.1) is believed to contribute to this increased risk of MetS with age⁸⁰. It is proposed that genetic adaptations which promote *in utero* survival in instances of maternal undernutrition limit fetal growth and impair glucose uptake, promoting the adverse risk of metabolic diseases after birth when the individual has access to sufficient nutrition⁸⁰. Other possible mechanisms behind DOHaD include altered phenotypes from epigenetic changes in specific genes, altered microbiota, and the effect of an intrauterine stress response on neuroendocrine pathways that regulate metabolism and vasculature^{76,81}. It should be noted that adverse events during pregnancy may affect two generations, as genetic

information for reproduction is already present in the developing fetus and may also be affected by fetal programming⁷⁶.

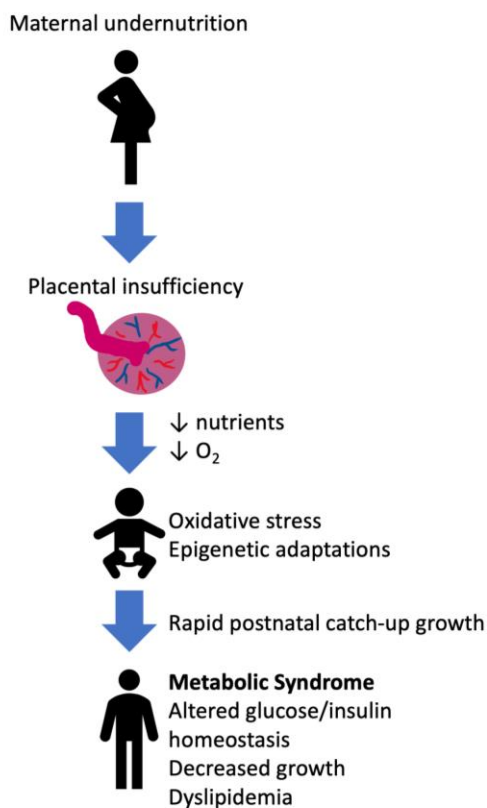


Figure 1.4: The DOHaD Hypothesis

Since its initial inception, DOHaD has been expanded to investigate a variety of *in utero* environmental pressures that influence the risk of developing a multitude of diseases, including type II diabetes⁷⁶, dyslipidemia (abnormal lipid concentration in the blood), obesity, cardiovascular disease⁸¹, asthma⁸², and cancer⁸³. Although maternal diet and metabolic health are still a focus of DOHaD, other stressors such as exposure to endocrine-disrupting chemicals that can harm the hormonal system have also been investigated as root causes of fetal programming^{76,84}. The fetus may be exposed to harmful chemicals via certain types of plastics (i.e. bisphenol-A), maternal smoking, or environmental pollution⁷⁶.

In Chapter 4, I focus on the impact of maternal diet on the placenta, and subsequently, the placenta's impact on fetal growth. Birth size is a simple and easily obtained measurement

related to the *in utero* environment and thus was used as a staple metric in early discussions of DOHaD, especially as a tool to look at historical epidemiological data⁸⁵. Neonates may be classified as small for gestational age (SGA), which can be a consequence of intrauterine growth restriction, also known as FGR. SGA is defined by a fetal or neonatal body size more than two standard deviations below the mean or third percentile for that gestational age⁸⁶. It is important to note that not all SGA fetuses result from FGR, as some fetuses will naturally be small based on genetic or physiological factors but were not growth restricted *in utero*^{73,87}. FGR neonates are known to have health problems as they age, including but not limited to increased risk of MetS, type II diabetes, CVD, obesity, neurodevelopmental issues, and cerebral palsy^{73,86-88}. One of the mechanisms proposed to explain these fetal consequences is growth-triggered stress induced by the undernourished individual's rapid postnatal catch-up growth. This postnatal stress has been shown to exacerbate metabolic defects^{81,87}.

On the other hand, lack of postnatal catch-up growth in FGR neonates is associated with insulin resistance⁸⁶ and risk of long-term growth issues⁸⁷. FGR neonates may be classified as symmetric (20-30%) if they are proportionately small or asymmetric (70-80%) if they disproportionately lag in abdominal growth⁸⁹. It is believed that asymmetric FGR is caused by extrinsic influences such as placental insufficiency, and symmetric FGR is caused by intrinsic influences such as intrauterine infections or genetic abnormalities⁸⁹. These fetal growth patterns are complex and more research is needed to confirm these causal associations⁸⁹. FGR symmetry may also be dependent on the onset of FGR during gestation⁹⁰. Asymmetric FGR is thought to occur due to "brain sparing," where it is hypothesized that oxygen and nutrients are shunted to vital organs, including the brain and heart, leaving other organs like the liver underdeveloped⁹¹. There is no definitive agreement on whether symmetric or asymmetric FGR is predictive of more severe complications for the fetus⁸⁹.

On the other extreme of the size spectrum, infants born with high birth weight, categorized as macrosomia, are also associated with adverse outcomes for both the mother and child⁹². Macrosomia is defined as infants with a birth weight of more than 4000 g, though the upper limit may be set between 3720-4500 g and is not universally

agreed upon^{93,94}. Another related definition is large-for-gestational-age (LGA), which is used for fetuses with a weight >90th percentile or above two standard deviations for that gestational age⁹³. Fetal macrosomia may be caused by genetic factors, including epigenetic regulation related to the *in utero* environment, and maternal factors such as maternal age, BMI, body composition, diabetes status, gestational weight gain, and nutritional intake^{93,94}. LGA fetuses are at higher risk of intrauterine death, birth trauma, congenital anomalies, shoulder dystocia, and developing diabetes, MetS, obesity, asthma, and cancer later in life compared to fetuses that fall within the average range of size for gestational age^{70,93}.

Both SGA and LGA definitions that rely on absolute measurements or arbitrarily chosen percentiles are flawed as they regularly misclassify naturally small or large fetuses as abnormally sized⁸⁷. These definitions may also misclassify SGA fetuses as averaged sized if they lie within acceptable fetal size measurements but, in reality, have not met their growth potential⁸⁷. In other words, using statistical definitions does not reliably allow us to distinguish fetuses that grew normally throughout gestation from those that experienced flawed growth *in utero*⁹². A solution to this is customized fetal growth charts that consider genetic and physiological factors such as maternal age, sex, height, and parity to gauge the fetus' growth respective to its genetically predetermined growth potential⁸⁷. Another solution would be to look at fetal body composition instead of just fetal size, which may be achieved using imaging. US and Doppler techniques are currently used to diagnose FGR using fetal body measurements and umbilical artery flow⁹¹. MRI boasts superior soft-tissue contrast and though not commonly used in pregnancy, may provide high accuracy in fetoplacental measures of structure and function⁹⁵. Increased fetal brain:liver weight and volume ratios have been established as indicators of asymmetric FGR and predictors of fetal outcome^{96,97}. Measurements of placental volume and fetus:placenta volume ratio, also known as placental efficiency⁹⁸, can help identify at-risk fetuses, where very small or very large placentae relative to birth weight are associated with placental insufficiency and fetal death^{99,100}. It is important to note that the range of normal volume ratios change throughout gestation⁹⁷. Before birth, these volume ratios can be estimated using 3D ultrasound or MRI, where historically they were identified using post-mortem samples or by weighing the fetus and placenta after

birth^{95,96}. Being able to measure volumes *in utero* allows for the classification of early-onset (<32 weeks) and late-onset (\geq 32 weeks) FGR, which have different causes and consequences⁷³. Additionally, the risk of perinatal mortality differs according to the gestational age during the onset of FGR⁸⁷.

Critiques of the DOHaD hypothesis question whether the correlations between birth weight and adulthood disease are due to random error, focus too heavily on potentially unreliable historical data, or fail to account for confounding factors^{92,101}. Some studies recognize the validity of further research to investigate early life mechanisms of the origin of chronic disease but argue that current work related to DOHaD is too premature to be used as a basis for clinical interventions⁹². There have been examples of inconsistencies across DOHaD studies using observational data, which may not be suitable to confirm causal relationships⁹². Another criticism of DOHaD is the overemphasis on early life factors while neglecting the importance of lifestyle factors accumulated throughout life that contribute to the risk of metabolic disease⁹². Nevertheless, there are still many questions to be answered concerning DOHaD, particularly in areas concerning maternal nutrient status, and experimental species may be used as a more reliable framework in place of historical data⁹².

1.1.3.2 Effects of the Western Diet on the Placenta

The placenta is a vital temporary organ responsible for the exchange of nutrients between the mother and fetus and the production of growth factors and hormones during pregnancy¹⁰². Knowledge of the effect of maternal diet on placental function is limited; however, there is evidence that maternal diet impacts placental structure and growth¹⁰³. Moreover, most placental studies related to maternal diet have focused on maternal undernutrition, where maternal overnutrition, obesity, and metabolic disease have been less of a focus¹⁰⁴. The literature is very limited concerning the effect of the WD on the placenta; however, multiple studies are focused on the placental response to the high-fat diet and maternal obesity, both closely related to the WD. Pre-pregnancy nutrition status and maternal diet during pregnancy are important factors that have the potential to influence placental function and consequently fetal growth¹⁰⁵. Placental size is impacted

by diet, and both placental weight and the birth weight:placental weight ratio (placental efficiency) can provide estimations of offspring health¹⁰³. At both extreme ends of the placental size spectrum, there is an increased risk of coronary heart disease, blood pressure, hypertension, stroke, and type II diabetes in the offspring's adult life¹⁰³. Obesity is strongly correlated with the WD, and obesity during pregnancy is associated with increased placental weight and decreased placental efficiency^{104,106}. Other studies have shown decreased placental weight in rats fed a high-fat diet¹⁰⁷ and in humans with a high maternal energy intake early in pregnancy¹⁰⁵. Obese mothers produce placentae with increased thickness compared to placentae from normal BMI mothers¹⁰⁶. A study in rats also found increased placental thickness and changes in placental layer distribution in mothers fed a high-fat diet compared to a control diet¹⁰⁷. Increased placental thickness is associated with reduced placental permeability, limiting the amount of oxygen that can successfully be delivered to the fetus¹⁰⁶. Placental nutrient transfer capacity is influenced by factors including placental surface area and thickness, which may impact fetal growth and development¹⁰⁴. Other structural changes of the placenta observed in animal models of a maternal high-fat diet include increased infarction, villous calcification, and accumulation of lipid droplets in the placenta¹⁰⁴.

Overweight and obese women demonstrate localized placental inflammation at higher rates than normal-weight mothers^{104–106}. This inflammation has also been demonstrated in non-human primates fed a chronic high-fat diet¹⁰⁴. Placental inflammatory cytokine expression and nitrate stress are elevated in obese women and impact placental nutrient transport¹⁰⁵. Increases in inflammatory cytokines are associated with FGR, angiogenesis, and decreases in placental growth factor gene expression¹⁰⁵. A proinflammatory state in the placenta is also a potential contributing factor to modified nutrient transport¹⁰⁵. A study in mice has shown that inflammation in the placenta at late gestation in obese mothers exhibited a sex-specific effect, with placentae of male fetuses showing greater inflammation and macrophage activation¹⁰⁴. Many human and animal studies of placental function and response to maternal diet demonstrate sex dimorphism¹⁰⁴. The placenta has the same genetic sex information as the fetus since the placenta has a fetal origin and generally demonstrates a greater ability of female placentae to adapt to perturbations of the *in utero* environment, including a maternal Western or high-fat diet¹⁰⁴.

Placental vasculature dictates the ability of the placenta to deliver oxygen and nutrients from the mother to the fetus. Lifelong exposure to the high-fat diet and/or maternal obesity has been associated with abnormal placental vasculature and altered trophoblast invasion¹⁰⁷. Specifically, chronic high-fat diet consumption has been shown to reduce uterine blood flow and blood flow volume on the fetal side of the placenta in primates¹⁰⁴. Overnutrition, a consequence of the WD, has led to impaired vascular development in the sheep placenta at early and mid-gestation¹⁰⁴. High-fat diet-induced obesity in the mother has caused blood vessel immaturity and hypoxia in the placentae of mice¹⁰⁸. A possible mechanism behind poor vascularization in the placenta is disturbances to the fetoplacental renin-angiotensin system – a hormone system that regulates blood pressure, vascular resistance, and fluid balance – which has previously been linked to maternal high-fat diet exposure¹⁰⁷. Poor placental vascular function in humans is associated with placental oxidative stress and pre-eclampsia¹⁰⁵.

Though it is clear that the placenta makes adjustments related to cell growth and nutrient transport based on maternal factors like nutritional status, it is unclear how the placenta “senses” these external factors¹⁰⁵. A proposed explanation of a placental nutrient sensor is the placental mammalian target of the rapamycin signalling pathway, which controls amino acid transport and is influenced by diet-induced obesity^{109,110}. Another system that may act as a nutrient sensor is composed of the various epigenetic mechanisms that control placental gene expression¹⁰⁵. In rodents, a maternal high-fat diet increased placental transport of glucose and amino acids via upregulation of their transporters, resulting in larger fetal size and potentially contributing to LGA or macrosomia in offspring^{104,111}. Obesity and high concentrations of cholesterol and TG in maternal blood have been linked to an increase in placental fatty acid transporter proteins, contributing to both fetal overgrowth and increased fetal adiposity¹⁰⁴. Mouse studies have shown that placental epigenetic alterations triggered by the maternal high-fat diet were sex-specific, particularly for genes involved in controlling cellular, metabolic, and physiological functions important for adaptation¹¹². Protein markers of poor placental function, such as the plasminogen activator inhibitor, are elevated in obese women, providing evidence of genetic changes associated with maternal diet and body composition¹⁰⁵. A high-fat diet and maternal obesity have been linked to mitochondrial fragmentation in the human

placenta, potentially caused by a decrease in a protein related to mitochondrial fusion and cell metabolism¹¹². Down-regulation of this protein was observed in women with unexplained miscarriages and contributed to mitochondrial alterations in the placenta¹¹². Although this data supports the hypothesis that maternal diet and obesity influence placental gene expression and nutrient transport, global epigenetic changes in the placenta are still poorly understood¹¹³.

High fructose content is one aspect of the WD that generally harms physiology, though its impact on the placenta is understudied^{3,114}. In mice, maternal fructose consumption has led to placental inefficiency, increased lipids, and altered gene expression of systems that control oxidative stress in the placenta¹¹⁵. In maternal fructose intake studies, sex-specific changes in placental size and fetal outcome have been reported, with female placentae and fetuses displaying worse outcomes¹¹⁴.

Understanding how maternal diet affects placental structure and function is essential because the placenta is a programming agent of the adult health of the fetus¹⁰⁴. Adaptations made by the placenta *in utero* alter fetal nutrient supply, which in turn motivates epigenetic changes in the fetus that may contribute to DOHaD¹⁰⁴. Data supporting evidence of these placental trends associated with maternal diet come from various studies in both human and animal models using a diversity of species exposed to aspects of the WD for different durations. It should be emphasized that results may depend on the differences between studies, highlighting the need for further research on the impact of maternal diet on placental structure and function, especially in humans¹⁰⁴.

1.2 Guinea Pig Model

In the following chapters of this thesis, a guinea pig model is used in WD studies focusing on liver disease and pregnancy. Guinea pigs are often used in metabolism studies because they have a similar lipoprotein profile to humans where the majority of circulating cholesterol is transported as LDL, which is not observed in other rodents¹¹⁶. Other similarities include comparable plasma lipoprotein metabolism enzymes, a requirement for dietary vitamin C, gender plasma lipoprotein differences, and similar

responses to exercise and dietary interventions that include lowered plasma TG and increased plasma HDL^{116,117}. Like humans, guinea pigs develop atherosclerosis and display a related inflammatory response, which may be induced with high cholesterol diets¹¹⁶. Generally, the guinea pig is an ideal model for evaluating the mechanisms behind how diet interventions and drug treatments alter plasma lipids and lipoprotein metabolism¹¹⁶. Guinea pigs may be used as a NAFLD model as they develop enlarged, fatty livers when exposed to diets high in fat and cholesterol and demonstrate markers of liver damage, including altered ALT activity¹¹⁷. Importantly, unlike mice and rats, guinea pigs have shown to be reliable models for hepatic injury, steatosis, and cirrhosis without the need for genetic manipulations¹¹⁸. The storage, synthesis, and catabolism of cholesterol in the liver is similar between humans and guinea pigs, which may be relevant in NAFLD as it has been suggested that cholesterol plays a central role in the transition of NAFLD to NASH¹¹⁸. Certain risk factors for NAFLD are common in both humans and guinea pigs, including atherogenic hyperlipidemia, systemic inflammation, male gender, lack of exercise, and high-fat diet¹¹⁷. These risk factors are also relevant for CVD, closely related to NAFLD in humans¹¹⁸. Guinea pigs may be used as a model to evaluate therapeutic strategies for NAFLD as they display responses to interventions such as carbohydrate restriction, fatty acid saturation, dietary fibre, antioxidants, and pharmaceuticals that are similar to human responses^{117,118}.

The guinea pig is also an ideal model for pregnancy-related studies, as it has a relatively long gestation (~69 days) compared to other rodents but shorter than that of sheep or primates¹¹⁹. The guinea pig is easily bred, thanks to modest husbandry requirements and a docile temperament, and is an ideal species for assessing multi-generational effects of *in utero* perturbations in studies of DOHaD¹²⁰. Because of this long pregnancy, guinea pigs deliver precocial, or relatively mature and mobile, pups with many developmental events occurring *in utero* similar to the human fetus¹¹⁹. Examples of this are the similar timelines for muscle development and accumulation of adipose tissue in guinea pig and human fetal development¹²⁰. The relatively long guinea pig gestation allows for identifying critical periods during development that are vulnerable to *in utero* insults and displays adverse outcomes similar to those observed in humans¹²⁰. Unlike humans, guinea pigs usually produce more than one offspring (1-5); however, their litter sizes are

substantially lower than those typically seen in rats and mice (8-12)¹²⁰. Endocrine regulation is similar in the guinea pig and human pregnancy, with both species maintaining high and rising progesterone levels throughout birth¹²¹. The guinea pig placenta is hemomonochorial, having a similar structure to the hemochorial human placenta, and displays a deep trophoblast invasion similar to the human placenta¹²⁰. Due to similarities with human placentation and the fetal/maternal transport barrier, the guinea pig is a well-established model to study placental transfer and FGR and is one of the few species known to develop pre-eclampsia^{119,121,122}. A correlation between placental blood flow and fetal size has been shown in both guinea pigs and humans, highlighting the potential importance of this model for studying conditions that affect placental vascular function¹²⁰. There are also metabolic similarities in human and guinea pig pregnancies, including the transfer of glucose and amino acids across the placenta. Today, the guinea pig is one of the most important animal models for placental studies in obstetric research¹²².

1.3 Magnetic Resonance Imaging

1.3.1 Nuclear Magnetic Resonance

Nuclear magnetic resonance (NMR) is a phenomenon that occurs when magnetically sensitive nuclei are exposed to a strong magnetic field and perturbed by a weaker oscillating magnetic field¹²³. Nuclei possess an intrinsic quantized angular momentum known as spin, which is largely determined by the number of unpaired nucleons¹²³. “Spin-half” nuclei with half-integer quantum numbers occupy one of two discrete energy levels within an external magnetic field^{124,125}. These spin-half nuclei experience a magnetic moment in an external magnetic field and, therefore, can be detected using NMR techniques¹²⁴. Nuclei with integer or half-integer quantum numbers $> \frac{1}{2}$ exhibit electric quadrupoles instead of dipoles, meaning they are NMR sensitive but are not suitable for high-resolution NMR¹²⁵. Generally, the nucleus of interest in NMR is hydrogen (¹H), as it has a high natural abundance of 99.98% and is present in most organic compounds¹²⁵. In NMR, ¹H is often referred to as the proton itself since the electrons do not contribute to the magnetic resonance phenomenon¹²⁶. The nuclei

involved in NMR are also colloquially referred to as spins, not to be confused with the nuclear spin introduced above¹²⁶.

A strong applied magnetic field interacts with the magnetic moment of a nucleus, produced by its angular momentum, and nearly aligns with the main magnetic field in either a parallel (low energy) or antiparallel (high energy) orientation⁶⁹. At thermal equilibrium, the energy levels of non-interacting, identical nuclei in a magnetic field are described by the Boltzmann distribution¹²³. There is an almost equal number of spins existing at the two energy levels in this state, with only a tiny excess in the lower energy orientation¹²³. The relative population difference in energy levels is defined by the polarization, which, in the high temperature approximation ($kT \gg 1$, $k \sim 8.6 \times 10^{-5}$ eV/K), is inversely proportional to temperature and directly proportional to the magnetic field strength and an intrinsic property of the nucleus known as the gyromagnetic ratio (γ)¹²³. For hydrogen nuclei at body temperature in a 1.5 T field, only $\sim 1/100,000$ spins contribute to the NMR signal¹²⁷. This small polarization across the enormous number of spins in a sample produces a mean magnetic moment that aligns with the direction of the external magnetic field, referred to as the net magnetization (M_0)¹²⁶, as shown in Figure 1.5.

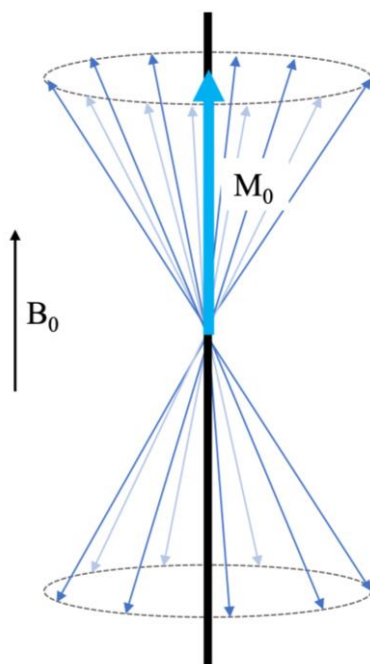


Figure 1.5: Representation of the net magnetization vector M_0 in an external magnetic field B_0 .

Quantum mechanics governs the behaviour of each nucleus; however, when referring to a large number of protons, such as in the human body, classical mechanics may be used to describe the mean magnetic moment of the nuclei¹²⁶. M_0 precesses about the main magnetic field due to the spins creating a torque when interacting with the magnetic field¹²⁶. The angular frequency, referred to as the Larmor frequency (ω_0), of this magnetic moment vector is directly related to the main magnetic field (B_0) and the gyromagnetic ratio (γ) of the nuclei, as expressed in Equation 1-1.

$$\omega_0 = \gamma B_0 \quad \mathbf{1-1}$$

To make a measurement, the net magnetization must be manipulated in a direction away from the main field since M_0 is much weaker than B_0 and would not be detectable along the same axis as B_0 ¹²⁶. To accomplish this detection of M_0 , a radiofrequency (RF) pulse oscillating at the Larmor frequency is applied for a short time perpendicular to the main magnetic field, producing a weak magnetic field perpendicular to B_0 in the rotating field of reference, referred to as B_1 ¹²⁶. The excitation pulse is called an RF pulse because Larmor frequencies are typically in the MHz range, which corresponds to the radiofrequency range of the electromagnetic spectrum¹²⁷. The net absorption of energy from the RF pulse promotes spins to transition from the low energy state to the high energy state¹²⁶. The RF pulse also causes the net magnetization M_0 to experience nutation about the B_1 field as it is tipped into the transverse plane perpendicular to the B_0 field while the RF pulse is applied¹²⁸. The amplitude and duration of the RF pulse will determine the flip (or tip) angle (α), describing the amount of nutation away from the axis of the B_0 field¹²⁵.

In simple experiments, α is chosen to be 90° to achieve the maximum value of the transverse component of M_0 upon excitation¹²⁵. A 180° RF pulse would result in a net magnetization in the negative direction on the B_0 axis¹²⁵. In a Cartesian coordinate system, the magnetization component in the direction of the B_0 axis is called the longitudinal magnetization and is denoted as a vector in the z-direction, M_z ¹²⁵. The component of M_0 in the transverse plane or x-y plane is called the transverse

magnetization and is represented as a rotating phasor, M_{xy} ¹²⁵. These components of the net magnetization can be described by Equations 1-2 and 1-3, where ϕ represents an arbitrary initial angle position, or “phase shift”, of M_0 in the transverse plane¹²⁵.

$$M_z = M_0 \cos \alpha \quad \mathbf{1-2}$$

$$M_{xy} = M_0 \sin \alpha e^{i(\omega_0 t + \phi)} \quad \mathbf{1-3}$$

According to Faraday’s law of induction, any changing magnetic field produces an electromotive force¹²⁹. Therefore, when an RF pulse is applied and M_0 experiences nutation, the spins radiate electromagnetic energy that is detected as an induced voltage by receive coils¹²⁵. This voltage is amplified and used to form the NMR signal measurement¹²⁵. The receive coil is only sensitive to magnetization perpendicular to B_0 , and the voltage produced in the coil is proportional to the NMR signal and the square of the magnetic field strength of B_0 ¹²⁶.

After the magnetic moments of the nuclei are tipped into the transverse plane, they immediately start to lose phase coherence, or dephase, with each other, causing the M_{xy} signal to decay exponentially and bringing the detected signal amplitude to 0 within a few milliseconds¹²⁸. The rate of this signal decay in an ideal homogeneous magnetic field is characterized by the transverse, or spin-spin, relaxation constant T_2 ¹³⁰. T_2 is a result of the intrinsic relaxation process in tissue and is related to the microscopic magnetic fields caused by adjacent protons and random molecular and atomic interactions¹³¹. The decay of M_{xy} over time due to T_2 is known as the free induction decay (FID) and can be expressed by Equation 1-4¹²⁵.

$$M_{xy} = M_0 \sin \alpha e^{i(\omega_0 t + \phi)} e^{-t/T_2} \quad \mathbf{1-4}$$

Meanwhile, the longitudinal magnetization M_z is recovered to M_0 in the absence of the RF pulse¹²⁵. This relaxation is completely independent of the transverse relaxation and is related to the transitions of excited spins back to their thermal equilibrium¹²⁵. The molecules in the sample undergo random translational, vibrational, and rotational motion, or “tumble”, in the external field¹²⁵. This tumbling motion within the B_0 field causes the dipole strength of an individual spin to fluctuate at the Larmor frequency and is further

affected by interactions with other fluctuating dipoles, known as intramolecular or dipole-dipole interactions¹²⁵. These interactions, determined by the random motion and spatial distance between nuclei, cause spin-state transitions between the low and high energy states¹²⁵. By this process, the extra energy absorbed from the RF pulse is released to the surrounding environment or “lattice”. This relaxation depends on the proximity of spins to other molecules, which varies according to tissue composition and pathophysiological state^{125,126}. This M_z relaxation is characterized by the longitudinal, or spin-lattice, relaxation time T_1 ¹²⁵. The mathematical expression of the M_z at a given time (t) after an RF pulse of flip angle α is given by Equation 1-5.

$$M_z(t) = M_0(1 - e^{-t/T_1}) + M_0 \cos \alpha e^{-t/T_1} \quad 1-5$$

T_1 is much slower than T_2 , as seen in Figure 1.6, and the difference between these rate constants must be considered in all NMR spectroscopy or imaging¹²⁶. The unique T_1 and T_2 characteristics associated with different tissues in the body generate contrasts useful for imaging anatomy *in vivo* using MRI¹²⁶.

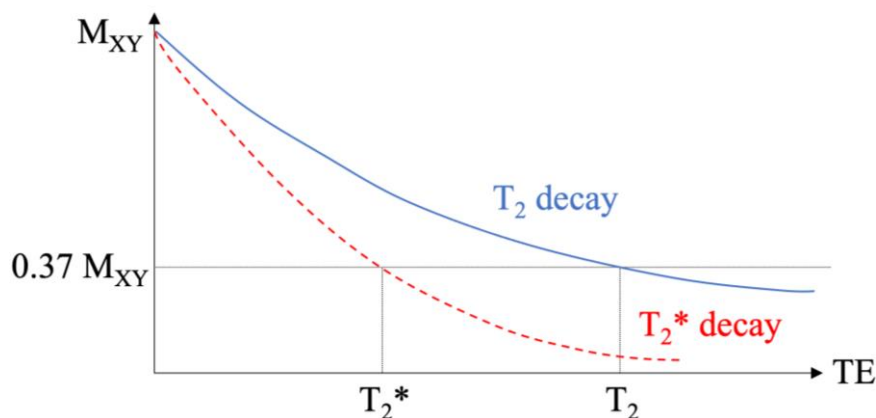


Figure 1.6: Graphical representation of the longitudinal (T_1) and transverse (T_2) relaxation times.

1.3.2 Magnetic Resonance Spectroscopy

In a basic sense, spectroscopy is the study of the interaction between matter and electromagnetic radiation¹³². In magnetic resonance spectroscopy (MRS), the interaction of interest is between an applied external magnetic field and the resultant electromagnetic signals produced by nuclei within a sample of interest¹³³. NMR spectroscopy has been

used since the early 1950s in physical chemistry. When this technology is applied in a biomedical context it is generally referred to as MRS¹³³. The word “nuclear” was eliminated from the phrase to dispel the false implication that MRS is associated with nuclear radioactivity¹³³.

MRS provides chemical and structural information about molecules within the sample by observing differences in NMR due to the local magnetic fields around nuclei, which are slightly but measurably affected by their environment and placement within a molecule¹³⁴. Specifically, the magnetic field a nucleus experiences is influenced by the proximity and motion of nearby electrons and atoms, either having a shielding or an enhancing effect^{126,134}. The B_0 field causes electrons in an atom to circulate within their orbitals, and this induced motion generates a small local magnetic field at the site of the nucleus that is proportional to B_0 ¹²³. This shielding becomes more complex when considering a sample containing molecules instead of just atoms, with the resonant frequency of a nucleus characteristic of the electronic structures surrounding it¹²³. The phenomenon of slight differences in resonant frequency between nuclei in different local chemical environments is known as the “chemical shift”, and is a function of the chemical structure of the molecule¹³⁴. While the electron shielding factor itself is a constant, the chemical shift increases linearly with field strength, meaning that the spectral resolution is higher at large B_0 strengths¹²⁵.

A spin-spin coupling may occur within a molecule if multiple nuclei exist within different chemical environments and interact with each other¹³⁴. This phenomenon results in split peaks in the NMR spectrum, where spins occupying each energy level are slightly shifted away from each other, providing additional information about the arrangement of atoms in that molecule¹²³. Obtaining a very precise measurement of the spectroscopic peaks in a sample enables us to quantify the relative number of protons in each position on a molecule¹²⁶. MRS may be used to identify and quantify the concentration of metabolites *in vitro* or *in vivo* and provides a means of monitoring dynamic metabolic processes over time¹³³.

Before the signal is acquired, the magnetic field is shimmed to correct for B_0 inhomogeneities that may affect the precision of the measurement¹³⁴. This shimming is done using shim coils placed around the sample that generate small local fields to provide the most homogenous B_0 field possible near the sample¹³⁴. In order to measure a signal, an RF pulse (as described in section 1.3.1) is applied either in short, intense increments at a specific frequency (pulsed method) or applied constantly and swept over varying frequencies (continuous wave method)^{134,135}. Although both methods have been used since the development of MRS, pulsed methods are more widely used today¹²⁵. The decay is measured as the previously introduced FID and consists of a superimposition of all resonances from the different nuclei in the sample¹³⁴. To get from the FID to the frequency spectra typically associated with MRS, the Fourier transform (FT) must be applied¹²⁵. The general idea behind the FT is the Fourier series, which is a way of representing any complex signal as a series of sinusoidal waves described by different frequencies, phases, and amplitudes^{126,136}. The FT enables the mathematical transformation of information from the FID in the time domain into the frequency domain, where distinct spectral peaks, or resonances, corresponding to each chemical shift are visible (Figure 1.7)¹³⁴. In other words, the FT is a mathematical tool that decomposes a complicated signal into the frequencies and relative amplitudes of its simple component waves expressed as a complex-valued function¹³⁶. The resultant complex signal consists of real (absorption spectrum) and imaginary (dispersion spectrum) components that contain information about the phase shifts corresponding to each frequency, though typically only the absorption spectrum is used in clinical MRS¹³⁵. If data is known in either the time or frequency domains, the FT or inverse FT can be used to compute data in the other domain¹³⁶.

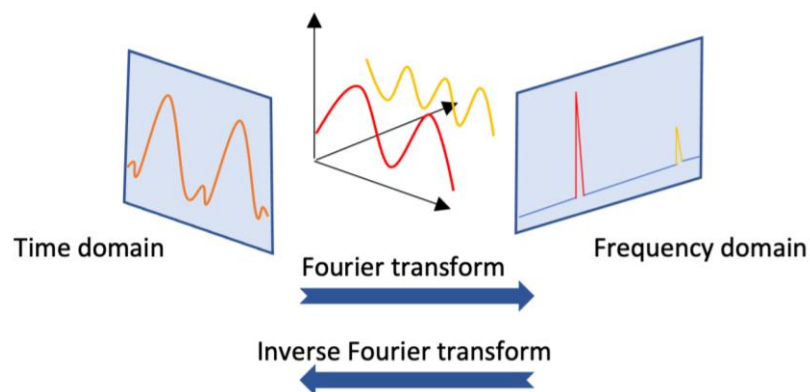


Figure 1.7: Visual representation of the Fourier transform

Each spectrum acts as a unique fingerprint of the compound in question, allowing for identification of organic compounds using MRS¹³⁵. The multiple peaks in the MR spectrum represent the relative contributions of individual nuclei that make up metabolites in the region sampled, existing at distinct chemical shifts from each other¹³⁶. In the MR frequency domain, the area under each peak corresponds to the concentration of that chemical species and, though not common, direct quantification of metabolites is possible using advanced acquisition protocols, calibrations, and relaxation time measurements^{125,134}. The chemical shift of each molecule is usually expressed in dimensionless units (parts per million, ppm) using a reference material such as water¹³⁴.

In vivo MRS is performed to detect small molecules within cells or extra-cellular spaces and monitor metabolic changes in response to disease or treatment¹³⁷. ¹H and ³¹P are the most commonly used nuclei for *in vivo* MRS as they are naturally abundant and have a high gyromagnetic ratio, though ¹³C, ²³Na, and ¹⁹F are also targets of clinical MRS¹³⁴. Water suppression is usually used in ¹H MRS as the spectrum would otherwise be dominated by the water peak, and metabolite peaks would be difficult to detect above the background noise¹²⁵. Though the chemical shift is mostly affected by electron shielding, other factors, including temperature and pH, may have measurable effects on the chemical shifts of specific compounds¹³⁵. *In vivo* MRS is most commonly done using single-voxel spectroscopy, where a single voxel of interest within an organ is selectively targeted using gradients (expanded upon in section 1.3.3) and excited to produce a spectrum from that voxel^{126,134}. Smaller voxels require a higher number of signal

averages, resulting in longer scan durations¹³⁴. For greater anatomical coverage, chemical shift imaging uses a matrix of voxels to form the spectra, typically in a 2D single slice¹³⁴. Advantages of *in vivo* MRS include its capacity for direct measurement of distinct metabolites, robustness, reproducibility, rapid sampling, a minimal requirement for sample preparation, and the ability to sample small volumes¹³⁴. A disadvantage of this technique is its failure to detect metabolites in low abundance or metabolites co-resonant with higher concentration metabolites that are therefore hidden in the spectra¹³⁴. Interpretation of data from *in vivo* experiments must consider sources of potential error related to hardware, water suppression efficiency, localization of voxel, choice of analysis technique, and tissue characteristics¹³⁴.

The most common application of *in vivo* ¹H MRS is in the brain, as many important cerebral metabolites are present in the proton spectrum, including N-acetyl aspartate, choline, creatine, myo-inositol, glutamine and glutamate, and lactate¹³⁴. Pattern changes in the MR spectrum over time in the brain may indicate disease and aid in diagnosing conditions such as white matter demyelination, Alzheimer's disease, or ischemia¹³⁷. Conditions that affect brain metabolism are also a focus of *in vivo* MRS research, including Parkinson's disease, epilepsy, cancer¹³⁷, and traumatic brain injury¹³⁸. Lipid signals in the brain are generally associated with necrosis observed in high-grade brain tumours and have also been observed in MR spectra of multiple sclerosis patients¹³⁷. ¹H MRS has also been used as a research tool in the context of liver disease to provide insight into mechanisms involved in NAFLD, cirrhosis, and hepatocellular carcinoma¹³⁴. ³¹P MRS can provide measurements related to intracellular pH and adenosine triphosphate (ATP) synthesis and has been used to assess energy metabolism in the skeletal muscle, brain, heart, and liver¹³⁹.

1.3.3 Magnetic Resonance Imaging

While both MRS and MRI are based on NMR theory, they differ in application¹³³. MRS is used to detect signals from chemical compounds to evaluate *in vivo* biochemistry, whereas MRI detects signals produced by water in tissue to acquire images of the macroscopic anatomy¹³³.

In MRI sequences, the FID is manipulated to create an echo, which is the refocusing of the spin magnetization used to measure the NMR signal¹²⁶. Two types of echo can be generated: the spin echo (SE) or gradient echo (GE)¹²⁶. In both cases, an RF pulse is applied to flip the magnetization into the xy-plane, similar to how the FID would be generated¹²⁶. Typically, a 90° RF pulse may be used to flip all of the magnetization into the xy-plane but smaller flip angles ($< 90^\circ$) may also be used to generate echoes. To create a spin echo, the transverse magnetization is left to dephase for some time after the RF pulse is applied. After this delay, a 180° RF pulse is applied to flip all the spins about the x-axis in the transverse plane¹²⁶. This rotation reverses the phase angles of the spins, causing them to rephase and produce an echo, as seen in Figure 1.8¹²⁶.

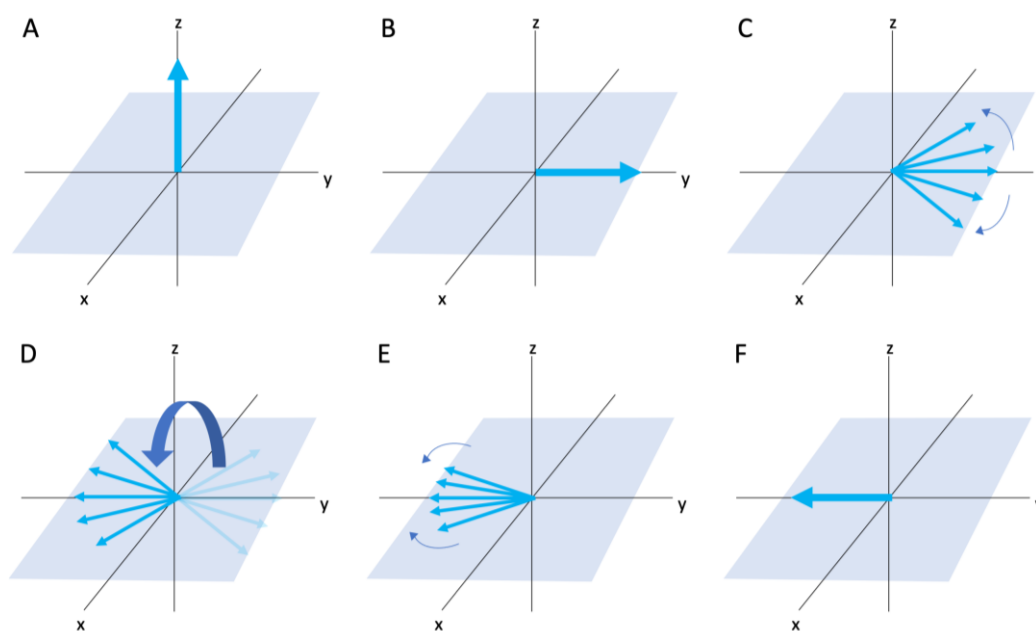


Figure 1.8: Formation of a spin echo. (A) Magnetization is in the M_z direction (B) A 90° RF pulse tips the magnetization into the xy-plane (C) Spins begin to de-phase with each other (D) A 180° RF pulse is applied to flip the spins in the xy-plane (E) Spins move back into phase with each other (F) An echo is formed.

The gradient echo is generated instead using a single 90° RF pulse followed by a gradient – a magnetic field that changes in magnitude across a specific direction and distance – that refocuses the phase of the nuclei spins¹²⁶. A negative gradient lobe is applied immediately after the RF pulse to rapidly dephase the magnetization in the transverse

plane, followed by a positive but equal in magnitude gradient lobe that reverses the magnetic field gradient, causing the spins to rephase and come back into phase¹²⁶. Like the FID, these echoes are detected by a receive coil, where they can be recorded as NMR signals. The signal produced by an echo depends on the concentration of spins, intrinsic relaxation properties (T_1 , T_2) in a particular tissue, and the echo time (TE) – the time between applying the RF pulse and creating the echo¹²⁶. The time period between the application of successive RF pulses is the repetition time (TR)¹²⁶.

Images generally display a contrast, or weighting, primarily dependent on the T_1 , T_2 , or proton density (PD) of the sample¹²⁶. PD-weighted images display high signal intensities in areas of high proton density, T_1 -weighted images display high intensity in areas with short T_1 , and T_2 -weighted images display high signal intensity in areas with long T_2 ¹²⁶. The dominant weighting of the image can be selected by manipulating the TE, TR, and α of the sequence, as detailed in Table 1.1¹²⁶.

Table 1.1: Image weighting via manipulation of TE, TR, and α ¹²⁶

Spin Echo Sequences		
	Short TE (< 40 ms)	Long TE (> 75 ms)
Short TR (< 750 ms)	T_1 -weighted	Not useful
Long TR (> 1500 ms)	PD-weighted	T_2 -weighted
Gradient Echo Sequences		
	Short TE (< 15 ms)	Long TE (> 30 ms)
Small α (< 40°)	PD-weighted	T_2 -weighted
Large α (> 50°)	T_1 -weighted	Not useful

The information is spatially encoded in MRI, producing a matrix of information that is transformed into a 2D image or 3D volume¹²⁵. Magnetic field gradients enable the spatial localization and encoding of information in three dimensions in a Cartesian coordinate system¹²⁵. The ground-breaking work surrounding magnetic field gradients that eventually resulted in the first MRI of a human was pioneered by Paul Lauterbur and further developed by Peter Mansfield; these joint efforts won them the Nobel Prize in Physiology or Medicine in 2003¹²⁵. Magnetic field gradients are linearly varying

magnetic fields applied along an axis that cause the spin's location to be encoded in its Larmor frequency^{125,127}. Since the magnetic field of the gradient changes linearly with position along the applied axis, spins along that axis experience slightly different magnetic fields based on their position in space¹²⁵. The gradient strength is ~1% of the B_0 field strength, meaning that the gradients result in very small perturbations to the magnetic field¹²⁷. The addition of the gradient field to B_0 causes spins along the gradient axis to precess faster or slower than the Larmor frequency, depending on their position. Note that the center of the gradient will only experience the main field B_0 ¹²⁶. Therefore, as shown in Equation 1-6, the angular frequency of any spin (where r is a location described by x, y, z) can be written as a function of the gradient strength, where G_r is the strength of the gradient applied along the r direction¹²⁵.

$$\omega_0(r) = -\frac{\gamma}{2\pi} (B_0 + G_r \cdot r) \quad \mathbf{1-6}$$

The spatial localization of the MR signal requires three orthogonal linear gradients that are typically applied along the z (parallel to the MRI bore), x (left-right), and y (top-bottom) axes¹²⁶. Since the gradients have both magnitude and direction, they can be considered vectors and can be used to generate magnetic field gradients applied along any direction if applied in combination¹²⁷. These gradient fields are produced by gradient coils inside the bore of the MRI scanner¹²⁶. The gradient strength is expressed as mT/m, and larger gradient strengths allow for images to be acquired with a smaller field of view and thinner slices¹²⁶. Gradients both allow for slice selection, the selective excitation of particular anatomical planes of interest, and spatial encoding of the positions of resonating spins¹²⁵.

Combining a band-limited RF pulse with a gradient restricts the MR interactions to a 2D plane, or slice, of a prescribed location and thickness^{126,127}. The slice selection gradient causes spins along that axis to resonate at progressively increasing frequencies, and an RF pulse is transmitted at a bandwidth of frequencies corresponding to spins within the slice of interest (Figure 1.9)¹²⁵. Slice selection can be performed in any direction, producing transverse, sagittal, coronal, or oblique slices¹²⁶. After the RF pulse is applied and gradient removed, only the spins in that slice experience transverse magnetization

and contribute to the MR signal, while all other spins remain aligned with the B_0 field¹²⁷. The width and location of the slice can be controlled via the gradient strength and range of frequencies in the RF pulse bandwidth¹²⁷. After the RF pulse is applied, a refocusing gradient with equal and opposite amplitude to the slice selection gradient is used to bring the spins in that slice back into phase with each other to avoid signal loss¹²⁵.

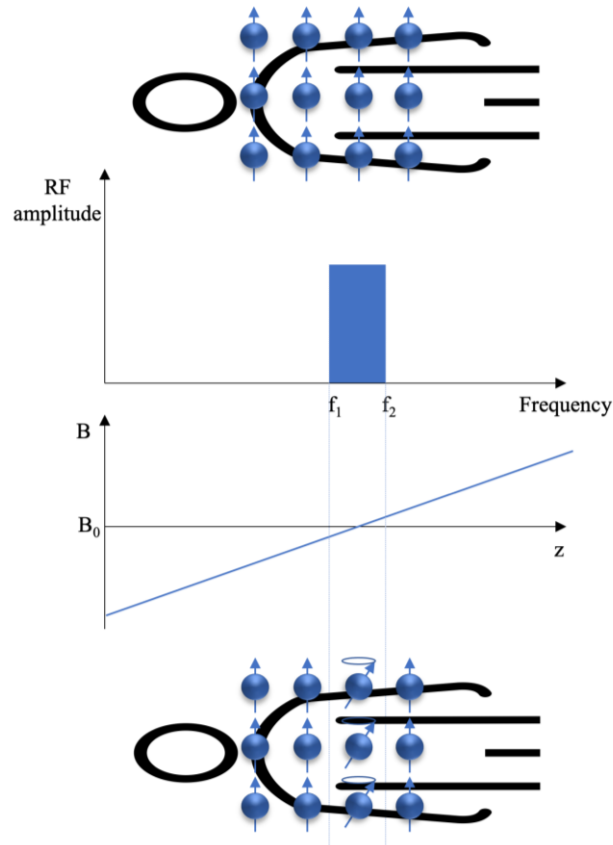


Figure 1.9: Schematic of slice selection using an RF pulse with a bandwidth from f_1 to f_2 applied in combination with a gradient in the z -direction. Only spins within the bandwidth are selectively excited by the RF pulse.

After a slice is selectively excited, the next step is spatially encoding the spins within the slice in the two directions orthogonal to the slice selection gradient¹²⁵. These are known as the frequency and phase encoding gradients (Figure 1.10). By convention, slice selection is performed along the z -direction, frequency encoding along the x -direction, and phase encoding along the y -direction¹²⁵.

The frequency encoding gradient, also known as the readout gradient, is applied along the x-axis continuously while the MR signal is being sampled, resulting in spins with linearly varied resonant frequencies along the x-axis^{125,126}. Since the gradient is present during the MR signal measurement, the signal's frequency will depend on the position of the material within the gradient field, so the signal is “frequency encoded” in the x-direction¹²⁶. The signal will consist of a mixture of many frequency components, which, as explained in section 1.3.2, can be decomposed using the Fourier transform into a spectrum that represents a one-dimensional projection of the sample¹²⁶. Therefore, for a single RF excitation, all the spatial frequencies in the x-direction can be collected in real time¹²⁶.

Phase encoding is done in a similar way to frequency encoding, with the difference being that the phase encoding gradient is not continuously on during acquisition; rather, it is turned on for a short amount of time to cause the spins to experience a phase change¹²⁶. Although it would be time-efficient to have two continuous orthogonal gradients frequency encoding simultaneously, the frequency value is scalar, and therefore it would not be possible to discern which gradient a particular spin's frequency originated from using this strategy¹²⁶. Instead, one of the gradients manipulates the phase of the spins so that each spin has a unique combination of phase and frequency that corresponds to its position in 2D space. In practice, the phase encoding gradient is applied before the frequency encoding gradient so that the spins experience different frequencies during sampling while still retaining their previous phase shifts¹²⁶. When the gradient is on, the precession of the nuclei increases or decreases depending on their position along the y-axis. When the gradient is turned off, the nuclei will revert to the Larmor frequency but will retain the different phase angles acquired during the time the gradient was applied; in other words, they are “phase-encoded”¹²⁵. The relative phase difference between these spins persists until another gradient is applied or the signal decays due to T_2 relaxation¹²⁵. Unfortunately, there is no way to distinguish signals along the phase-encode direction using a single acquisition since only the sum of all phase shifts for each frequency is measured¹²⁶. By repeating the excitation and measurement at many different phase-encoding steps, or phase changes, multiple data points are acquired that demonstrate different strengths of the MR signal over a range of gradient moments¹²⁶. With this

information, we can disentangle the individual phase contributions using the inverse Fourier transform, where each phase component corresponds to a different spatial position along the y axis¹²⁶. The MR sequence must be repeated with a different phase-encoding gradient until all possible spatial frequencies have been sampled, corresponding to the number of rows of pixels in the image¹²⁶. The total scan time of an MR sequence is equal to the number of signal averages multiplied by the number of phase encoding steps multiplied by the TR¹²⁶. Signal averaging is achieved by repeating measurements under similar conditions to increase SNR by suppressing effects from random noise¹²⁶.

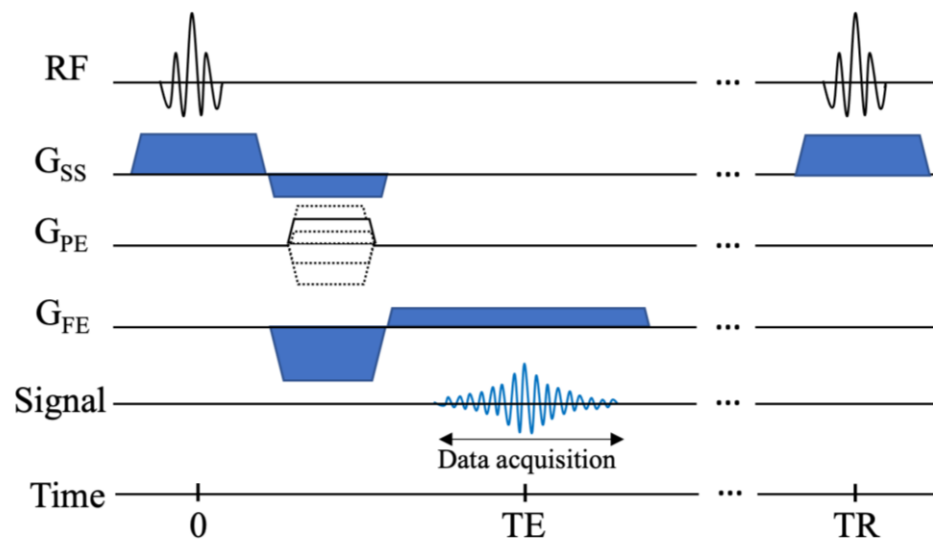


Figure 1.10: An example of a basic gradient echo pulse sequence diagram showing the slice selection (G_{SS}), phase encoding (G_{PE}), and frequency encoding (G_{FE}) gradients at work to encode the spatial location of the echo.

A 2D inverse Fourier transform is used to convert the spatially encoded data in one slice from a raw data matrix to a 2D image¹²⁶. Unique to MRI, compared to other imaging modalities, the raw data is complex and contains both a real and imaginary component¹²⁵. These components can be used to construct magnitude and phase images, where the magnitude image is used for diagnostic purposes, and the phase image may be used to identify regions of B_0 inhomogeneity¹²⁵. The complex nature of this data means it contains inherent properties such as symmetry that may be exploited to enable more efficient image acquisition and reconstruction¹²⁵. 3D MRI is an alternative to acquiring 2D images at multiple slices and may be advantageous for certain applications that

require high axial resolution images¹²⁶. The 3D acquisition technique requires a second phase-encode axis, resulting in longer scan times¹²⁶.

1.3.4 Chemical Shift-Encoded MRI

As introduced in section 1.3.2, chemical shift is a property that allows nuclei to be distinguished from each other based on slight differences in their resonant frequencies due to their local chemical and molecular environments¹²⁵. Perhaps the most common example of chemical shift in MRI is the shift of 3.5 ppm between water and fat protons^{125,140}. Water and fat are obvious initial targets of chemical-shift encoded MRI (CSE-MRI) as they have good SNR at clinical field strengths and are much more abundant than other endogenous metabolites¹⁴¹. This chemical shift exists because the methyl group (CH_3 -) on fatty acids causes spins to experience a different electron density distribution and magnetic shielding than spins on a water molecule¹²⁵. Chemical shift-encoded MRI is an imaging technique that uses multiple TEs to measure the phase variation between signals originating from different metabolites¹⁴². CSE-MRI techniques employ modified pulse sequences to encode the chemical shift difference into the signal's phase that can be used to achieve separation of fat and water during postprocessing¹⁴⁰. While MRS techniques can detect and separate signals from fat and water, CSE-MRI has the advantage of faster acquisition times and providing spatial information¹⁴². As long as the chemical shifts between the components are known, it is possible to calculate the TEs at which the two signals will be in-phase and out-of-phase with each other¹⁴⁰.

W. Thomas Dixon first introduced this method in 1984, using a modified SE sequence to acquire images using TEs when fat and water were in-phase and 180° out-of-phase (Figure 1.11)¹⁴¹. The in-phase and out-of-phase images are combined to create fat-only and water-only images of anatomy^{126,141}. Using a conventional SE, the water and fat signals are in-phase at the echo time, but due to their different precession frequencies, they move out of phase over time¹⁴¹. By shifting the readout gradient slightly during a second acquisition, it is possible to acquire the minimum signal that occurs when water and fat are 180° out-of-phase^{140,141}. This pioneering work is known as the two-point Dixon method and is the simplest iteration of the fat-water separation technique¹²⁶. Using

this method, the in-phase image contains the sum of signals from fat and water, while the out-of-phase image is the difference of the fat signal from water signal¹²⁶. The water-only image is useful for fat suppression in instances where the hyperintense fat signal may obscure pathology, and both images may be used to quantify the fat and water content in an area of interest¹⁴⁰. Since this method only requires the addition of a time delay to an otherwise conventional SE sequence, there is little to no sacrifice of spatial resolution, SNR, or imaging speed required to obtain the additional information¹⁴¹. This technique is limited by B_0 inhomogeneity which appears as a phase error and affects the summation and subtraction approach to fat and water image construction¹⁴⁰.

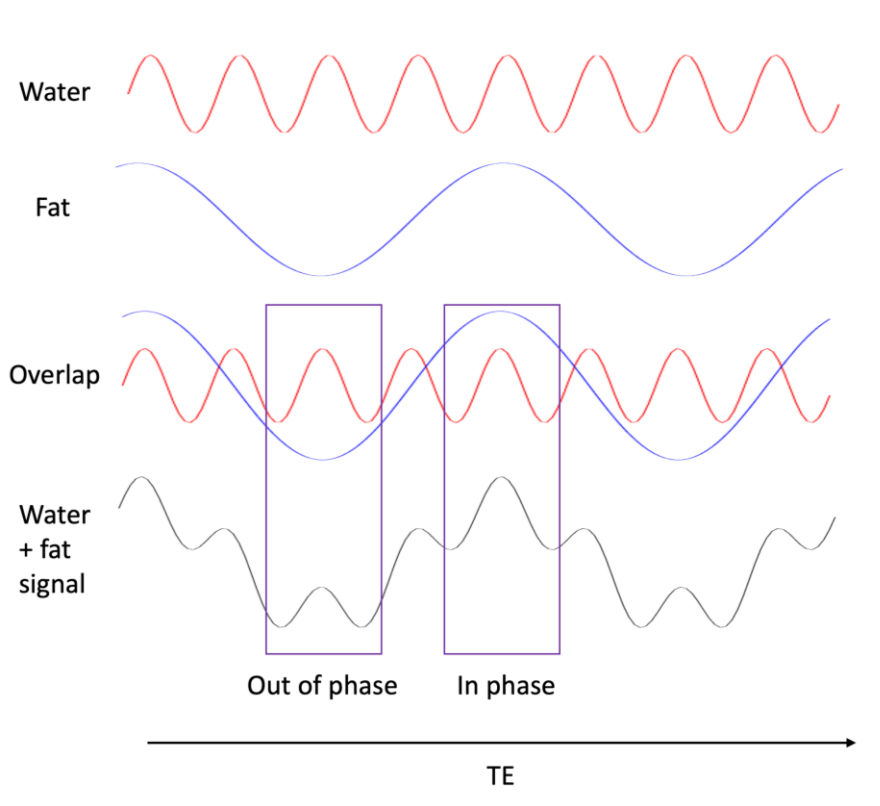


Figure 1.11: An example of the MR signal from fat and water coming in and out of phase with each other at different TEs. In a two-point Dixon acquisition, images would be acquired at the TEs that correspond to the purple boxes.

The attempt at correction for B_0 inhomogeneity led to the introduction of the three-point Dixon method, which acquires a third image with an in-phase TE¹²⁶. Using the three-point Dixon method, the two in-phase images are used to calculate and remove the phase acquired from B_0 inhomogeneities in each voxel, followed by the simple postprocessing

of the two-point method¹⁴⁰. Additions to the three-point method include the four-point Dixon method, which involves an additional acquisition at another TE to provide information that can be used to calculate the line width of the fat spectra¹⁴³. Another strategy involves obtaining a T_2^* map, the accelerated T_2 decay that may be caused by microscopic magnetic susceptibilities (further discussed in section 1.1.3.6), in addition to fat, water, and B_0 images¹⁴³.

Modern magnet design and increased shimming capabilities led to renewed interest in the Dixon technique in the early 2000s, with the emergence of more complex algorithms including IDEAL (Iterative Decomposition of water/fat using Echo Asymmetry and Least-squares estimation)¹⁴⁴. The IDEAL method utilizes multiple asymmetrically acquired echoes and a more complex least-squares decomposition algorithm to separate fat and water¹⁴⁴. This method was introduced to minimize noise and eliminate the dependence of noise on the fat:water ratio in a voxel¹⁴⁴.

So far, the fat peak has been simplistically described by a single peak, but in reality, the fat signal consists of several resonant frequencies, including those originating from methylene ($-\text{CH}_2-$) and olefin ($-\text{CH}=\text{CH}-$) groups that, in addition to the methyl group, are present on TG molecules¹⁴³. This issue can be overcome with fat spectrum modelling, either using *a priori* MRS measurements or estimating the fat spectrum from the measured CSE-MRI data¹⁴⁵. Not only does this modelling provide more accurate estimations of T_2^* and fat/water content, but it may also be used to measure fatty acid chemical composition, which is relevant to studies of obesity, hepatic steatosis, and cancer¹⁴⁶. Additionally, IDEAL methods can identify and characterize brown adipose tissue and differentiate it from white adipose tissue *in vivo* using the known difference in fat fraction between these compounds¹⁴⁷.

As more improvements were continuously made to CSE-MRI, algorithms have been introduced to address confounding factors of measurement, including relaxation parameters (T_1 , T_2^*), the spectral complexity of fat, and noise biases¹⁴⁸. By correcting these inconsistencies, it is possible to estimate the proton density fat fraction (PDFF), defined as the ratio of the density of mobile protons from fat to the total density of mobile

protons in the sample¹⁴⁹. The PDFF is constructed by dividing the fat image by the sum of the fat and water images and provides information on the percentage of fat in the body^{148,149}. Today, PDFF is the most practical and meaningful MRI-based biomarker of tissue fat concentration based on its robustness, reproducibility, accuracy, and precision¹⁴⁹. The PDFF is highly correlated with *ex vivo* measurements of TG concentration¹⁴⁹. A more complex IDEAL algorithm can be used to achieve simultaneous quantification of PDFF and T_2^* ¹⁵⁰, similar to the IDEAL technique used in Chapters 2 and 4 of this thesis to quantify these measurements. Modern developments have led to the use of CSE-MRI sequences in routine clinical settings¹⁴⁰.

CSE-MRI is often used for PDFF estimation in the liver, particularly in the study of NAFLD, and has been validated for use at clinical field strengths^{148,151}. Another popular application is its use in the assessment of T_2^* and PDFF in osteoporosis¹⁵². Aside from PDFF and fat suppression, CSE-MRI is used to produce B_0 maps, useful for field shimming and quantitative susceptibility mapping^{140,153}. T_2^* mapping, which may be achieved with CSE-MRI, is used to assess the concentration of iron in tissue¹⁴⁰. CSE-MRI methods can be employed for non-proton imaging, including in ^{19}F imaging¹⁵⁴ and are demonstrated in Chapter 3 of this thesis to separate signal from hyperpolarized [1- ^{13}C]pyruvate (see section 1.3.7.1) and its metabolites using a modified IDEAL technique¹⁵⁵.

1.3.5 Diffusion-Weighted Imaging

Diffusion-weighted imaging (DWI) is sensitive to the molecular diffusion of water molecules within the body, providing information on the microstructure of organs¹⁵⁶. In this context, diffusion refers to Brownian motion, or the random displacement of molecules due to movement and collisions driven by thermal energy¹⁵⁷. In a perfectly homogeneous medium, this displacement would be random, isotropic, and described by a Gaussian distribution dependent on the type of molecule, the temperature of the medium, and time allowed for diffusion¹⁵⁸. The spread, or variance, of the Gaussian distribution depends on the diffusion time interval and the diffusion coefficient (D), which represents

the magnitude of the molecule's diffusion as a function of displacement and velocity^{157,158}. D is approximately equal to $3 \times 10^{-9} \text{ m}^2/\text{s}$ for water at 37°C ¹⁵⁸.

The complex structure of the human body does not allow for perfectly random diffusion. Instead, water molecules exist within cells and in extracellular compartments coming into contact with barriers of varying diffusivity^{158,159}. While extracellular water molecules experience relatively free diffusion, intracellular water molecules experience "restricted diffusion"¹⁵⁹. Restricted diffusion due to compartmental boundaries and molecular obstacles results in a decreased diffusion distance compared to particles experiencing unrestricted diffusion¹⁵⁸. Different tissues in the human body experience different diffusion properties based on characteristic cellular architecture and proportions of intra- and extracellular regions, which may be further altered by disease¹⁵⁹. Therefore, DWI provides a functional dimension to conventional anatomic MRI that may be used to obtain information regarding microscopic architecture and blood flow¹⁵⁹.

DWI uses magnetic field gradients, termed diffusion gradients, to identify the displacement of spins based on small differences in their Larmor frequencies^{156,159}. The most common approach involves a spin echo sequence with equal area gradient pulses applied before and after the 180° refocusing pulse¹⁵⁶. A moving spin will accumulate phase from the diffusion gradient proportional to its displacement in the direction of the gradient¹⁵⁶. If there is no motion, the phase shifts accrued from the two equal diffusion gradients cancel out. If all the spins are moving coherently within the field, they acquire an identical phase. The case of diffusion is unlike these two scenarios. Instead, the spins experience a random displacement, and the phase shifts accumulated by individual spins differ from each other¹⁵⁶. Since the spins move between the application of the two gradients, each spin experiences a slightly different applied gradient strength each time and the spins do not successfully rephase, causing signal attenuation¹⁶⁰. Because of this, the resulting diffusion-weighted image displays low signal intensity in regions of high diffusion along the diffusion gradient¹⁵⁸. The amount of signal attenuation is dependent on how far the molecule travels between the application of the two gradients and can be described by Equation 1-7¹⁵⁶:

$$M_{(b,TE)} = M_0 e^{-TE \times T_2} e^{-b \times D} \quad \mathbf{1-7}$$

Where $M_{(b, TE)}$ represents the magnetization at a specific b-value and echo time, M_0 represents the original magnetization, TE is the echo time, T_2 is the transverse relaxation constant, D is the apparent diffusion coefficient, and b represents the “b-value” used to describe the strength of diffusion gradients. The b-value is proportional to the squares of the duration and amplitude of the applied gradient and the time delay between the two diffusion gradients¹⁵⁹. A fully accurate calculation of the b-value should include contributions from other gradients used in imaging, such as the readout gradient, but these effects are usually overshadowed by the diffusion-weighted gradients at sufficiently high b-values. The degree of diffusion weighting is dependent on the b-value, where a higher b-value results in a more pronounced diffusion-related signal attenuation¹⁵⁹. Therefore, the signal attenuation displays a mono-exponential decay with respect to b-value that positively correlates with the diffusion coefficient¹⁵⁷. Different b-values may enhance different properties of the tissue. For example, longer intervals between gradients will increase the distinction between diffusion occurring in different directions¹⁵⁸.

If we assume the diffusion in the image can be described by a free diffusion model with a 3D isotropic Gaussian distribution, we can estimate the diffusion coefficient, referred to in this model as the apparent diffusion coefficient (ADC)¹⁵⁸. The ADC can be calculated from at least two measurements using Equation 1-8¹⁵⁸:

$$ADC = -b \times \ln \left(\frac{DWI}{b_0} \right) \quad \mathbf{1-8}$$

Here, DWI is the diffusion-weighted image intensity for a b-value, b, and b_0 represents signal from a reference image with no diffusion weighting¹⁵⁸. The ADC is dependent on the direction of diffusion encoding. To overcome this directional dependence, three orthogonal measurements may be applied and averaged in the calculation of ADC¹⁵⁸. Tissues with more restricted diffusion appear hypointense on an ADC map, allowing for

a more intuitive interpretation compared to DWI¹⁵⁹. The ADC provides limited information, especially in anisotropic anatomy like axon bundles in the brain¹⁵⁸. More advanced techniques that account for greater degrees of freedom, including diffusion tensor imaging, q-Ball imaging, and diffusion spectrum imaging, make use of longer acquisitions and more complex postprocessing to gain information about the orientation and anisotropy of diffusion¹⁵⁸.

Clinical use of DWI became possible in the 1990s with the availability of echo-planar imaging (EPI), which provided a fast sequence that negated issues associated with motion artifacts¹⁵⁹. Pathologic processes that alter the structural organization on a cellular level are targets of diagnosis via DWI technology¹⁵⁶. Water diffusion can be modulated by cell density, cell membrane orientation, or cell size; for example, cell swelling as observed in stroke¹⁶¹. DWI is commonly used in brain imaging and has been used to improve knowledge of brain connectivity and research conditions including multiple sclerosis, dyslexia, schizophrenia, and trauma^{156,162}. DWI has also been implemented clinically for use in identifying ischemia *in vivo* and has had a large clinical impact in the management of stroke^{156,162}. DWI is widely used to detect metastases in areas including the breast, prostate, and liver¹⁶². While uncommon, recent studies have applied DWI to study the placenta in human and animal models to measure blood movement through the placenta to the fetus¹⁶³.

DWI is limited in its accuracy and image quality because the algorithms used in reconstruction make assumptions that do not hold in reality, including perfect field homogeneity, infinitely fast gradient changes, and perfectly shaped RF pulses¹⁵⁹. DWI is susceptible to artifacts such as ghosting, blurring, and distortions¹⁵⁹. T₂ shine-through may occur from tissues with long T₂ times that retain signal on high b-value images, resulting in artificially bright signals on ADC maps¹⁵⁹. Conversely, the T₂ blackout effect results in low signals on an ADC map in regions with very low T₂ signal, for example areas lacking water protons, that may mask the diffusion sensitivity¹⁵⁹. The reproducibility of ADC values is questionable, as DWI typically suffers from low SNR and artifacts common to single-shot EPI sequences¹⁵⁹. The implementation of non-EPI sequences for DWI has helped to overcome some of these limitations¹⁵⁹.

1.3.5.1 Intravoxel Incoherent Motion (IVIM)

It has been acknowledged that the ADC model describing a mono-exponential relationship between the DWI signal and b-value does not perfectly describe the behaviour of water in tissue¹⁶⁴. A more appropriate and sophisticated model, referred to as intravoxel incoherent motion (IVIM), can separate the DWI signal into two mechanisms – diffusion and perfusion¹⁶⁵. The concept behind IVIM was introduced in 1986 when it was discovered that the collective low velocity motion of blood in randomly oriented capillaries mimics the diffusion process¹⁶⁵. IVIM enables the estimation of quantitative parameters that independently reflect tissue diffusivity and microcapillary perfusion without the need for novel DWI sequences or contrast agents^{157,164}.

At low b-values (0-100 s/mm²), the measured signal attenuation in DWI results from water diffusion in tissues and blood within the capillary network¹⁶⁴. Since the blood perfusing these capillaries does not move in a coherent orientation, it can be thought of as “pseudo-diffusion” that depends on the velocity of the flowing blood and the vascular architecture¹⁶⁴. The amount that the pseudo-diffusion effect contributes to the signal attenuation is dependent on the b-value and, as opposed to ADC estimation, a larger number of b-values are required to estimate the pseudo-diffusion coefficient (D^*)¹⁶⁴. Conveniently, D^* is close enough to D to be sensitive to DWI, resulting in a signal decay sensitive to tissue diffusion and blood microcirculation¹⁵⁷. Due to the comparatively faster velocity and larger displacement of molecules in the microvasculature during gradient application, the signal attenuation from pseudodiffusion is an order of magnitude greater than that from tissue diffusion¹⁶⁴. This means that at sufficiently high b-values ($b > 100$ mm/s), the measured signal attenuation is mostly or completely a result of the tissue diffusion, and at these b-values, the ADC is approximately equal to D (Figure 1.12)¹⁶⁴.

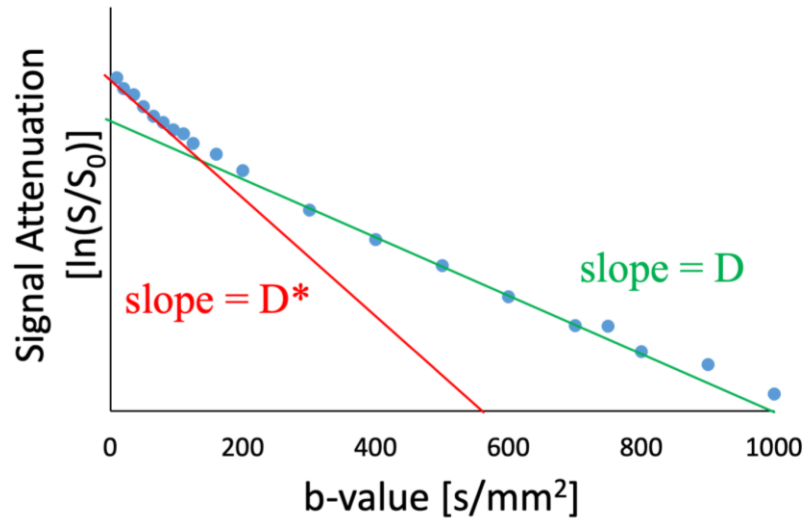


Figure 1.12: Semi-log plot of the signal attenuation at different b-values that demonstrates the IVIM effect at low b-values.

Therefore, the IVIM model uses a biexponential function to describe the DWI data, assuming that the measured signal attenuation is due to a combination of tissue diffusion and perfusion effects¹⁶⁴. Equation 1-9 describes the biexponential decay of the MRI signal (S) from the original signal (S_0) at a certain b-value (b), where D represents the water diffusion coefficient in the tissue, D^* represents the pseudo-diffusion coefficient in the microvasculature, and f represents the perfusion fraction or fraction of signal attenuation resulting from perfusion in the microvasculature¹⁵⁷.

$$\frac{S}{S_0} = f \times e^{-b(D^*+D)} + (1 - f)e^{-b(D)} \quad \mathbf{1-9}$$

The perfusion fraction may be thought of as the percent of a voxel volume occupied by capillaries and is used to describe the vascularity of the tissue¹⁶⁴. Fitting the MRI signal to this equation at multiple b-values allows for the estimation of D , D^* , and f , which can each be used to construct parametric maps¹⁶⁴.

For this technique to be useful clinically, it must be used in regions of the body that display a bi-exponential response to DWI¹⁶⁴. IVIM may have a clinical application as an alternative to perfusion MRI in patients with contraindications to contrast agents¹⁶¹. Perfusion imaging is important for evaluating microstructure heterogeneity and

angiogenesis¹⁵⁷. The most studied and promising clinical application of IVIM is in oncology, as a collection of research has shown that IVIM measurements demonstrate distinct characteristics in tumours and may be used to monitor treatment efficacy¹⁵⁷. Tumours in the prostate, breast, kidneys, pancreas, liver, and head and neck regions have been identified as potential diagnostic targets of IVIM as they display distinct D , D^* , and/or f values compared to healthy tissue in these areas^{157,161,164}. In the liver, IVIM has been used to identify fibrosis and cirrhosis, highlighting its potential use in identifying D^* as a biomarker of NASH^{157,164}. IVIM is particularly useful in the kidneys as diffusion parameters can differentiate between the cortex and medulla and may also be used to predict renal function¹⁶⁴. IVIM is sensitive to flow other than blood and may be used to investigate tubular flow in the kidneys, though it may be difficult to disentangle this signal from the microvascular flow¹⁵⁷. Any type of active transport from glandular secretion, including breast ducts, salivary glands, and pancreas glands, may be a target of investigation using IVIM¹⁵⁷. Like DWI, an obvious application of IVIM is studying the brain, as regional cerebral blood flow is closely related to functional brain activity and may be useful in studies focusing on trauma or stroke¹⁶⁶. IVIM techniques may also be used in conjunction with functional MRI (fMRI) by removing blood flow effects to improve the spatial resolution of activation maps¹⁶⁵.

There are some limitations to IVIM, including reproducibility issues as there is no consensus on the number of b -values that should be used for measurement¹⁶⁴. The MRI platform must allow for customized b -values during acquisition, as IVIM requires multiple low b -values to avoid errors and SNR variations¹⁶⁴. IVIM has a variable sensitivity to vessel size, which should also be considered when selecting b -values for different regions in the body¹⁶¹. More sophisticated data processing may help decrease uncertainty in parameter estimation and lead to shorter acquisition times^{161,164}. To provide more useful quantitative information, the relationship between IVIM parameters and blood volume and flow estimates from gold-standard approaches must be clarified¹⁶¹. This quantification may not be straightforward as the perfusion fraction measured with IVIM is likely influenced by other physiologic processes such as glandular secretion and ductal flow that may be difficult to isolate from the microvasculature contribution¹⁶⁴. Future work related to IVIM includes manipulating this technique for application in MR

elastography to measure tissue shear stiffness and angiography to detect laminar flow in larger vessels¹⁵⁷.

1.3.6 T_2^* MRI

When imaging physiological tissue, local B_0 inhomogeneities and differences in magnetic susceptibilities within the tissue result in a shortened T_2 relaxation time, known as the apparent transverse relaxation time, T_2^* (Figure 1.13)¹³⁰. This effect is caused by variations in the local magnetic field that randomly cause nuclei to experience phase shifts and local diffusion, leading to accelerated phase incoherence and transverse relaxation¹⁶⁷. While it may seem that correcting for T_2^* in images would be beneficial to measure T_2 , T_2^* is useful in itself for measuring functional parameters such as blood oxygen saturation. Oxyhemoglobin is weakly diamagnetic and does not produce a magnetic moment, while deoxyhemoglobin is paramagnetic due to the presence of four unpaired electrons¹⁶⁸. As paramagnetic substances cause local field distortions, the T_2^* is shortened by the presence of deoxygenated hemoglobin in the blood, which causes detectable susceptibility changes within vessels that have high concentrations of deoxyhemoglobin¹²⁶. Therefore, on a T_2^* -weighted image, areas with a concentration of deoxygenated blood appear dark¹³¹. T_2^* maps can also be produced where the T_2^* value is quantitatively measured and mapped to each voxel in the image¹³¹. Unlike spin echo sequences that eliminate effects of field inhomogeneities with the 180° refocusing pulse, gradient echo sequences do not correct for this effect and therefore depend on T_2^* ¹³¹. T_2^* weighting may be emphasized by acquiring an image using a small flip angle, long TR, and long TE^{126,131}.

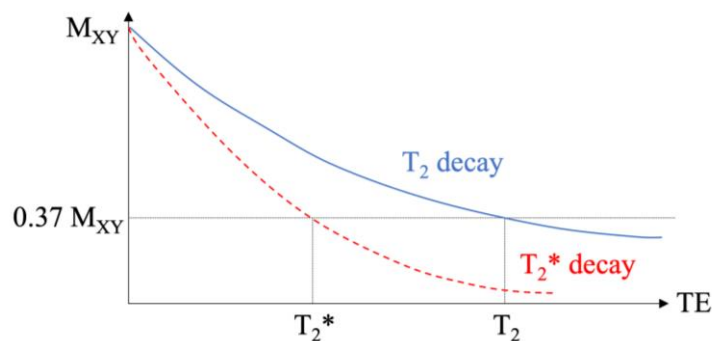


Figure 1.13: Graph of T_2 and T_2^* relaxation curves.

It should be noted that blood oxygenation is also related to the inherent T_2 , as the transverse relaxation rate ($1/T_2$) has a quadratic dependence on deoxyhemoglobin fraction¹⁶⁹. This quantitative relationship has been validated using *in vivo* animal studies over multiple oxygenation conditions¹⁶⁹. T_2 measured with a SE sequence is sensitive to spin diffusion caused by the field inhomogeneity, whereas T_2^* measured using a GE sequence is sensitive to spin dephasing and spin diffusion¹⁶⁹. Because of this, measurable T_2^* changes can be detected from smaller variations in blood oxygen saturation, making T_2^* the more sensitive and preferred method of detection for many oxygenation studies¹⁶⁹, including the work presented in Chapter 4 of this thesis.

Although T_2^* is primarily dependent on oxygenation, it is also affected by tissue characteristics, including villus density, inhomogeneous distribution of oxygenated blood, and the presence of other paramagnetic molecules¹⁶⁷. Furthermore, the T_2^* signal is affected by macroscopic field inhomogeneities, such as magnet imperfections, poor shimming, and tissue-air interfaces that should be taken into account if possible¹⁷⁰. Therefore, T_2^* alone cannot be used as a direct quantitative measure of blood oxygen saturation, but rather as an indirect measure of changes in blood oxygen saturation *in vivo*¹⁶⁹. T_2^* is dependent on the blood oxygen saturation and partial pressure of oxygen in and around the blood vessels, both of which are useful quantitative measures related to oxygen availability *in vivo*¹⁷⁰. Quantification of these measurements is possible through animal and *ex vivo* studies that account for factors such as the hemoglobin concentration, blood flow, and blood volume fraction within each voxel¹⁷⁰⁻¹⁷².

There are many clinical applications of T_2^* -weighted MRI and T_2^* mapping for detecting hemoglobin oxygenation levels throughout the body. One focus of this application is in myocardial imaging to detect damage due to infarction and differentiate between irreversible necrosis and reversible oedema that would benefit from restoring perfusion to the area¹⁷³. T_2^* has been used in placental imaging to detect baseline differences in oxygenation between fetal and maternal areas, differences between normal and dysfunctional placentae¹⁶⁷, and to evaluate the placenta's response to hyperoxygenation¹⁷². Other than detecting blood oxygen saturation, T_2^* -weighted

imaging may be used to visualize hemorrhage, arteriovenous malformation, cavernoma, thrombosed aneurysm, calcification, and iron deposits in various tissues¹³¹.

The relationship between dynamic changes in T_2^* as a response to neural activity is termed the blood oxygenation level-dependent (BOLD) effect and was first observed in the 1990s¹²⁶. BOLD contrast reflects changes in cerebral blood volume, blood flow, and oxygen consumption¹³⁰. The BOLD effect is the backbone of fMRI work, the most common application of T_2^* -based imaging¹²⁶. In fMRI studies, the relative local change in the raw T_2^* -weighted signal is measured over time to visualize the increased cerebral blood flow in response to neuronal activity in a region of interest in the brain^{131,167}. Quantitative BOLD techniques utilize complex biophysical modelling to distinguish information from cerebral venous blood volume oxygen saturation¹⁷⁴.

The long TEs required for T_2^* -weighted imaging pose technical difficulties arising from body motion and pulsatile blood flow¹⁶⁹. Despite any challenges in applying this technique, T_2^* MRI provides an alternative imaging method to positron emission tomography (PET) for mapping blood oxygenation that does not require ionizing radiation and is more widely available¹⁷⁴. T_2^* imaging also provides advantages over the standard procedure of pulse oximetry, which is limited to superficial capillary sampling and invasive blood sampling, which poses risks when used to gather information about deep vessels¹⁶⁹.

1.3.7 Hyperpolarized MRI

Imaging metabolic biomarkers provides the opportunity to probe the state of a biological system. Although MRI is often used to detect signal from the ^1H nuclei on water molecules, this technology can detect signals from other nuclei, potentially enabling imaging of metabolically important biomolecules. For many reasons, non-hydrogen MRI is challenging. Firstly, hydrogen has the highest gyromagnetic ratio of all magnetically sensitive, stable nuclei. This makes other NMR-sensitive nuclei challenging to use for MR imaging as, compared to hydrogen nuclei, they have smaller polarizations. While spectroscopy, especially at ultra-high field strengths, may be possible using lower γ

nuclei, imaging requires faster acquisitions at lower, clinical field strengths, making *in vivo* non-proton imaging difficult¹³⁷.

Secondly, as human bodies are composed of approximately 75% water, the concentration of hydrogen nuclei dominates the concentration of other nuclei in the body. While ¹⁵N is present in many biochemically interesting molecules, these metabolites exist in concentrations below thresholds necessary for detection using traditional MRI methods¹⁷⁵. One may assume carbon would be high enough in concentration due to the large number of hydrocarbons present in living systems; however, the natural abundance of the magnetically sensitive ¹³C isotope is only 1%. In contrast, hydrogen has almost 100% abundance of its magnetically sensitive isotope ¹H. Combining the low abundance of ¹³C with its low γ , thermal NMR measurements of ¹³C can only achieve 0.0176% of the sensitivity of ¹H¹⁷⁶. Despite these limitations, non-proton MRI has long been desired as a method to detect specific enzyme-catalyzed biological reactions as altered metabolism is central to many human diseases, including cancer, cardiovascular disease, diabetes, and a variety of inflammatory conditions^{175,177}. Attempts have been made to increase NMR sensitivity for non-proton nuclei to make non-proton MRI a practical clinical imaging tool.

A successful method of boosting the MR signal of nuclei is external nuclear polarization, otherwise known as hyperpolarized MRI (HP MRI)¹²⁴. Hyperpolarization is a process in which nuclei are aligned to a polarization many orders of magnitude greater than what would normally be possible at thermal equilibrium *in vivo*¹²⁴. If the hyperpolarized state can be maintained long enough for uptake and metabolism in cells at the site of interest, the hyperpolarized probe may be useful for qualitative and quantitative measurements of *in vivo* metabolism in various applications. A few methods may be used to boost the signal of these nuclei temporarily. Some methods are unique to hyperpolarized gases and some are used for liquid solutions containing hyperpolarized nuclei. Hyperpolarization methods most commonly used in preclinical and clinical studies include spin-exchange optical pumping (SEOP), parahydrogen induced polarization (PHIP), signal amplification by reversible exchange (SABRE), and dissolution dynamic nuclear polarization (d-DNP)¹⁷⁸.

SEOP methods are used to produce hyperpolarization in noble gases, most commonly in ^3He and ^{129}Xe ¹⁷⁹. The SEOP method uses circularly polarized resonant light aimed at the vapour of an alkali metal in a glass cell to transfer the photons' spin angular momentum absorbed by the metal vapour to the alkali metal atoms¹⁷⁹. This transfer produces spin polarization in the valence electrons of these atoms via optical pumping¹⁷⁹. The setup also contains a large amount of the target noble gas to facilitate collisions between the alkali metal atoms and noble gas atoms that result in a transfer of the electron-spin polarization to the nuclei of the noble gas¹⁷⁹.

PHIP is a polarization method that relies on the pairwise incorporation of hyperpolarized parahydrogen (H_2 with proton spins in opposing directions) into the molecule of interest, usually across unsaturated chemical bonds¹⁸⁰. PHIP does not require the use of radicals, and instead, proton hyperpolarization is transferred to carboxyl ^{13}C using RF-based or field-cycling approaches¹⁷⁸. An advantage of PHIP is that it can be achieved quickly, with hyperpolarization transfer occurring in a matter of seconds, and it may be stored for months at room temperature¹⁷⁸. PHIP is limited in its application as it is confined to use in probes that are unsaturated and have appropriate symmetry to incorporate the parahydrogen into the molecule structure¹⁸⁰.

SABRE is related to PHIP but differs in technique as the parahydrogen does not chemically react with the target molecule¹⁸¹. Instead, the parahydrogen and substrate are brought into temporary contact via a transition metal-based host¹⁸¹. In this state, the high spin order of parahydrogen is transferred to net polarization in a matter of seconds when exposed to a sudden change in the external magnetic field¹⁸². Though promising, the SABRE technique, introduced in 2009, is relatively new and d-DNP remains the most commercialized and utilized polarization technique for liquid-state probes.

The final polarization method, d-DNP, is the hyperpolarization technique used in Chapters 2 and 3 of this thesis. This technique involves the transfer of polarization from unpaired electrons to the target nuclei via low temperatures (near absolute zero) and strong static magnetic fields¹⁸³. To facilitate this, a stable free radical is mixed in a solution with the biomolecule probe to produce a glass matrix at a temperature $\sim 1\text{ K}$

inside a magnetic field of $\sim 3\text{-}5\text{ T}^{184}$. A high-powered microwave then irradiates the glass matrix at the electron resonant frequency to enable the transfer of the spin polarization from electrons to the nuclei of interest in the solid state¹⁸⁴. Finally, the solid-state solution is rapidly dissolved and warmed, ready for injection into the subject and subsequent imaging¹⁸⁴. d-DNP methods have been shown to increase polarization by 10,000 in liquid state NMR¹⁸⁴.

HP MRI is limited in the types of probes that may be used for imaging. The nuclei must be stable and able to produce net magnetization in an external magnetic field¹²⁴. The target nuclei must also be isolated from other magnetic moments, such as unpaired electrons (i.e. O_2) or other magnetic nuclei on the molecule to prevent loss of alignment with the external magnetic field¹²⁴. Target nuclei found *in vivo*, such as ^1H , ^{13}C , ^{15}N , and ^{31}P , are obvious choices for biological applications of HP MRI¹²⁴. If needed, these nuclei may be incorporated onto endogenous biomolecules via isotope enrichment (Figure 1.14). These hyperpolarized biomolecule probes may then be administered to the subject at near or supra-physiological concentrations without negative effects and provide information on native metabolic processes *in vivo*¹⁸⁵. Non-toxic molecules such as ^{19}F and ^{29}Si may also have application for HP MRI, and inert gases ^3He and ^{129}Xe are chosen as target nuclei for HP imaging of airways¹²⁴.

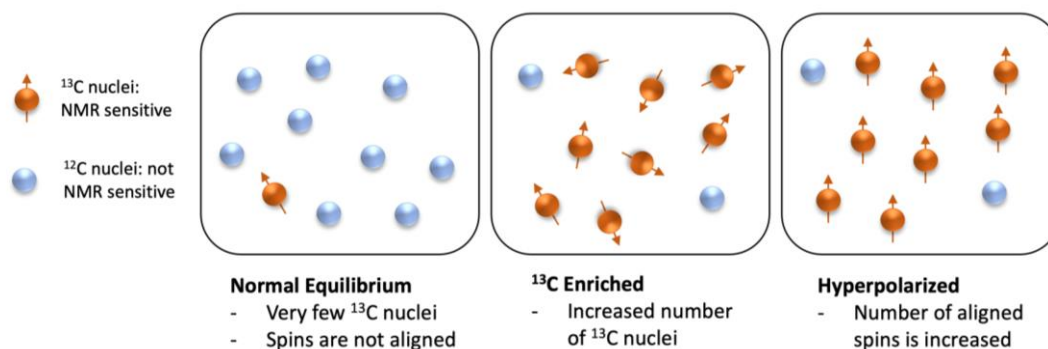


Figure 1.14: Example of the enrichment of NMR-sensitive nuclei followed by hyperpolarization

The HP probe must be selected to be biologically relevant, have the capacity to attain high polarization levels, and have relatively long T_1 decay constants¹⁷⁸. T_1 decay is an important factor for probe selection as there is a lower limit to the time scale required for image acquisition, and the rate of decay impacts the choice of acquisition techniques,

suitability for 3D imaging, and image quality¹⁷⁸. Biologically relevant applications of the probes may vary and can include measurement of cellular uptake, metabolic pathway kinetics, redox state, ion concentrations, pH, drug efficacy, or oncologic signalling¹⁸⁶. Metabolically active probes such as ¹³C-enriched pyruvate may be used to acquire signals from both the injected molecule and its downstream metabolites, as the hyperpolarized nuclei are transferred between metabolites *in vivo*¹⁸⁵. The known chemical shifts of each metabolite may be used to separate their acquired signals during image reconstruction using chemical shift imaging or CSE-MRI techniques¹⁸⁵.

Hyperpolarized MRI technology is often compared to nuclear medicine imaging modalities such as PET, as both are functional imaging methods used to probe biodistribution and cellular uptake of biologically relevant molecules *in vivo*. Like PET, HP MRI requires anatomic reference images¹⁴⁴ and conveniently, anatomic MRI acquisitions may be performed during the same exam and patient setup to allow for simple image registration. Using MRI for reference images also has the advantage of excellent soft-tissue contrast to localize metabolically active regions indicated by HP MRI. PET exhibits some benefits over HP MRI, including its sensitivity to nanomolar concentrations of tracer, allowing for administration of a very small amount of radiotracer that is unlikely to affect *in vivo* metabolism¹⁸⁷. HP MRI has some advantages over PET, as it does not produce ionizing radiation, enabling safety for use in vulnerable populations, including children and pregnant women¹⁷⁷. Additionally, unlike HP MRI, PET techniques are limited to providing information on the uptake and perfusion of the injected biomolecule and cannot provide information on the downstream metabolites of the probe¹⁷⁷. Combining HP MRI and PET information may prove beneficial as the two methods provide complementary information, especially in cancer metabolism¹⁸⁸. At centers that possess the equipment necessary for HP MRI and PET, it is estimated that the cost of clinical administration of these exams would be similar, negating any financial advantages of either technology¹⁷⁷.

Although the concept behind d-DNP was first explored in 1953¹⁸⁹, technological advancements in the construction of compact, high strength magnets have only recently made commercially available polarizers a reality, including polarizers capable of

producing sterile injections suitable for clinical use¹⁹⁰. Though not yet a routine clinical imaging modality, HP MRI has been used in clinical studies since 2013¹⁹¹. Even after almost a decade of clinical studies, HP technology is still in its infancy, and polarizer methods should continue to be optimized for cost-effective, reliable polarizations that can be achieved faster and at higher levels of polarization¹⁸⁸. Other improvements that should be prioritized are methods for prolonged storage of HP probes, enriched probes with longer T₁s, and established routine protocols for quality assurance, calibration, and data analysis¹⁷⁵. Improvements in hardware, including commercially available dual-tuned MRI coils and higher performance gradients, would also be beneficial for advancing the field of HP MRI¹⁸⁸. Novel techniques to improve acquisition speed, spatial and temporal resolution, and motion are still being developed to improve HP MRI's feasibility in clinical settings¹²⁴. Additionally, kinetic modelling techniques are being explored and improved upon to obtain quantitative information related to metabolic rates and uptake; external validation of these measurements using *ex vivo* samples is integral to highlighting the clinical use of quantitative HP MRI¹⁷⁵. Moving forward, it will be necessary to continue publishing literature concerning the biomedical value and specific human applications of HP MRI to encourage further support of translating this modality to eventual clinical use.

1.3.7.1 Hyperpolarized Pyruvate MRI

Projects described in Chapters 2 and 3 specifically utilize hyperpolarized MRI to gain information about pyruvate's biodistribution and metabolism *in vivo*. Pyruvate is an end product of glycolysis, which involves the metabolism of glucose – a simple sugar and the most abundant monosaccharide carbohydrate^{14,192}. Glucose is the most important energy source in all organisms, and dietary glucose may be sourced from many fruits, vegetables, and grains¹⁹². Pyruvate is less commonly generated via the oxidation of lactate, transamination of alanine, or conversion from malate^{14,193}. Pyruvate is a key molecule in cellular energy production and is critical for mitochondrial ATP production¹⁴. Normally, pyruvate enters the mitochondrial matrix where it is converted into acetyl coenzyme A (acetyl-CoA) via pyruvate dehydrogenase (PDH) or oxaloacetate via pyruvate carboxylase, which may both enter the tricarboxylic acid (TCA) cycle,

otherwise known as the citric acid cycle or Krebs cycle, to generate ATP via oxidative phosphorylation¹⁹³. Under anaerobic conditions, pyruvate may be reduced to lactate in the cytosol via lactate dehydrogenase (LDH), which also produces NAD⁺ from NADH¹⁹⁴. NAD⁺ is necessary to maintain glycolysis, and as such, the conversion of pyruvate to lactate indirectly facilitates energy production via the promotion of anaerobic glycolysis, though this method of energy production is less efficient than the TCA cycle¹⁹⁴.

There are two carbons on the pyruvate molecule that may be enriched with a ¹³C nucleus and used for HP MRI. The choice of which carbon is targeted will determine which metabolites the enriched carbon is transferred to and subsequently which energy production pathways may be understood via imaging. Focusing on ¹³C enrichment of the C2 atom on pyruvate, we can probe information on the oxidative phosphorylation pathway and specifically the TCA cycle where [2-¹³C]pyruvate and its downstream metabolites [2-¹³C]lactate, [1-¹³C]citrate, [1-¹³C]acetyl-carnitine, and [5-¹³C]glutamate contribute to the MRI signal^{124,195,196}. Acetyl-CoA retains the enriched C2 nuclei from pyruvate and may be metabolized into acetyl-carnitine, which does not enter the TCA cycle, or citrate, an intermediate of the TCA cycle that goes on to be metabolized into α -ketoglutarate. α -ketoglutarate is in metabolic flux with glutamate, which exits the TCA cycle¹⁹⁷. TCA cycle intermediates including acetyl-CoA and α -ketoglutarate carry the enriched C2 nuclei but suffer from a low signal that is not typically sensitive enough for MRI detection. Both C1 and C2-enriched pyruvate may be used to detect signal from the amino acid alanine, which is synthesized from pyruvate via the ALT enzyme^{176,198}. Alanine is usually produced in lower quantities than lactate; however, pyruvate's conversion to alanine is a useful biomarker for tissues in the liver and skeletal muscles heavily involved in alanine metabolism¹²⁴. A limited number of studies have focused on using HP [2-¹³C]pyruvate MRI due to the relatively low oxidative phosphorylation activity in many tissues, resulting in low signal and difficulty imaging these TCA cycle intermediates¹²⁴.

Due to its longer T₁ and higher capacity for polarization, [1-¹³C]pyruvate is the most common probe used in hyperpolarized MRI¹²⁴. Chapters 2 and 3 focus on [1-

^{13}C]pyruvate HP MRI, allowing us to gain information on three main metabolic fates of the pyruvate molecule, as demonstrated in Figure 1.15. Similar to $\text{C}2$ -enrichment, the $\text{C}1$ -enriched nuclei provides signal from lactate and alanine. In this case, the signal is provided by the $\text{C}1$ -enriched carbon on these molecules¹⁹⁸. Since the $\text{C}1$ nucleus is not transferred to acetyl-CoA, it does not flow into the TCA cycle, preventing direct detection of downstream metabolites in the TCA cycle¹⁹⁹. Instead of being carried to acetyl-CoA, the $\text{C}1$ from pyruvate is transferred to carbon dioxide during this reaction and is then rapidly converted to bicarbonate. $[1-^{13}\text{C}]$ bicarbonate can be measured with HP MRI, giving us an indirect measure of the proportion of pyruvate being used to drive the TCA cycle¹⁸⁸.

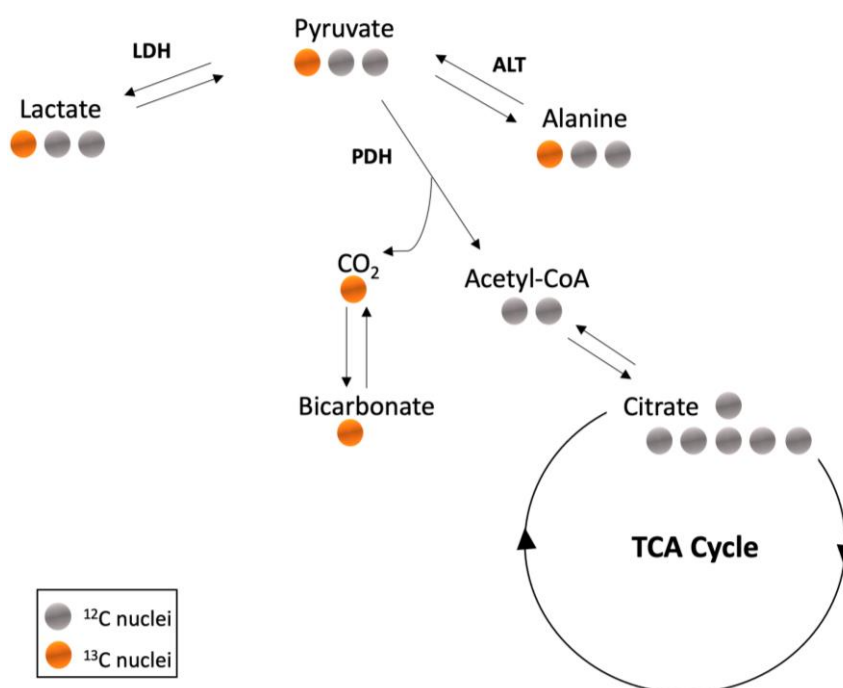


Figure 1.15: Schematic of pyruvate metabolism highlighting the fate of the $[1-^{13}\text{C}]$ pyruvate nuclei

It should be noted that $\text{C}1$ may enter the TCA cycle through other means, specifically pyruvate's conversion into oxaloacetate, which may then be converted to aspartate and exit the TCA cycle or be converted to other TCA cycle intermediates – malate and fumarate¹⁸⁵. Due to the short T_1 and/or rapid metabolism of these biomolecules, their signal is not usually visible with HP MRI, and applications primarily focus on imaging pyruvate, lactate, alanine, and bicarbonate¹⁸⁸. Signal from these metabolites may be used

to estimate metabolic kinetics, including modelling metabolic rate constants associated with the enzymatic activities of PDH, LDH, and ALT *in vivo*²⁰⁰. Quantification of these constants from imaging data is complex, with many uncertainties including polarization levels, B₁ inhomogeneity, transmitter/receiver gain settings, and T₁ relaxation²⁰⁰. There is currently no consensus on the best method of quantifying HP metabolic data, and this remains a future goal of HP [1-¹³C]pyruvate MRI²⁰¹.

There are many HP [1-¹³C]pyruvate MRI applications, with the majority of projects centred around tumour detection and characterization, as the Warburg effect causes altered and distinct glucose metabolism in cancer cells²⁰². Specifically, the Warburg effect is a hallmark of cancer, presenting as a shift from aerobic to anaerobic metabolism in tumour cells as tumours expand beyond the local blood supply's perfusion and oxygenation capabilities and rely on anaerobic glycolysis for cellular energy production²⁰². The first human study involving hyperpolarized [1-¹³C]pyruvate MRI was done in prostate cancer patients in 2013 and demonstrated successful translation of this technology to clinical research. This study confirmed increased lactate production as a characteristic of tumour cells while also demonstrating this technique's safety in human patients¹⁹¹. Preclinical studies using HP [1-¹³C]pyruvate MRI have identified lactate and alanine as potential biomarkers for prostate cancer, and the lactate/pyruvate ratio has been correlated with tumour grade in the prostate^{124,203}. Other sites targeted for tumour detection and treatment response include the brain, kidneys, and breast¹²⁴.

Although tumour imaging is the most popular application of HP [1-¹³C]pyruvate MRI, the probe has also been used to characterize metabolic patterns in models of acute injury, inflammation, and normal *in vivo* metabolism. HP [1-¹³C]pyruvate MRI has been used to examine the metabolic profile of a healthy heart and changes to this profile in cardiac ischemia cases, resulting in increased lactate and decreased bicarbonate production¹²⁴. In addition to brain cancer, HP MRI has been used to characterize metabolic changes occurring in post-traumatic brain injuries, with findings of lowered bicarbonate production suggesting impaired mitochondrial pyruvate metabolism due to local decreases in aerobic respiration²⁰⁴. The kidneys typically have a high ¹³C signal as they receive 20% of the cardiac output, making them a target for HP [1-¹³C]pyruvate MRI to

study the metabolism of healthy kidneys and metabolic changes with respect to blood glucose levels in diabetes¹²⁴. The liver is another target for [1-¹³C]pyruvate as it is the most metabolically active organ in the body, and pyruvate metabolism has been used to probe information about hepatic tumours and non-alcoholic fatty liver disease²⁰⁵. HP inert gases are commonly used for imaging the airways, but HP [1-¹³C]pyruvate has also been used in the lung as an angiography tool for pulmonary vasculature. Since HP [1-¹³C]pyruvate MRI of the lung is challenging due to low tissue density, B₀ inhomogeneity, and motion, most studies are done on *ex vivo* perfused lung models of ischemia and reperfusion¹²⁴. HP [1-¹³C]pyruvate MRI has also been used in unique applications such as monitoring placental metabolism²⁰⁶. Lastly, skeletal muscle metabolism may be probed using HP [1-¹³C]pyruvate MRI and used for comparison with metabolic profiles in other organs or functional experiments of muscle activation¹²⁴.

1.4 Thesis Outline

This thesis is motivated by a need to understand the complex and often unknown effects of diet on the body, particularly in relation to liver and placental function. Advanced MRI techniques capable of providing structural and functional information about the areas of interest were employed in an animal model of Western diet-induced metabolic disease. The main objective of this thesis was to investigate the effects of the WD on anatomy *in vivo*, using a variety of measurements. Technical improvements in cutting-edge hyperpolarized MRI were applied to improve the investigation of *in vivo* metabolism in real time. The major themes of this thesis are represented in Figure 1.16.

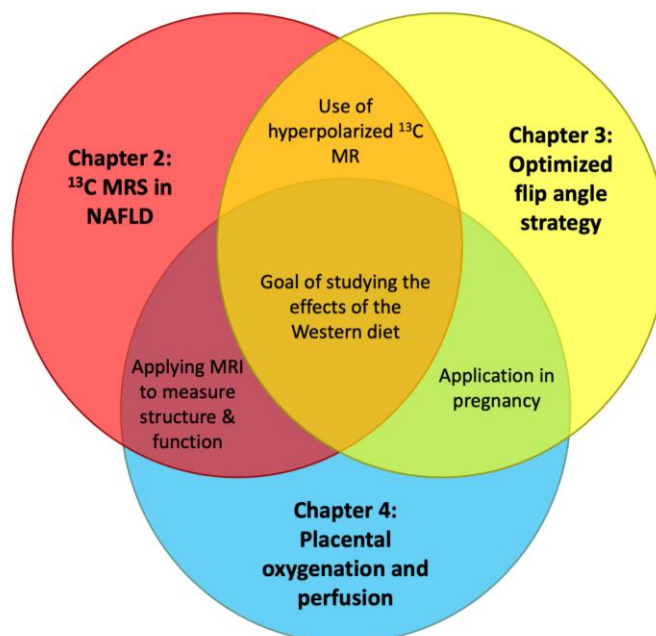


Figure 1.16: Venn diagram of major themes of this thesis represented in each project

Chapter 2 of this thesis presents work adapted from an original research manuscript entitled “In vivo magnetic resonance spectroscopy of hyperpolarized [1-¹³C]pyruvate and proton density fat fraction in a guinea pig model of non-alcoholic fatty liver disease development after lifelong Western diet consumption”¹. The purpose of this project was to use hyperpolarized MRS and PDFF measurements to investigate the effects of a chronic, lifelong exposure to the WD in a guinea pig model resulting in non-alcoholic fatty liver disease. It was hypothesized that the WD would result in the development of NAFLD in association with altered pyruvate metabolism. Animals fed a lifelong WD had increased PDFF in the liver and demonstrated abnormal hepatic pyruvate metabolism indicated by an increased rate of lactate production. PDFF and HP MRS results were significantly correlated with *ex vivo* measurements of TG concentration and enzyme activity.

Chapter 3 is adapted from an original research article entitled “Optimizing SNR for multi-metabolite hyperpolarized carbon-13 MRI using a hybrid flip-angle scheme”². This project aimed to improve the SNR of hyperpolarized ¹³C MRI of [1-¹³C]pyruvate. This was achieved using a multi-spectral variable flip angle (msVFA) scheme where the spectral profile and flip angle varied dynamically with time to be optimized for each

metabolite. The novel msVFA scheme was compared to a constant flip angle (CFA) scheme through simulations and *in vivo* experiments in pregnant guinea pigs where regions of interest were placed in the placenta, maternal liver, and maternal kidneys. *In vivo* experiments showed significant increases in SNR using the msVFA technique relative to CFA for all metabolites and regions of interest.

Chapter 4 of this thesis describes an original research project prepared as a manuscript for submission to a peer-reviewed scientific journal titled “Perfusion and oxygen saturation of the mid-pregnancy and near-term placenta measured by magnetic resonance imaging in a guinea pig model of pregnancy following lifelong Western diet consumption”. The purpose of this work was to investigate the effect of a lifelong maternal WD exposure on placental structure and function at mid- and near term in a guinea pig model of pregnancy. T_2^* mapping and diffusion-weighted imaging techniques were applied to gain information on placental oxygen saturation, diffusion, and perfusion *in vivo*. Sows fed a lifelong WD displayed higher placental perfusion, lower placental oxygen saturation, and decreased placental efficiency compared to sows on a control diet. These results suggest that hypoxic conditions induced by the WD led to placental vascular adaptations resulting in increased blood perfusion at mid-gestation and improved oxygen saturation at late gestation.

Chapter 5 concludes this thesis with a summary of the work presented within and suggestions for future work related to this thesis.

Chapter 2

2 **In vivo magnetic resonance spectroscopy of hyperpolarized [1-¹³C]pyruvate and proton density fat fraction in a guinea pig model of non-alcoholic fatty liver disease development after lifelong Western diet consumption**

2.1 Introduction

With increasing consumption of the 'Western diet' (WD) that is high in fat and sugar, there has been a corresponding increased incidence of non-alcoholic fatty liver disease (NAFLD) and comorbidities in Western society in both lean and overweight/obese populations⁴⁴. NAFLD has become the leading cause of chronic liver disease in developed nations, imposing significant burdens on healthcare systems and decreasing overall life expectancy⁴⁴. The ability to non-invasively assess liver metabolism may provide a means of monitoring NAFLD severity as it has been reported that altered pyruvate metabolism, specifically increased lactate production, is an indicator of liver disease¹⁴. The increased production of lactate from pyruvate is an indication of the shift from oxidative metabolism to anaerobic glycolysis and is associated with liver damage²⁰⁷. Elevated lactate in the liver, induced by a high-fat diet, has been found in obese mice²⁰⁵ and may be linked to a disturbance in hepatic lipid synthesis²⁰⁸. The ability to measure lactate production *in vivo* would prove useful for observing NAFLD's effects on liver damage, stress, and lipid accumulation.

MRI is used to evaluate structure, function, and composition of organs, making it an ideal method for characterizing liver disease²⁰⁹. Chemical shift-encoded imaging is an MRI technique that can be used to separate signal from fat and water within the body, enabling *in vivo* measurements of fat fractions in the liver²⁰⁹. Additionally, MRI can detect signal from nuclei besides hydrogen, allowing for the selective imaging of certain biomolecules of interest²¹⁰. Carbon-13 (¹³C) magnetic resonance spectroscopy (MRS) has historically been used to investigate glycolysis but is limited by inherently low sensitivity and long

acquisition times²¹⁰. To address these limitations, hyperpolarized ^{13}C MRS is used to temporarily boost the signal-to-noise ratio, allowing for rapid acquisition of the spectroscopy signal from ^{13}C -enriched substrates¹⁵⁵.

By enriching pyruvate with ^{13}C and using hyperpolarized technology to significantly enhance the MR signal, it is possible to inject and subsequently image the distribution of $[1-^{13}\text{C}]$ pyruvate *in vivo* in real-time¹⁵⁵. Additionally, this technique allows us to simultaneously acquire and subsequently differentiate signals from the pyruvate molecule and its downstream metabolites that retain the ^{13}C nuclei over the acquisition duration¹⁵⁵. Concentrations and time curves of each metabolite can be quantified, allowing for examination of metabolic processes. Time-to-peak (TTP) is a quantitative indirect measurement of enzyme concentration as the temporal dynamics of the metabolic reactions are directly related to its concentration²⁰¹. Animal studies are crucial in understanding the fundamental biochemical properties of disease and in validating emerging technologies such as hyperpolarized MRI by correlating ^{13}C exchange rates with *ex vivo* measurements¹⁸⁸. Hyperpolarized $[1-^{13}\text{C}]$ pyruvate MRS has previously been used in a NAFLD rat model where both $[1-^{13}\text{C}]$ alanine and $[1-^{13}\text{C}]$ lactate were identified as potentially useful non-invasive markers of the progression of NAFLD²⁰⁵.

To study a model of NAFLD, guinea pigs were fed a WD previously shown to induce NAFLD without causing the accumulation of subcutaneous fat in this species⁸. Thus, this study aimed to validate MRI techniques used to investigate the effect of long-term WD consumption on liver metabolism in a pre-clinical guinea pig model of lean NAFLD and to investigate the hypothesis that exposure to the WD will result in NAFLD in association with altered pyruvate metabolism.

2.2 Methods

2.2.1 Ethical Approval

Animal care, maintenance, and procedures were performed following the national council's standards and guidelines on animal care. All procedures were reviewed, approved, and monitored by the institutional animal care and ethics committee.

2.2.2 Animal Model and Welfare

Guinea pigs were used in this study as they differ from other rodents as a model for NAFLD in that their lipoprotein metabolism and hepatic enzyme activity closely mimics human physiology¹¹⁸. Male Dunkin-Hartley guinea pig pups were born in-house to mothers fed a standard diet throughout gestation and lactation in a 12/12 hour light-dark schedule in individual cages. At approximately fifteen days postnatal (PN), pups were weaned onto their respective diets, feeding *ad libidum* in individual cages. Male guinea pig pups (matched for litter) were randomly weaned onto either a control diet (CD: 21.6% protein, 18.4% fat, 60% carbohydrates, n = 14) or WD (21.4% protein, 45.3% fat, 33.3% carbohydrates, n = 14)²¹¹. Percentages indicate the calorie contribution from each macronutrient to the total dietary calories. The fat content (CD: 3% SFA, 4% MUFA, 11% PUFA; WD: 32% SFA, 12% MUFA, 2% PUFA) and carbohydrate content (CD: 10% sucrose, 40% corn starch; WD: 19% sucrose, 6.5% fructose, 9% corn starch; % by weight) of the diets differed in terms of their compositions. The WD had a higher caloric density (4.2 vs 3.8 kcal/g) and included 0.25% cholesterol²¹¹. Daily food consumption (g/day/kg body weight) and animal weights were recorded for the 10 days before MRI scanning and during the period between MRI and euthanasia. At 144 days PN, animals underwent scanning (details below), and at approximately 150 days PN, animals were euthanised by CO₂ inhalation in a sealed chamber²¹². Blood samples were immediately collected from the descending vena cava and analyzed using VetScan VS2 Chemistry Analyzer (VetScan® Mammalian Liver Profile reagent, Abaxis, Union City, CA) to quantify levels of alkaline phosphatase (ALP), alanine aminotransferase (ALT), gamma glutamyl-transferase (GGT), blood ammonia (BA), bilirubin (TBIL), albumin (ALB), blood urea nitrogen (BUN), and cholesterol (CHOL). Livers were then harvested, weighed, snap-frozen in liquid nitrogen, and stored at -80°C until later biochemical determinations. Kidneys, brains, and hearts were harvested and weighed.

2.2.3 In Vivo Proton MRI Determination of Fat Content and In Vivo Measurements of Hepatic Metabolism with Hyperpolarized ^{13}C MRS

At 144 +/- 4 days PN (equivalent to ~ 18-22 human years²¹³), animals were imaged using a 3T MRI scanner (GE Discovery MR750; GE Healthcare, Waukesha, WI, USA) under anesthetic²⁰⁶. Animals were anesthetized using 4.5% isoflurane with 2L/min O_2 and maintained between 1.5-2.5% isoflurane with 2L/min O_2 . A catheter was inserted into the hind foot saphenous vein for intravenous administration of the hyperpolarized ^{13}C pyruvate during the MRI exam. Vital signs were monitored throughout the experiment, and body temperature was maintained at 37°C. To standardize metabolic state at the start of the experiment, all animals underwent MRI at roughly the same time of day. All animals were fasted for 2 hours before imaging and a subcutaneous injection of glycopyrrolate (0.01mg/Kg body weight) was administered half an hour before administration of anesthetic to reduce saliva production and risk of aspiration²¹⁴.

Anatomical T_1 -weighted gradient echo (repetition time/echo time [TR/TE] = 5.1/2.4 ms, flip angle = 15°, number of averages = 4, slice thickness = 0.9 mm, total scan time ~ 7 min) and T_2 -weighted spin echo (TR/TE = 2000/120 ms, number of averages = 2, slice thickness = 0.9 mm, total scan time ~ 7min) images with $0.875 \times 0.875 \text{ mm}^2$ in-plane resolution were obtained using a 32-element cardiac coil (In Vivo Corp., Gainesville, FL). Water-fat images were acquired using a modified IDEAL acquisition (TR/ Δ TE = 9.4/0.974 ms, echoes = 6, flip angle = 4°, number of averages = 4, slice thickness = 0.9 mm, total scan time ~ 13 min) with a $0.933 \times 0.933 \text{ mm}^2$ in-plane resolution and reconstructed into PDFF images. CSE-MRI (IDEAL-IQ) used parallel MRI to accelerate the acquisition by a factor of 1.75 in the phase and slice directions. Regions of interest were drawn around the whole liver, hind limb tissue, whole body, subcutaneous adipose tissue (SAT), and visceral adipose tissue (VAT) by L.S. (5 years' experience), who was blinded to the diet group. These segmentations were done manually with digitizing monitors using 3D Slicer (version 4.10.0)²¹⁵. For this study, the VAT was defined as the adipose tissue visible on IDEAL fat images below the diaphragm and above the pelvis

external to the abdominal cavity organs. SAT and VAT were reported as absolute values and as a percentage of the total body volume, calculated by dividing the adipose tissue volume by the whole body volume. These segmentations were used to measure the total volume and median PDFF of each region when overlaid on IDEAL fat fraction images. Areas of fat-water swaps were excluded from volumes that were used to measure PDFF.

Anatomical images were used as a reference to select a slab through the liver for 1D localized MRS. PRESS chemical shift MRS (TR/TE = 1082/35 ms, echoes = 1, slice thickness = 20.4 mm) was used to acquire hyperpolarized ^{13}C spectra over 90 s with a 1 s time resolution using a custom ^{13}C birdcage coil (Morris Instruments, Ottawa, Canada). [1- ^{13}C]pyruvate (Cambridge Isotope Labs, Massachusetts, USA) with 15mM Ox063 (Oxford Instruments, Oxford, UK) and 1.5mM Dotarem (Guebert, Villepinte, France) was hyperpolarized (Hypersense, Oxford Instruments), and a 3.5 mL bolus of the 80 mM solution (pH balanced, 37 °C) was injected over approximately 12 s into a vein in the hind leg²⁰⁶. Spectra were analyzed using SAGE software (Spectroscopy Analysis by General Electric, GE Medical Systems, Chicago, IL, USA), and the TTP was measured as the time between the pyruvate peak and metabolite peak to mitigate effects due to slight differences in injection times. TTP is a model-free analysis metric that roughly displays an inverse correlation with enzyme concentration²⁰¹. The animals were monitored, warmed, and kept on 100% O₂ until they began to wake up. They were then placed under a heating lamp and monitored until they were fully awake and mobile, at which time they were returned to their cages.

2.2.4 Ex Vivo Hepatic Determinations

2.2.4.1 Triglyceride Content

The left liver lobe was ground into a frozen powder over liquid nitrogen and analyzed for liver triglyceride levels using a colorimetric assay (Cayman Chemicals, Ann Arbor, MI, USA) following the manufacturer's instructions. Briefly, approximately 200 mg tissue was homogenized in NP-40 buffer containing leupeptin using an electric homogenizer. Samples were centrifuged at 10 000 g, and the supernatant was harvested. Samples from

CD-fed animals were not diluted, whereas samples from WD-fed animals were diluted 1:4 in NP-40 before assaying. After incubating the samples in the enzyme mixture for 15 minutes in the dark, the plate was read at 530 nm, 540 nm, and 550 nm. The absorbance at the three wavelengths was averaged and used to calculate triglyceride concentration based on the standard curve. Triglyceride concentration was normalized to protein concentration by Pierce BCA assay (ThermoFisher, Waltham, MA, USA).

2.2.4.2 Liver Cholesterol Content

Total lipids were extracted from approximately 150 mg of frozen liver tissue following the Folch method²¹⁶. Total cholesterol, free cholesterol, and cholesteryl ester levels in lipid extracts were determined by enzymatic, colorimetric assays (Wako Diagnostics, Richmond, VA, USA) (20) performed through the Metabolic Phenotyping Laboratory in Robarts Research Institute (London, Ontario, Canada). Cholesterol levels were normalized to the mass of the extracted tissue.

2.2.4.3 Western Blot

Protein was isolated from approximately 100 mg of frozen, ground liver tissue using RIPA buffer containing Aprotinin, Leupeptin, PMSF, NaF, and Sodium Orthovanadate (New England BioLabs, Ipswich, MA, USA). Tissue was homogenized using an electric homogenizer, sonicated at 30% amplitude for 5 second processing time, and centrifuged at 12 000 g for 30 mins at 4°C. The supernatant was harvested and stored at -80°C until use. Protein samples were prepared in laemmli buffer containing b-mercaptoethanol at a final concentration of 5%. Twenty mg of protein was run through 10% polyacrylamide tris-glycine gels and transferred onto PVDF membrane. Membranes were probed for PDH, phosphorylated PDH (pPDH), and LDH (Table 1) overnight at 4°C. Anti-rabbit secondary antibodies (Table 1), conjugated to HRP, were used to detect primary antibodies by incubating for one hour at room temperature. Proteins were detected using Amersham ECL reagent (GE Healthcare, Chicago, IL, USA) and ChemiDoc imager (BioRad, Hercules, CA, USA) with ImageLab software. Protein expression was normalized to total protein by amido black staining.

Table 2.1: Antibodies used in Western blot analysis

Antibody	Host Animal	Company	Catalog #	Dilution
Pyruvate Dehydrogenase	Rabbit mAb	Cell Signaling	3205	1:1000 in 5% BSA
Phosphorylated Pyruvate Dehydrogenase-E1 α (pSer ²³²)	Rabbit pAb	EMD Millipore	AP1063	2:2000 in 5% milk
Lactate Dehydrogenase	Rabbit pAb	Cell Signaling	2012	1:1000 in 5% BSA

2.2.4.4 Enzyme Activity Assays

Six samples were randomly selected from each diet group for enzyme activity assays. Liver tissue was homogenized in 9 volumes of homogenization buffer (25 mM HEPES, 2 mM EDTA, 0.1% (v/v) Triton X-100, 10 mM sodium fluoride, 1 mM sodium orthovanadate, pH 7.8) using a microtube plastic pestle. Following incubation at 4°C for 20 min, homogenates were centrifuged at 10000 g for 10 min at 4 °C. Floating lipid was removed by aspiration, and pellets were resuspended within the supernatant for each sample. Samples were subjected to three rounds of freeze-thaw in liquid nitrogen, then assayed immediately for enzyme activity. Enzyme assays were performed at 37°C using a Spectramax plate spectrophotometer (Molecular Devices, Sunnyvale, CA, USA) in a 96-well plate. Enzyme activities were expressed relative to total protein concentration for each homogenate (determined by bicinchoninic acid (BCA) assay).

Lactate dehydrogenase (LDH) activity was measured following the addition of 5ml liver homogenate (diluted 1:20 in homogenization buffer) to 295ml assay mixture containing 50 mM HEPES (pH 7.4), 0.2 mM NADH, 1.0 mM pyruvate. Absorbance values (340 nm) were collected for 3-5 mins, and LDH activity was calculated using an extinction coefficient of 6.22 L mol⁻¹ cm⁻¹.

Pyruvate dehydrogenase (PDH) activity was measured following the reduction of iodonitrotetrazolium chloride (INT) at 500 nm. Background rates were collected following the addition of 5 ml liver homogenate to 290 ml assay mixture containing 50

mM Tris (pH 7.8), 0.5 mM EDTA, 2.5 mM NAD⁺, 0.2 mM Coenzyme A, 0.1 mM sodium oxalate, 0.4 mM thiamine pyrophosphate, 1 mg/ml bovine serum albumin, 0.1% (v/v) Triton X-100, and 1U/ml diaphorase. The PDH reaction was then initiated by the addition of 5 ml 0.6 M sodium pyruvate. PDH activity was calculated from the difference between the rates with and without pyruvate, using an extinction coefficient of 15.4 L mol⁻¹ cm⁻¹.

Citrate synthase (CS) activity was measured following the addition of 10 ml liver homogenate (diluted 1:20 in homogenization buffer) to 287 ml assay mixture containing 50 mM Tris (pH 8.0), 0.1 mM 5,5-dithiobis(2-nitro-benzoic acid) DTNB), and 1.15 mM acetyl CoA. Parallel reactions were run with and without the addition of 0.5 mM oxaloacetate. Absorbance values (412 nm) were collected for 5 min, with CS activity calculated from the difference between the rates with and without oxaloacetate, using an extinction coefficient of 13.6 L mol⁻¹ cm⁻¹.

2.2.5 Statistical Analysis

Unpaired two-tailed Student's t-tests were used to determine differences in all measurements between animals in the two diet groups. A Shapiro-Wilk normality test was used to confirm the normal distribution of the data, and subsequently, the Pearson correlation coefficient was calculated for correlations between MRI and *ex vivo* data using a two-tailed P-value and a 95% confidence interval. Results are shown as mean ± SEM, and statistical significance was set at $p < 0.05$. Data analysis was performed using GraphPad Prism 6 (San Diego, CA, USA).

2.3 Results

2.3.1 Animal Body Weights and Food Intake

Average daily food consumption and daily calorie consumption did not significantly differ between the diet groups in the 10 days before MRI (CD 45.27 ± 2.64 g/day/kg body weight vs WD 45.56 ± 4.67 g/day/kg body weight, $p = 0.958$; CD 121.1 ± 9.48 kcal/day vs WD 130.6 ± 25.87 kcal/day, $p = 0.578$) or during the time between MRI and

euthanasia (CD 51.11 ± 2.84 g/day/kg body weight vs WD 54.43 ± 7.58 g/day/kg body weight, $p = 0.667$; CD 132.1 ± 11.42 kcal/day vs WD 150.0 ± 33.54 kcal/day, $p = 0.416$). On average, guinea pigs in the WD group weighed significantly less than animals in the CD group based on weight recording in the 10 days before (CD 770.6 ± 17.97 g vs WD 693.6 ± 18.52 g, $p < 0.05$) and the period after the MRI examination (CD 774.6 ± 21.63 g vs WD 708.3 ± 19.01 g, $p < 0.05$).

2.3.2 Blood Profiles Show Elevated Indicators of Liver Damage in Western Diet Animals

ALT levels were significantly elevated in WD-fed animals compared to CD-fed animals ($p < 0.05$, Table 2). Blood cholesterol levels were also significantly greater in WD-fed animals compared to CD-fed animals ($p < 0.05$, Table 2). No significant differences were observed in levels of ALP ($p = 0.1301$), GGT ($p = 0.7814$), BA ($p = 0.5457$), TBIL ($p = 0.2914$), or BUN ($p = 0.7276$) between the two diet groups, though there was a non-significant trend towards elevated ALB in WD-fed animals ($p = 0.0508$, 95% CI = [-0.001085, 0.5189]; Table 2).

Table 2.2: Liver function and tissue profiles

Liver Function Profile	CD	WD	P-value
Alkaline phosphate (ALP) [u/L]	62.43 ± 11.06	43.14 ± 5.65	0.1301
Alanine aminotranferase (ALT) [u/L]	48.14 ± 2.80	82.00 ± 9.58	0.0071
Gamma glutamyl-transferase (GGT) [u/L]	6.14 ± 0.74	6.63 ± 1.53	0.7814
Blood ammonia (BA) [μ mol/L]	52.57 ± 13.65	65.38 ± 15.14	0.5457
Bilirubin (TBIL) [mg/dl]	0.20 ± 0	0.24 ± 0.02	0.2914
Albumin (ALB) [g/dl]	4.03 ± 0.08	4.29 ± 0.09	0.0508
Blood urea nitrogen (BUN) [mg/dl]	22.75 ± 1.87	23.50 ± 0.98	0.7276
Cholesterol (CHOL) [mg/dl]	71.57 ± 14.37	440.4 ± 29.84	< 0.0001
Liver Tissue Component	CD	WD	P-value
Triglycerides (TG) [mg/mg protein]	0.02 ± 0.00	0.11 ± 0.01	< 0.0001
Total cholesterol [mg/mg tissue]	2.44 ± 0.12	19.34 ± 1.91	< 0.0001

Free cholesterol [mg/mg tissue]	1.85 ± 0.11	4.72 ± 0.28	< 0.0001
Cholesterol ester [mg/mg tissue]	0.59 ± 0.07	14.62 ± 1.66	< 0.0001

2.3.3 Impact of Lifelong Western Diet on Body and Organ Fat Content

Using MRI, at 144 ± 4 days PN, WD-fed animals had a significantly lower body volume compared to CD-fed animals (CD $684800 \pm 20000 \text{ mm}^3$ vs WD $631200 \pm 16100 \text{ mm}^3$, $p < 0.05$; Figure 2.1A). Additionally, following lifelong WD feeding, guinea pigs had significantly elevated liver volume (CD $28300 \pm 1000 \text{ mm}^3$ vs WD $41400 \pm 3200 \text{ mm}^3$, $p < 0.05$; Figure 2.1B) compared to CD-fed animals, with no significant differences in hind limb volume ($p = 0.6667$, Figure 2.1C) between the two groups. WD-fed animals showed a significantly elevated liver PDFF (CD $6.20 \pm 0.34 \%$ vs WD $10.64 \pm 0.87 \%$, $p < 0.05$; Figure 2.1D) and significantly decreased hind limb PDFF (CD $5.47 \pm 0.58 \%$ vs WD $3.86 \pm 0.25 \%$, $p < 0.05$; Figure 2.1E) compared to CD-fed animals. The SAT (CD $34897 \pm 2339 \text{ mm}^3$ vs WD $28196 \pm 2173 \text{ mm}^3$, $p < 0.05$) and VAT (CD $29374 \pm 2316 \text{ mm}^3$ vs WD $22299 \pm 2075 \text{ mm}^3$, $p < 0.05$) volumes were significantly larger in CD-fed animals compared to WD-fed animals. When considering the SAT and VAT as a percentage of total body volume, there were no differences between animals in the two diet groups (Figure 2.2A, B); however, there was a reduction in total adipose tissue (VAT + SAT) as

a percentage of total body volume in WD-fed animals vs CD-fed animals (CD 9.32 ± 0.43 % vs WD 8.01 ± 0.44 %, $p < 0.05$; Figure 2.2C).

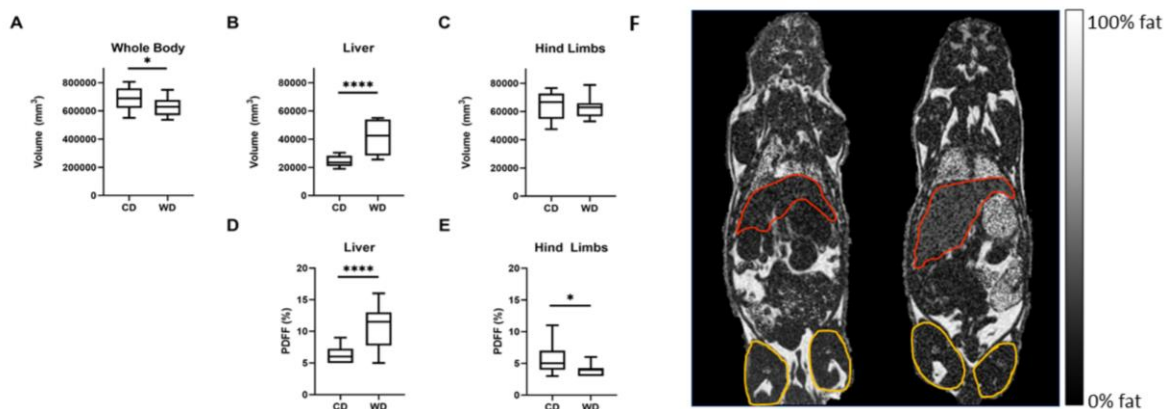


Figure 2.1: Total volumes estimated from MRI for the whole body (A), liver (B), and hind limbs (C). WD-fed animals displayed a significantly decreased whole-body volume and increased liver volume compared to the CD-fed animals. Median PDFF percentages of the liver (D) and hind limbs (E) show a significantly elevated PDFF in the livers and lower PDFF in the hind limbs of WD-fed animals compared to CD. * indicates $p < 0.05$, ** indicates $p < 0.0001$. (F) Examples of proton-density fat fraction image slices from an animal in the CD (left) and WD (right) groups. The livers and hind limbs are outlined in red and yellow, respectively, in both images. The PDFF is visibly elevated in the WD-exposed liver, as indicated by a lighter colour, and visibly reduced in the WD hind limb. In the box-and-whisker plots, the boxes extend from the 25th to 75th percentiles, the middle line is the median, and the whiskers extend from the smallest to the largest value in the data set.**

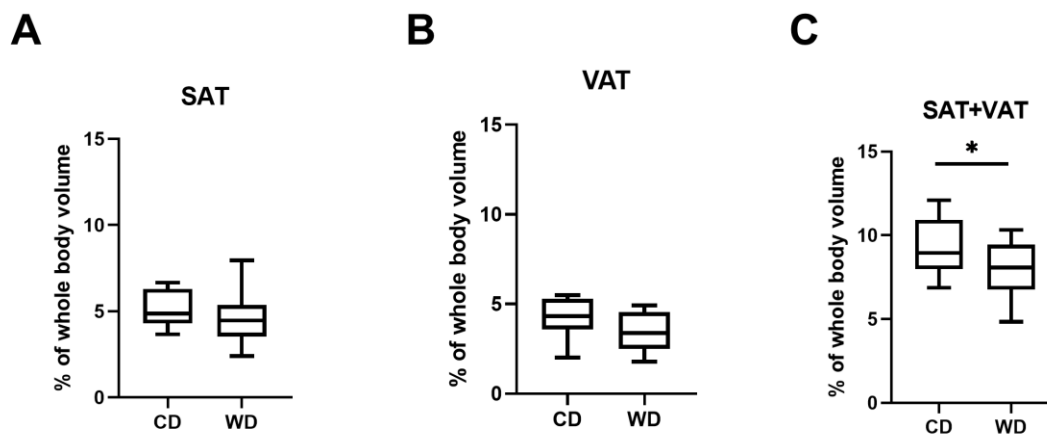


Figure 2.2: Adipose tissue volumes as a percentage of total body volume for the subcutaneous adipose tissue (A), visceral adipose tissue (B), and the sum of subcutaneous and visceral adipose tissue (C). The SAT+VAT as a percentage of total body volume was significantly elevated in CD-fed animals. * indicates $p < 0.05$.

2.3.4 Western Diet Feeding Results in Accelerated Hepatic Lactate Production Rate

Of the 28 animals scanned in MRS experiments, 26 spectra produced viable data (CD $n = 13$, WD $n = 13$; Figure 2.3A). Lactate TTP in WD-fed animals was significantly lower than in CD-fed animals (CD 14.92 ± 1.14 sec vs WD 11.15 ± 1.06 sec, $p < 0.05$; Figure 2.3B). The TTP related to the rate of metabolism for pyruvate to alanine did not significantly differ with respect to diet conditions ($p = 0.2422$, Figure 2.3C).

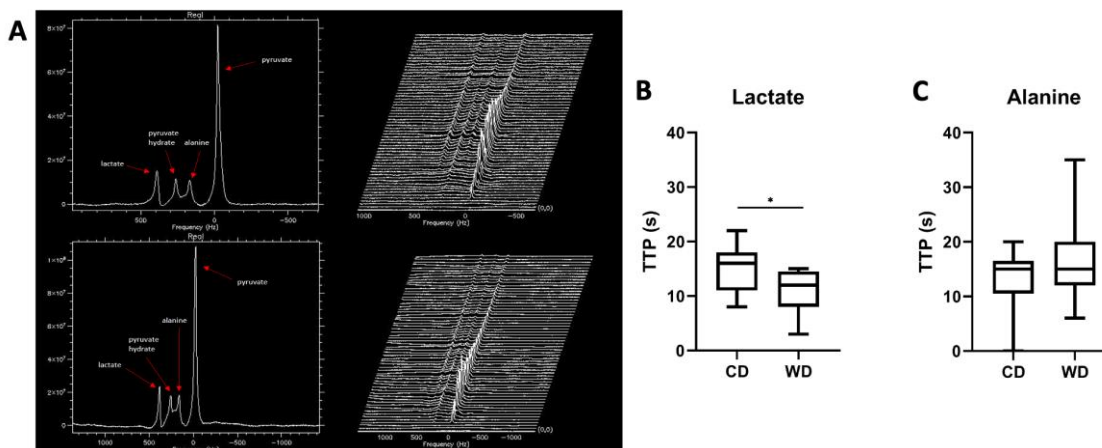


Figure 2.3: (A) Examples of hyperpolarized [1-¹³C]pyruvate magnetic resonance spectra (left) and stack plots (right) from one CD (top) and one WD (bottom) fed guinea pig liver. Frequency is relative to the center of the pyruvate peak. Stack plots display spectra from the first 60 seconds of acquisition with a 1 second time resolution. Mean time to peak (TTP) measured from the time of the pyruvate peak for lactate (B) and alanine (C) in both diet groups. WD (n = 13) animals show a significant decrease in lactate TTP compared to CD (n = 13) animals.* indicates p < 0.05.

2.3.5 Lifelong Western Diet Alters Body and Liver Weights

At 150 ± 6 days PN, tissue collection samples showed WD-fed guinea pigs were significantly lighter than CD-fed guinea pigs (CD 787.6 ± 21 g, n = 14 vs WD 718.8 ± 17.9 g, n = 14; p < 0.05), despite WD-exposed livers being significantly heavier than CD-exposed livers both in absolute weight (CD 26.70 ± 1.18 g vs WD 42.33 ± 2.47 g; p < 0.05) and as a fraction of total body weight (CD 0.034 ± 0.001 vs WD 0.059 ± 0.003 ; p < 0.05). Kidneys from WD-fed animals were found to be lighter than those from CD-fed animals as an absolute weight (CD 5.45 ± 0.16 g vs WD 5.00 ± 0.12 ; p < 0.05) but no differences were found in kidney weight as a fraction of total body weight (CD 0.0070 ± 0.0002 vs WD 0.0070 ± 0.0002 ; p = 0.883). Brain and heart weights were not significantly different between the two diet groups in absolute weight (CD 3.96 ± 0.31 g vs WD 3.91 ± 0.24 g, p = 0.55; CD 3.28 ± 0.56 g vs WD 2.84 ± 0.58 g, p = 0.15) or as a fraction of total body weight (CD 0.0055 ± 0.0001 vs WD 0.0051 ± 0.0002 , p = 0.072, 95% CI = $[-3.812 \times 10^{-5}, 8.296 \times 10^{-4}]$; CD 0.0042 ± 0.0005 vs WD 0.0039 ± 0.0005 , p = 0.323).

2.3.6 Triglyceride and Cholesterol Levels are Elevated in WD-exposed Livers

WD-fed animals had significantly elevated hepatic TGs compared to CD-fed animals ($p < 0.05$, Table 2). The hepatic triglyceride concentration displayed a moderate correlation to the PDFF in the livers of animals in both diet groups combined ($r = 0.692$, Figure 2.4). The correlation between TG and PDFF becomes weak and non-significant when only considering animals from the WD group ($r = 0.311$, $p = 0.301$, $n = 14$). Total cholesterol ($p < 0.05$; Table 2), free cholesterol ($p < 0.05$; Table 2), and cholesteryl ester ($p < 0.05$; Table 2) were significantly increased in the WD-exposed liver tissues.

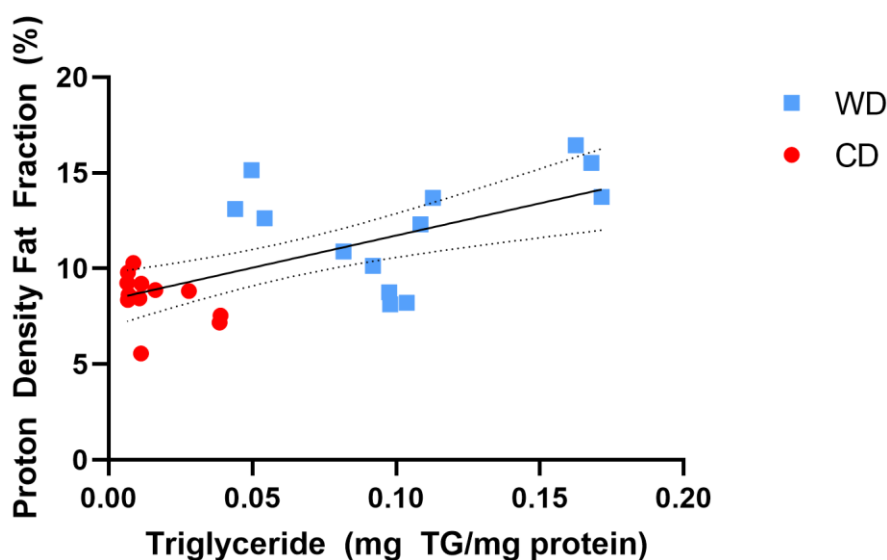


Figure 2.4: Liver triglyceride concentrations plotted against PDFF in the liver. There is a moderate positive correlation ($r = 0.6917$, $p = 0.0001$) between TG and PDFF for all animals. The linear fit line is shown with 95% confidence intervals. There is a non-significant weak correlation between TG and PDFF when only considering animals from the WD group ($r = 0.311$, $p = 0.301$).

2.3.7 Altered PDH and LDH Activity in WD-exposed Livers

PDH protein levels were significantly increased in WD-fed animals compared to CD-fed animals (CD 0.28 ± 0.02 , $n = 13$ vs WD 0.42 ± 0.04 , $n = 14$; $p < 0.05$, Figure 2.5A), with no difference observed in phosphorylated PDH ($p = 0.5694$, Figure 2.5B), although PDH activity was significantly decreased in WD-fed animals (CD 1.56 ± 0.14 $\mu\text{mol}/\text{min} \cdot \text{mg}$

protein, $n = 6$ vs WD $0.50 \pm 0.24 \mu\text{mol}/\text{min} \cdot \text{mg}$ protein, $n = 5$; $p < 0.05$, Figure 2.5D). Note that one of the samples from an animal in the CD group was not abundant enough to be used for protein level analysis and thus was not included in this data. Despite no difference in protein levels of LDH ($p = 0.1477$, Figure 2.5C), LDH activity was significantly elevated in WD-exposed livers (CD $388.7 \pm 35.3 \mu\text{mol}/\text{min} \cdot \text{mg}$ protein, $n = 6$ vs WD $638.6 \pm 73.1 \mu\text{mol}/\text{min} \cdot \text{mg}$ protein, $n = 6$; $p < 0.05$, Figure 2.5E). No significant difference with respect to diet was observed in CS activity ($p = 0.1031$, Figure 2.5F).

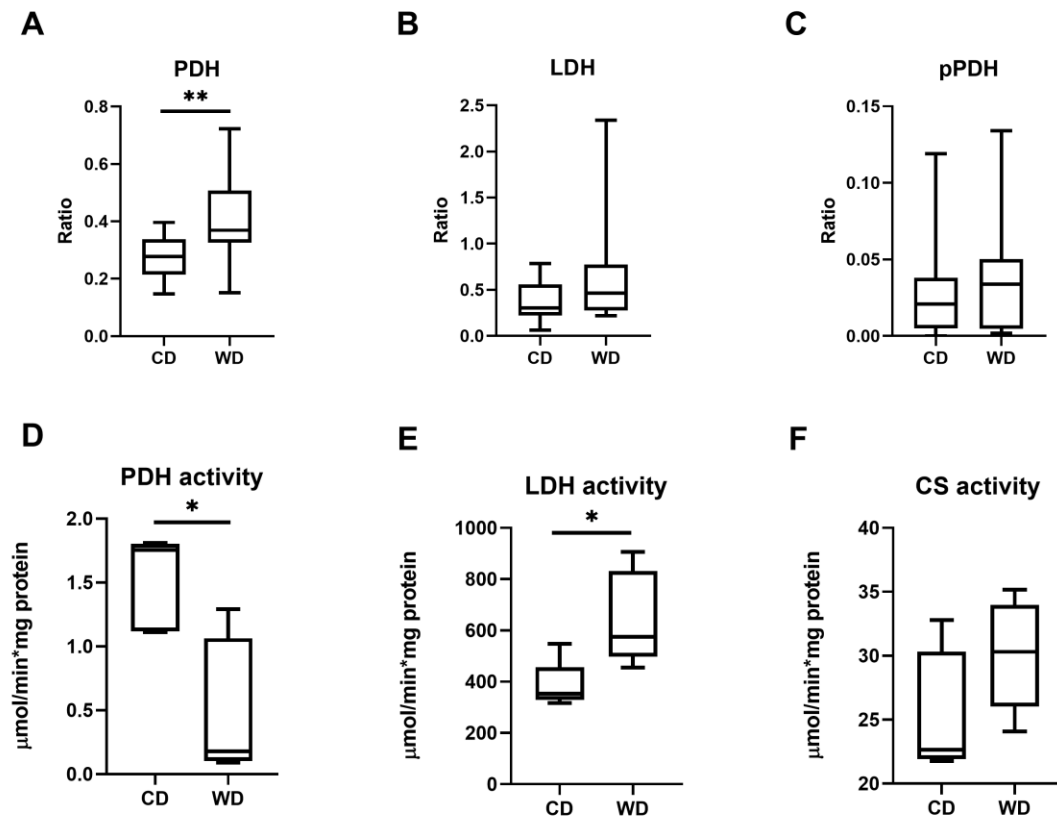


Figure 2.5: Liver enzyme protein levels for pyruvate dehydrogenase (PDH; A), lactate dehydrogenase (LDH; B), and phosphorylated PDH (pPDH; C). Enzyme activity measured from liver tissue for PDH (D), LDH (E), and citrate synthase (CS; F). * indicates $p < 0.05$, ** indicates $p < 0.01$.

2.3.8 Correlations

All data passed the Shapiro-Wilk normality test. LDH activity displayed a significantly strong positive correlation with PDFFF in the liver ($r = 0.829$, $p < 0.05$; Figure 2.6A) and PDH activity displayed a significantly strong negative correlation with liver PDFFF using data from both diet groups ($r = -0.835$, $p < 0.05$; Figure 2.6B). LDH activity was also shown to have a moderate negative correlation with the lactate TTP measurement across all animals in both diet groups ($r = -0.600$, $p = 0.051$; Figure 2.6C).

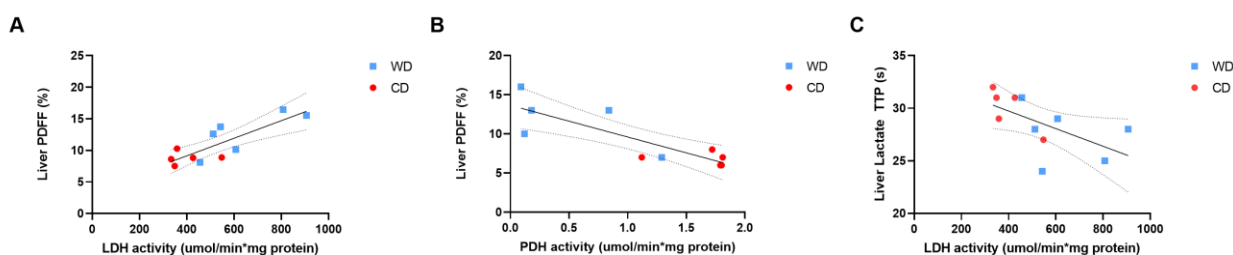


Figure 2.6: (A) Liver PDFFF plotted against LDH activity displays a strong positive correlation ($r = 0.8289$, $p = 0.0016$). (B) Liver PDFFF plotted against PDH activity displays a very strong negative correlation ($r = -0.8350$, $p = 0.0026$). (C) LDH enzyme activity plotted against lactate TTP displays a moderate negative correlation ($r = -0.6004$, $p = 0.0508$). Linear fit lines are shown with 95% confidence intervals .

2.4 Discussion

2.4.1 PDFFF Findings Consistent with Lean NAFLD Phenotype

The increase in liver PDFFF with a decline in hind limb PDFFF is evidence that this model of lifelong WD consumption promotes NAFLD; differential fat deposition occurs, displaying a lean NAFLD phenotype. High-fat and high-fat/high-sugar diets have typically been found to induce obesity in animal models²¹⁸, although lean phenotypes of NAFLD are also reported²¹¹. PDFFF values of guinea pig⁸ and rat²¹⁹ livers previously reported in the literature are similar to PDFFFs reported in this study for both WD and CD groups. Also of note, the liver PDFFF values observed in WD-fed animals were within the range of PDFFF values (10-20%) previously reported in human patients with grade 1 and 2 steatosis¹⁵¹. This pre-clinical assessment of lean NAFLD using PDFFF MRI techniques

similar to those that have been established in human studies²⁰⁹ provides motivation for further research focused on lean NAFLD in humans, which is often overlooked clinically and in the literature²²⁰. The increased volume and weight of livers in WD-fed animals reflect fat accumulation in the liver and are likely indications of enlarged hepatocytes²²¹. WD-fed animals had significantly elevated hepatic TG and cholesterol levels, with all liver TG concentrations being above the lower limit for hepatic steatosis defined in humans²²². Elevated liver TG and cholesterol levels found in WD-fed animals indicate that lifelong exposure to the WD may result in lipid overload and dysfunction in the liver²²³. Related to this, elevated serum ALT was observed in WD-fed animals, indicating liver damage²²⁴. ALT is a reliable marker of hepatocellular injury or necrosis, suggesting that the WD group experienced liver cell damage due to diet²²⁴. Although not statistically significant, a trend towards elevated serum ALB in WD-fed animals was observed and is another indication of liver damage²²⁵.

Animals in the WD group exhibited a smaller body volume, weight, and proportion of adipose tissue compared to animals in the CD group. Specifically, the decreased percentage of adipose tissue may be explained by the WD's high fructose content, as fructose has been shown to decrease lipogenesis in rat adipose tissue²²⁶. The overload of dietary fructose in rats has also been found to increase the release of free fatty acids from adipose tissue into the bloodstream, where the fatty acids may eventually be taken up by hepatocytes and stored as TGs in the liver²²⁷. The loss of muscle mass has been reported in chronic liver diseases such as NAFLD²²⁸, and it is speculated that this may also explain the overall decreased body weight and volume of WD-fed animals in this study. While other studies have found acute high fructose diets to increase visceral adiposity^{13,228}, it is speculated here that the lifelong exposure to a high fructose diet during critical development stages in this study results in a reduced capacity of extrahepatic adipose tissues to synthesize and store fatty acids. Hexokinase, a hepatic enzyme responsible for fructose metabolism in adipose tissue, is adaptive to diet and may be responsible for the reduction of adipose tissue as a response to high fructose exposure²²⁶. Similar changes of reduced body size and adiposity have been noted after exposure to high fructose diets in neonates²²⁹ and *in utero*²³⁰, suggesting that adaptations to an overload of dietary fructose may be programmed at a very young age or even before birth. Previous studies in guinea

pigs have reported a lean phenotype with decreased adipose tissue after lifelong WD exposure with the same diet composition as the WD used in this study⁸. The mechanisms of this adaptation to a high fructose diet in the adipose tissue during early development is an important topic that warrants further research.

2.4.2 Altered Pyruvate Metabolism and Evidence of Damaged Livers Found in WD-fed Animals

The decreased *in vivo* lactate TTP, indicating an increased rate of lactate production, and the increased *ex vivo* LDH activity in the WD group highlight, in two techniques, a shift towards lactate production via anaerobic glycolysis in the fatty livers²⁰⁵. In the current study, PDFF in the liver showed a strong correlation to LDH enzyme activity, supporting the relationship between fatty livers and the promotion of anaerobic glycolysis. Increased lactate concentration may be linked to a disturbance in liver lipid synthesis²¹¹ and has been found in obese mice, indicating that lactate may act as a metabolic biomarker for a diet-induced fatty liver²³¹. WD-fed animals showed a significant increase in PDH protein levels but a significant decrease in PDH activity, suggesting inhibition of PDH in the livers of WD-fed animals. Reports of decreased PDH activity in liver disease are associated with increased lactate as PDH normally regulates lactate production in healthy livers²³². A previously published study by Lee et al. used a rat model to investigate the effects of a lifelong exposure to a high-fat diet and found no change in lactate production, but rather an increase in aspartate and malate production in the livers of these animals²¹⁰. The diet used in their study was not high in sugar, unlike the diet used in the current study, and these diet differences may explain the disparity in lactate production findings in the liver. Another relevant study used a rat model with induced obesity to investigate the effects of an acute exposure to a high-fat diet²⁰⁵. This study observed increased lactate in the liver after six weeks of exposure to the high-fat diet, in conjunction with NAFLD, which would be consistent with our findings of increased lactate as a result of NAFLD²⁰⁵. A major difference in the acute study was the finding of increased alanine production in the liver, which was not observed in the chronic WD-induced NAFLD model presented here. It may be hypothesized that the mechanisms resulting in increased liver alanine may be associated with the onset of NAFLD and become more subtle over time in a chronic

model of NAFLD like the one presented in this study. In support of this hypothesis, a previous study has found no evidence of elevated ALT in NAFLD patients with portal chronic inflammation, which is a marker of advanced disease state²³³. Considering data from these multiple studies allows us to investigate liver function differences between acute and chronic exposure to high-fat diets. Demonstrating the sensitivity of HP [1-¹³C]pyruvate MRS in measuring liver metabolism in different species and experimental conditions is an essential step in its external validation for use as an *in vivo* biomarker of liver dysfunction. This technology is already being implemented in clinical studies to measure pyruvate metabolism in tumours, and studies providing motivation for its use in NAFLD patients may help to accelerate its clinical translation for this application¹⁸⁸.

An approach to consider for future work may include a longitudinal study that repeats these imaging experiments in both sexes, at different time points in the guinea pigs' development to understand the impact of sex upon these changes and also when liver metabolic changes occur in the animal's lifespan. Additionally, these imaging methods could be implemented in a study investigating whether diet reversal, exercise, or therapeutic interventions can modulate the metabolic effects of the WD. Previous studies have demonstrated the benefits of dietary intervention and exercise in decreasing liver volume and fat accumulation but have not specifically looked at the impact of these interventions on hepatic pyruvate metabolism *in vivo*²³⁴.

2.4.3 Limitations

First, due to the low signal-to-noise ratio of bicarbonate in MRS experiments, there was insufficient data to measure the bicarbonate TTP. Information on the rate of bicarbonate production *in vivo* would have been valuable to correlate to PDH activity and further confirm the value of hyperpolarized ¹³C MRS as a tool to measure hepatic [1-¹³C]pyruvate labelled metabolism. Second, labelling the first carbon on the pyruvate molecule limits which downstream metabolites can be measured via MRS. Other experiments may label the second carbon on pyruvate instead to measure the signal from metabolites involved in the metabolic pathway following pyruvate's conversion into acetyl-CoA. Third, our TTP measurement precision is limited by the 1 s temporal

resolution of our MRS experiments. Finally, the animals' metabolic environment may be affected by the anesthetic during MRI experiments, limiting our ability to observe homeostasis *in vivo*²³⁵. To combat this, the animals were returned to their cages to recover in the days between the MRI examination and tissue collection.

2.4.4 Conclusion

PDFP imaging showed increased fat fractions, corresponding to increased TG levels in the livers of male guinea pigs fed a lifelong WD. Further, the application of hyperpolarized ¹³C MRS demonstrated utility in probing metabolic events in the liver that correlated with *ex vivo* liver enzyme activities. Hyperpolarized ¹³C spectroscopy results, in conjunction with altered LDH enzyme activity, highlight a shift from oxidative metabolism of pyruvate to anaerobic glycolysis and increased lactate production in the fatty livers of animals fed a WD. These results highlight lactate production as an indication of changes brought on by NAFLD development after chronic exposure to a WD in a guinea pig model of lean NAFLD. Hyperpolarized MRS techniques provide a non-invasive method of examining liver metabolism that correlates well with *ex vivo* findings and may eventually be used to help diagnose and determine the efficacy of treatment for NAFLD.

Chapter 3

3 Optimizing Signal-to-noise Ratio for Multi-metabolite Hyperpolarized Carbon-13 Magnetic Resonance Imaging using a Hybrid Flip Angle Scheme

3.1 Introduction

The placenta produces a variety of biomolecules during pregnancy that are important for both maternal and fetal metabolism²³⁶. *In vivo* assessment of placental metabolism would allow us to characterize healthy metabolism at all stages of pregnancy and investigate potential placental metabolic abnormalities in conditions such as intra-uterine growth restriction²³⁷. Imaging assessment of the placenta during pregnancy is generally limited to the non-ionizing imaging modalities of ultrasound and MRI. These imaging techniques can contribute structural information and limited functional data about the placenta^{237,238}.

Hyperpolarized carbon-13 magnetic resonance imaging (HP ¹³C MRI) is an ideal imaging modality for real-time *in vivo* monitoring of metabolism. Using d-DNP methods, it is possible to temporarily increase signal up to 10,000 fold and acquire images of the distribution of molecules enriched with the hyperpolarized substrate²³⁹. This technique has a variety of applications in research, including tumour monitoring, inflammation, cardiac disease, and fetoplacental development^{177,206}.

One of the more common HP ¹³C MRI substrates is [1-¹³C]pyruvate, which following an intravenous injection allows us to resolve signal from its metabolites: lactate, alanine, and bicarbonate. Pyruvate metabolism is a key step in glycolysis and indicative of normal and abnormal cell function. The metabolic by-products of pyruvate follow different metabolic pathways, some aerobic and some anaerobic, and the metabolic fates of these biomolecules provide insight into the biological state of the region or organ of interest. The metabolic conversion rate constant from pyruvate to a metabolite (e.g. K_{PL} is the conversion rate of pyruvate \rightarrow lactate) can be calculated from the time-resolved

measurements of the different metabolites and provides a quantitative measure of metabolism related to enzyme concentrations *in vivo*²⁴⁰. Measuring the entire concentration-time curve of each metabolite is necessary for a robust sampling of data in order to calculate metabolic rates. As such, a sufficiently high signal-to-noise ratio (SNR) must be maintained throughout the entire acquisition.

The metabolites of pyruvate we wish to image exist at distinct chemical shifts (between -9.7 to 12.6 ppm relative to pyruvate). Since metabolism of the injected pyruvate occurs rapidly, the relative abundance of each metabolite changes over the course of the experiment. The metabolites are typically found in quantities > 6-fold lower than pyruvate. In past experiments we have taken advantage of this by utilizing a spectrally varying RF pulse such that pyruvate is exposed to a smaller flip angle than its metabolites that are lower in abundance²⁰⁶. This flip angle scheme is spectrally varying but constant in time and will be referred to as the constant flip angle (CFA) scheme.

The rapid T_1 decay of the hyperpolarized state provides challenges to maximizing SNR. Previous HP ^{13}C MRI studies²⁴¹⁻²⁴⁶ have addressed this by proposing variable flip angle (VFA) schemes that increase the flip angle over time for one metabolite. These studies typically use a spectral-spatial RF pulse shape and vary the pulse amplitude at each excitation, continuously increasing to 90° to maintain a constant signal from a single spectral peak of a hyperpolarized ^{13}C molecule despite the rapid decay of polarization.

The aim is to expand upon the CFA scheme to optimize SNR in HP ^{13}C MRI experiments by introducing a novel approach that allows us to deliver optimized time-varying flip angles to each metabolite by taking advantage of the spectral variance of CFA. This will be referred to as the multi-spectral variable flip angle (msVFA) scheme. The individual trajectories for each metabolite using msVFA are calculated using previously published VFA methods and applied to each metabolite simultaneously by progressively varying both the shape and amplitude of the spectrally varying pulse. This allows us to produce a distinct VFA trajectory for each metabolite and apply the SNR benefits associated with VFA to all metabolites simultaneously²⁴⁷.

In this study, the novel msVFA is compared to the CFA scheme. The comparison CFA to msVFA was chosen as it allows for comparison of the SNR for all four metabolites of interest simultaneously. Additionally, this comparison highlights an alternative to the spectral-spatial RF method as an improvement of the current IDEAL technique.

Therefore, the focus of this work is to investigate the benefit of adding time-varying flip angles to the CFA method to provide optimal SNR for multiple metabolites simultaneously.

It is hypothesized that the msVFA scheme will provide SNR equivalent to VFA for each metabolite; therefore, it will significantly increase SNR throughout the experiment for each metabolite compared to the CFA scheme. If successful, the msVFA has potential to improve HP ^{13}C MRI image quality in a variety of research applications including, but not limited to, fetoplacental research.

3.2 Methods

3.2.1 Simulations

Flip angles for each metabolite were calculated using the method described by Xing et al.²⁴⁵, which takes into account both the T_1 decay and metabolic conversion of each metabolite. This method was used to calculate the flip angles that would optimize SNR for each metabolite throughout the experiment. The calculated flip angles for the msVFA scheme were compared to a CFA scheme previously described by Friesen-Waldner et al.²⁰⁶. Figure 3.1 shows the flip angle trajectories applied in this work for both of these methods.

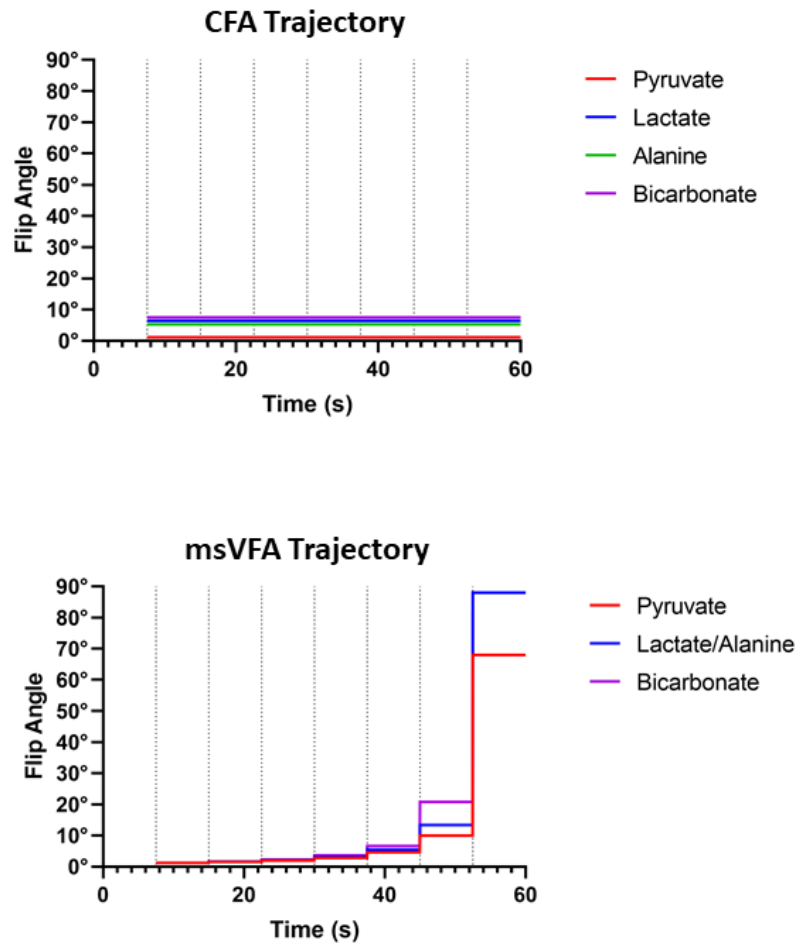


Figure 3.1: The desired flip angle trajectories for each metabolite are shown for CFA (top) and msVFA (bottom) strategies. These flip angles were achieved using a double Gaussian RF pulse. Dotted vertical lines indicate the start time of each acquisition.

Bloch equations were used to simulate the SNR of different metabolites using Matlab (MATLAB 2018a, Mathworks, 2018). Equation 3-1 was used to estimate SNR at each n^{th} time point for every metabolite (met) where the concentration of each metabolite was calculated using estimated T_1 decay and metabolic conversion rates found in the literature^{248,249}. The predicted SNR resulting from using the implemented flip angle in msVFA was compared to the predicted SNR using the exact VFA for each metabolite.

$$SNR_{met}(n) = [Met(n)]e^{-\frac{(n-1)TR}{T_{1met}}} (\sin \alpha) \cos \alpha^n \quad 3-1$$

3.2.2 msVFA Implementation and Verification

In the msVFA experiments, a unique RF waveform is applied for each image acquisition²⁴⁷. Additional improvement would likely be possible by applying a unique RF waveform for each excitation of each image. This may be feasible for single-shot pulse-and-acquire type sequences but becomes impractical to implement for the thousands of custom RF pulse shapes required for the sequence used here.

The double Gaussian pulse allows us to implement unique flip angles for each metabolite; however, the double Gaussian pulse shape limits our accuracy in delivering the exact calculated flip angles to every metabolite. If there was interest in imaging only two or three metabolites, the double Gaussian pulse could be used to deliver the exact calculated flip angles; however, with four metabolites, some approximations must be made due to the different spectral positions. This is why lactate and alanine are delivered the same flip angle in msVFA experiments.

For ¹³C acquisitions, a quadrature volume transmit and receive coil was used (12 cm diameter, 19 cm long)¹⁵⁵. The desired flip angles were applied to each metabolite using double Gaussian RF spectral profiles designed for each acquisition. The RF profiles for each acquisition are shown in Figure 3.2.

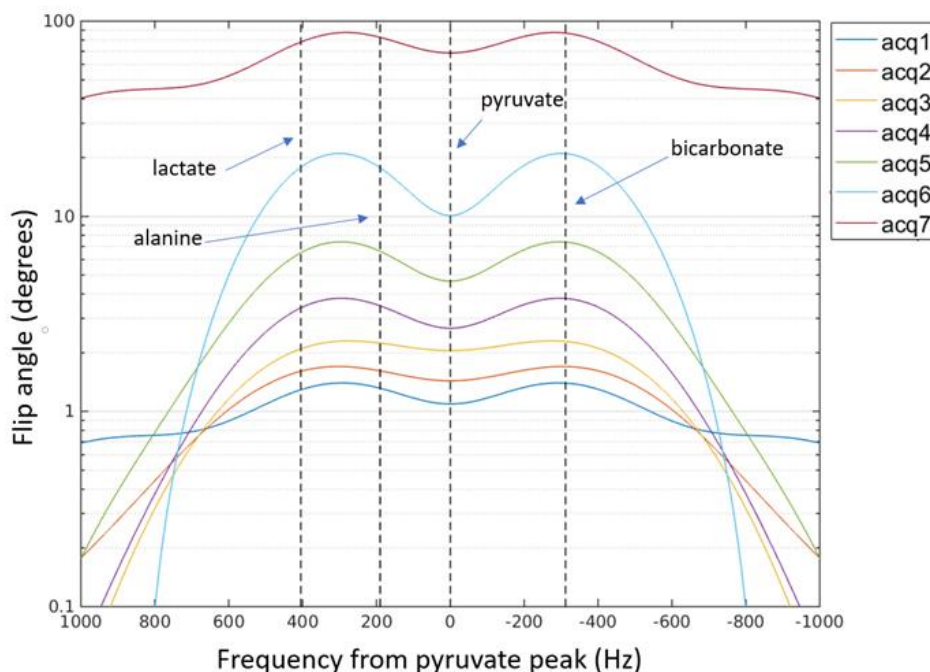


Figure 3.2: The double Gaussian RF spectral profile used in each msVFA acquisition is shown here, centered on the pyruvate peak. The resonant frequency of each metabolite is indicated by vertical dashed lines. The magnitude and shape of the RF profile progressively changes with each acquisition to follow the msVFA trajectory.

These RF pulses were implemented in a version of our previously described chemical shift encoded [1-¹³C]pyruvate imaging pulse sequence^{155,206,247}. The modified pulse sequence was tested on a phantom containing 7 mol/L thermal [1-¹³C]sodium acetate phantom doped with a gadolinium-based contrast agent²⁵⁰ to ensure that RF pulses were scaling appropriately to prescribed flip angles over time. Frequency sweeps of the RF pulses were used to determine RF amplitude at various chemical shifts relevant to [1-¹³C]pyruvate imaging. The pulse sequence was run at a longer TR (1.5 s) than hyperpolarized experiments to permit for the T₁ recovery of the thermal phantom.

3.2.3 Animal Experiments

Six pregnant adult guinea pigs (gestational age = 48.2 ± 11.7 days, number of pups = 3.4 ± 0.9) were imaged under the approval of the institution's Animal Care Committee. Due to a technical failure of the RF coil in one experiment, one animal was excluded from analysis, leaving a total of 5 guinea pigs and 17 placentae. Animals were anesthetized

using 4.5% isoflurane with 2 L/min O₂ and maintained between 1.5-2.5% isoflurane with 2 L/min O₂. Animal vital signs (breathing, heart rate, temperature, blood oxygenation) were monitored throughout the experiment. Experiments were done at roughly the same time of day, and all animals were fasted for 2 hours before the experiment to standardize their metabolic state at the start of the experiment. All animals underwent an ultrasound examination three days prior to the MRI experiment to confirm pregnancy.

Each animal received two pyruvate injections during an experiment, one imaged with CFA and the other with msVFA. The order of the msVFA and CFA acquisitions were randomized between experiments. The second injection occurred approximately one hour after the first to allow time for hyperpolarization of the second dose of pyruvate.

For each injection, [1-¹³C]pyruvic acid (Cambridge Isotope Laboratories, Tewksbury, MA) containing 15 mM OX63 trityl radical (Oxford Instruments, Abingdon, UK) and 1 mM ProHance (Bracco, Milan, Italy) was hyperpolarized using the Hypersense DNP polarizer (Oxford Instruments). 75 mg/kg of the hyperpolarized 250mM [1-¹³C]pyruvate solution was delivered as a bolus injection via intravenous catheter into the saphenous vein over ~12 seconds, approximately 15 seconds after the dissolution had been released from the polarizer. Imaging was initiated 7.5 seconds after the start of pyruvate injection. An image was acquired every 7.5 seconds following the first acquisition, resulting in a total of seven images acquired at different time points. Hyperpolarized imaging was done using a 3D multiphase broadband fast gradient recalled multiecho pulse sequence with the following parameters: FOV 20 x 0.6 cm, slice 8.5 mm, BW 8.93 kHz, echoes 8, NEX = 1, ETL 4, first TE 4.2 ms, echo spacing 1.1 ms, acquisition time = 7.5 s.

T₁-weighted gradient echo (repetition time/echo time [TR/TE] = 5.1/2.4 ms, flip angle = 15°, number of averages = 4, slice thickness = 0.9 mm, total imaging time ~ 7 min) and T₂-weighted spin echo (TR/TE = 2000/120 ms, number of averages = 2, slice thickness = 0.9 mm, total imaging time ~ 7 min) images with 0.875 × 0.875 mm² in-plane resolutions were obtained as anatomical references for the ¹³C images. All experiments were done on a 3T MRI system (Discovery MR750, GE Healthcare, Waukesha, WI). ¹H images were acquired using a 32-element human cardiac coil array (In Vivo Corp., Gainesville, FL),

and ^{13}C images were acquired using a custom-built ^{13}C birdcage coil (Morris Instruments, Ottawa, Canada). Polarization levels were measured with an MQC spectrometer shortly after the dispensation of the sample for each injection.

3.2.4 Signal-to-Noise Ratios

The SNR of the *in vivo* images was calculated as the mean signal in a region of interest (ROI) divided by the standard deviation of signal in a signal-free ROI placed outside the animal. ROIs were drawn on the T_1 images for each placenta, maternal liver, and maternal kidney and then transferred to the HP ^{13}C images. SNR was calculated for each metabolite and acquisition. Paired t-tests were done to compare SNR for each metabolite in each ROI. Significance was defined at 0.05 for this test.

3.3 Results

Using the msVFA double Gaussian pulse, it is possible to achieve flip angles very similar to those of the optimal VFA calculated for each metabolite. Bloch simulations found that the predicted SNR using the flip angles implemented with msVFA was very similar to the predicted SNR using the exact VFA calculated for each metabolite. The SNR ratio summed over time for each metabolite using msVFA compared to the true VFA are as follows: 97% for pyruvate, 89% for lactate, 97% for alanine, and 95% for bicarbonate.

An increase in SNR in the placentae was observed for all metabolites using msVFA at time points up to 37.5 s, as displayed in Figure 3.3A. Statistically significant ($p < 0.00005$) increases in SNR were observed for pyruvate, lactate, and bicarbonate signal in the placentae using the msVFA acquisition compared to the CFA acquisition. An exception of this SNR increase in the placentae is the alanine signal; however, placental alanine SNR is very low, suggesting very little alanine was being produced in the placentae, and as such, it is not possible to increase the SNR when negligible signal is present.

Significant increases of pyruvate and lactate SNR were observed in the maternal liver ($p = 0.005$ and $p = 0.006$ respectively). There is no significant difference in the SNR of

alanine and bicarbonate in the maternal liver, but low SNR indicates that very little alanine and bicarbonate were produced in the maternal liver. A significant increase in pyruvate SNR was observed using msVFA in the maternal kidneys ($p = 0.015$) and trends of increased mean SNR were found using msVFA for all metabolites (see Figure 3.3C).

Typically, there is no increase in SNR using msVFA at the last time point (52.5 s) since there is not much hyperpolarized signal left to acquire at this time point. In some cases, SNR is increased in the CFA images at 52.5 s, and this may be due to the fact that CFA is less efficient at using all the signal by the end of the scan, leaving “wasted” signal. SNR was not corrected for polarization level in this analysis because all polarization measurements were between 5-7% and polarization level was not significantly different between msVFA and CFA, as determined by a paired t-test ($p = 0.15$).

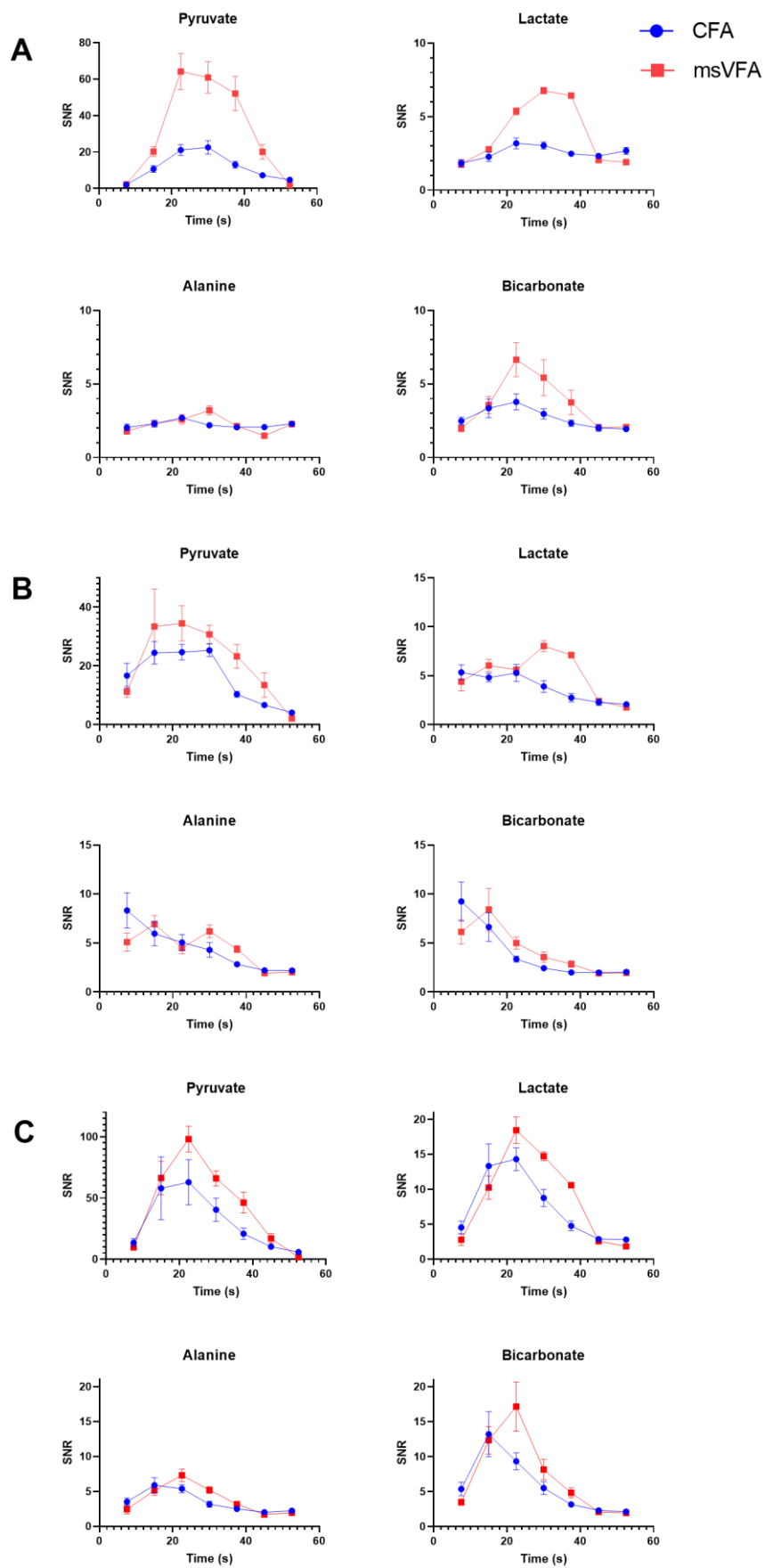


Figure 3.3: The mean SNR for each metabolite averaged over all (A) placenta, (B) maternal liver, and (C) maternal kidney ROIs are plotted here. The mean SNR at each time point may be compared between msVFA (red squares) and CFA (blue circles) acquisitions. A: The increased SNR provided by the msVFA acquisition is apparent for all metabolites, except alanine. This is likely due to limited production of alanine in the placenta providing very little metabolite signal that could be increased by the use of msVFA. B: The increased SNR provided by the msVFA acquisition is apparent for pyruvate and lactate, while there is limited improvement for alanine and bicarbonate. C: There appears to be increased mean SNR using msVFA for all metabolites in maternal kidney ROIs; however, these trends were not found to be significant. Note for all ROIs, the y-axis SNR scale is larger for pyruvate due to larger amount of signal from pyruvate compared to other metabolites.

Qualitatively, it can be appreciated that the increased SNR in images collected using the msVFA acquisition allows for a more easily discernible signal in less perfused and/or metabolically active areas than the lower SNR images acquired using the CFA method. This allows for a clearer distinction of low metabolism values from noise and detect small changes in metabolism. It was observed that signal in the fetal livers was distinguishable more often in images acquired using msVFA compared to CFA. An example of this is displayed in Figure 3.4, where there is more signal in placentae and fetal livers in the image acquired using the msVFA technique.

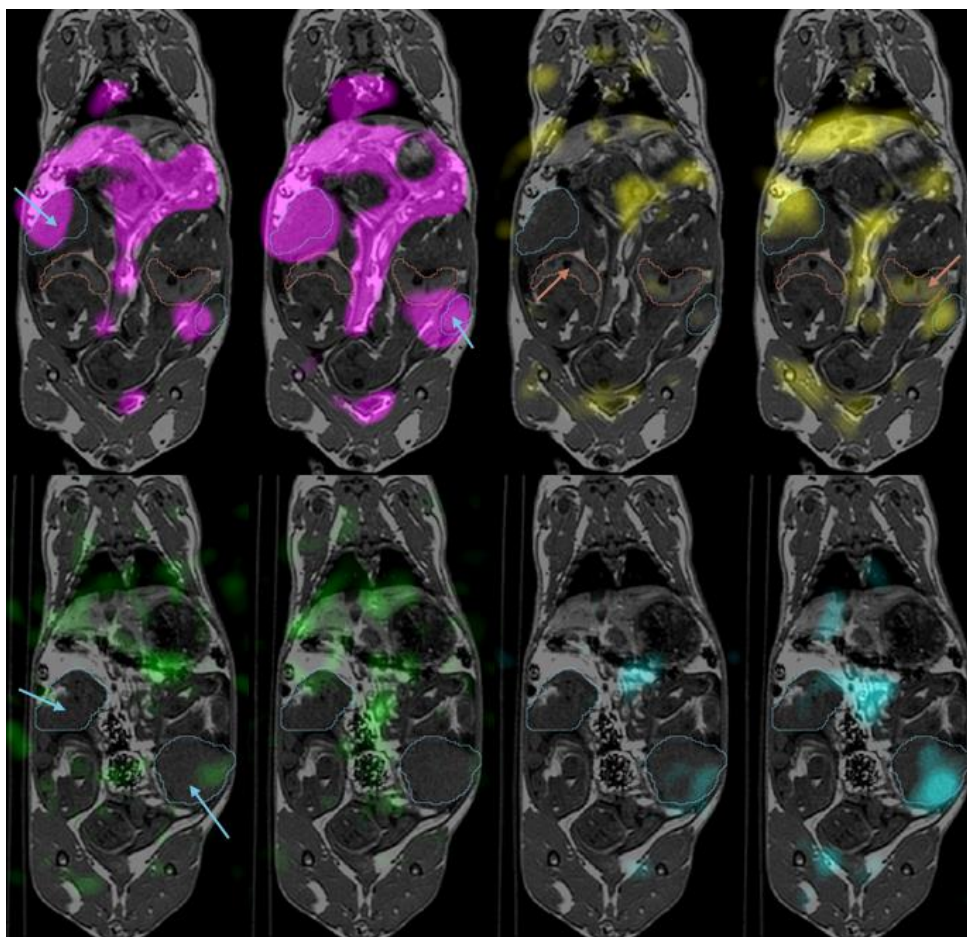


Figure 3.4: Typical hyperpolarized ^{13}C metabolite images overlaid on axial T_1 of the same animal at 30s post injection. Four pairs of images are shown here for each metabolite: pyruvate shown in magenta (top left), lactate in yellow (top right), alanine in green (bottom left), and bicarbonate in cyan (bottom right). For each pair of images, the image on the left was acquired using CFA and the image on the right acquired using msVFA. The image pairs have identical window and level for each metabolite. Placentae are indicated by blue arrows and outline; fetal livers are indicated by red arrows and outline. A different slice is shown for alanine and bicarbonate to show increased bicarbonate signal in the placenta using msVFA.

3.4 Discussion and Conclusions

In this study, it was demonstrated that a spectrally varying dynamic flip angle scheme individually optimized for each metabolite increases the SNR for all metabolites in time-resolved metabolic imaging. Up to 250% increases in SNR in pyruvate, lactate, and bicarbonate images of the placentae were observed; and similar SNR increases for metabolites in the maternal liver was demonstrated. The lack of alanine signal in the

maternal liver may be related to the known decrease of alanine aminotransferase enzyme activity enzymes in the liver that occurs during pregnancy, though this has only been reported on in human studies^{251,252}. The increased incidence of signal seen in fetal livers using msVFA compared to CFA leads us to believe that msVFA may be useful for metabolic analysis of fetal organs, where otherwise signal may not be distinguishable from noise.

The msVFA approach combats the rapid decay of hyperpolarized signal while accounting for the variation in metabolite concentrations and T_1 rates in hyperpolarized [1-¹³C]pyruvate MRI. The delivery of flip angles optimized for different metabolites in HP¹³C MRI builds on studies that have shown the advantage of VFA techniques to counter-act the rapid hyperpolarized decay^{244,245,253–255}. In these previous studies, VFA was optimized for one metabolite, usually either pyruvate or lactate, leading to sub-optimal flip angles for other metabolites.

Alternative approaches to optimize SNR for multiple metabolites have used spectrally-selective RF pulses which apply a unique flip angle for each metabolite but only excite one metabolite per RF pulse^{243,245,246,255}. These approaches to date have only been used to optimize up to two metabolites, usually pyruvate and lactate, and are usually implemented for imaging 2D slices. In our application of fetoplacental imaging, 3D imaging has the advantage of ensuring we can image multiple placentae and fetuses, which would be difficult if limited to a single 2D slice. The msVFA technique uses a spectrally varying flip angle which delivers unique flip angles for each metabolite during every RF excitation. The msVFA method does not limit the number of metabolites for which we may use optimized flip angles, and scaling up msVFA for more metabolites would be possible with a change in the RF excitation pulse shape. The current implementation of msVFA does not use the exact VFA flip angles for each metabolite due to limitations of the double Gaussian RF pulse. Delivering the exact desired flip angles may be possible as one could imagine using a more sophisticated RF pulse design; however, more complex pulses may be associated with additional complications such as higher SAR and likely longer pulses, which should be avoided in hyperpolarized experiments. While both methods of achieving multi-metabolite VFA are valid, unique

advantages and weaknesses exist for either method. This step-wise msVFA is considered to be a step toward a fully optimized VFA for 3D volumes.

The msVFA technique may be generalized for any set of metabolites in hyperpolarized imaging, assuming a rough estimate of the T_1 and metabolic rate constant is known. This would be valuable for hyperpolarized imaging of any metabolite, particularly if the end goal is quantitative analysis. The *in vivo* T_1 rates of these metabolites are difficult to measure and not well characterized; however, the msVFA optimization is dependent on the ratio of TR/T_1 and hyperpolarized imaging sequences typically use $TR \ll T_1$ due to the limited lifetime of the hyperpolarized signal. Therefore, the msVFA optimization calculation is relatively insensitive to errors of *in vivo* T_1 estimation. Similarly, flip angle optimization calculations from Xing et al.²⁴⁵ used assumed metabolic rate constant values in the estimation of the effective T_1 , which is inversely related to the rate constant. These metabolic rate constants are not well known *in vivo*, but as above, errors in rate constant estimation are not expected to affect SNR since $TR \ll T_{1\text{eff}}$ in this sequence.

The metabolic rate constants measured *in vivo* are typically on the order of 10^{-2} or 10^{-3} s^{-1} and precision is important when quantifying such small values. It is predicted that the increased SNR produced in images acquired with msVFA will improve the precision of metabolic rate fitting, enhancing the ability to detect small changes in these values. A future application of this work would be to quantify and compare metabolic rate constant values in diseased and healthy placentae using the msVFA acquisition.

In this study, there is a large degree of biological variation between our animals, including different maternal ages, gestational ages, and number of fetoplacental units. A diverse population was chosen for *in vivo* experiments to demonstrate that the advantages of using msVFA are applicable to different populations, meaning that the msVFA would not bias results when comparing two groups of animals.

For these ^{13}C acquisitions, the birdcage coil was used to limit the guinea pig volume we wished to image. To translate this technique to application in large animal or human studies, the RF pulse would need to be redesigned to include spatial selectivity. This adaptation is an important topic for future work.

In summary, it has been demonstrated that msVFA results in improved overall SNR for all metabolites in *in vivo* hyperpolarized [1-¹³C]pyruvate MRI. This was achieved using a spectrally varying RF pulse that increases in amplitude over the duration of the scanning protocol, preserving hyperpolarized ¹³C signal more effectively than a flip angle scheme that is constant over time. Although this study has focused on reporting the SNR for ROIs in the placenta, maternal liver, and maternal kidneys, this technique could improve SNR for any organ where metabolism is occurring. Additionally, this technique may be generalized for metabolic imaging of any hyperpolarized substrate. The msVFA technique improves hyperpolarized ¹³C images to allow better quantitative analysis of metabolic rates, and this is an important step in translation of hyperpolarized ¹³C MRI to clinical applications.

Chapter 4

4 Perfusion and oxygen saturation of the mid-pregnancy and near-term placenta measured by magnetic resonance imaging in a guinea pig model of pregnancy following lifelong Western diet consumption

4.1 Introduction

Consumption of a high-fat and high-sugar diet common to the Western world, known as the Western diet (WD), is linked to several metabolic diseases, including type II diabetes and cardiovascular disease⁵. Animal studies have shown that consuming high-fat diets in pregnancy can lead to postnatal negative health outcomes for offspring, including, but not limited to, cardiovascular dysfunction, obesity, and type II diabetes⁶⁹. Maternal obesity and metabolic syndrome, often induced by WD consumption, are associated with placental dysfunction⁶⁷. Placental dysfunction is a leading cause of stillbirth and major morbidities, including fetal growth restriction (FGR)^{72,73}, with the severity of these morbidities dependent on when they develop during gestation²⁵⁶. It is hypothesized that the WD negatively impacts placental function during pregnancy which, in turn, predisposes the fetus to increased risk of later life disease, though the mechanisms behind this association are unclear^{67,171}.

Historically, birth weights of the fetus and placenta have been used as a measure of placental efficiency; however, with modern imaging techniques, it is possible to obtain a clearer picture of fetoplacental physiology *in utero*^{99,100}. Ultrasound (US) is the most commonly used imaging modality for assessing fetoplacental growth but is limited in its ability to quantify placental function¹⁷¹. Umbilical artery Doppler US is used to provide an indirect measure of fetoplacental circulation^{171,257} but even with this technology, it remains difficult to detect microscopic changes to the placental microcirculation that are commonly associated with placental dysfunction¹⁷¹. US wave reflection is a technique

that can isolate US signal from the placental vasculature and has potential for detecting placental vascular pathology but is still in early pre-clinical stages of application²⁵⁸. To better understand physiological changes associated with diet during pregnancy, we investigate placental function using specialized MRI techniques. MRI has advantages over US, including superior soft-tissue contrast and the ability to make quantitative measurements related to tissue microstructure and function¹⁷¹. X-ray CT is often used to examine vascular function²⁵⁹, but, unlike MRI, it is not generally considered safe for use in pregnancy as it produces ionizing radiation²⁶⁰.

In this study, T_2^* mapping was used as an indirect measurement of blood oxygen saturation in the placenta, fetal brain, and fetal liver as T_2^* decay is sensitive to deoxygenated hemoglobin¹⁷¹. Diffusion-weighted imaging (DWI), specifically intravoxel incoherent motion (IVIM) techniques, were used to quantify diffusion and perfusion in the placenta, providing information on placental microstructure²⁶¹. IVIM provides estimates of the diffusion coefficient (D) related to cellular density and regional fibrosis, the pseudodiffusion coefficient (D^*) related to the perfusion of blood in the microcirculation, and the perfusion fraction (f) related to the density of blood vessels in a voxel¹⁶⁵.

The purpose of this study was to investigate the impact of lifelong maternal WD consumption on placental structure and function *in utero* in a guinea pig model at two points in pregnancy to observe any changes over gestation. T_2^* and IVIM measurements were used to provide placental oxygen saturation and microvascular information. Measurements of the fetus:placenta and fetal brain:liver volume ratios were used as well-defined proxy measurements of placental efficiency and fetal growth symmetry^{97,98}. Based on previous studies focusing on the impact of poor maternal nutrition^{108,262,263} on placental structure and function, it was postulated that lifelong maternal exposure to the WD would result in placental oxygen saturation and blood perfusion decreasing over gestation compared to placentae in sows consuming a control diet (CD).

4.2 Methods

4.2.1 Animals

All animals were housed at the Animalium of Western University, London, Canada. They were allowed feed and water ad libitum throughout the experiment and were examined regularly, and all efforts were made to minimize any distress as per the approved protocol and with veterinary oversight. This study was carried out in strict accordance with the recommendations of the Canadian Council of Animal Care (CCAC). The protocol was approved by the Animal Care Committee of Western University (AUP# 2019-116), and day-to-day operation was overseen by the Institution's post-approval monitoring program. Thirty female guinea pigs were weaned from birth randomly onto either a control diet (CD: 21.6% protein, 18.4% fat, 60% carbohydrates, N=15) or a Western diet (WD: 21.4% protein, 45.3% fat, 33.3% carbohydrates, N=15)²¹¹. The percentages listed indicate the calorie contribution from each macronutrient to the total calories of that diet. The two diets differ in terms of fat content (CD: 3% SFA, 4% MUFA, 11% PUFA; WD: 32% SFA, 12% MUFA, 2% PUFA) and carbohydrate content (CD: 10% sucrose, 40% corn starch; WD: 19% sucrose, 6.5% fructose, 9% corn starch; % by weight)²¹¹. Additionally, the WD had a higher caloric density of 4.2 kcal/g than the CD at 3.4 kcal/g²¹¹. The guinea pigs used in this study were mated in-house, and all had experienced one pregnancy prior to this study. The animals underwent MRI at either 40 ± 1 days (N = 13) or 63 ± 1 days (N = 17) gestation (term ~68 days)¹²². These gestational ages correspond to the mid-term (MT) and near-term (NT) groups, respectively. Each guinea pig was carrying between 1-5 pups, with the CD group containing 41 fetuses and the WD group containing 44 fetuses.

4.2.2 Imaging and Analysis

Animals were transported from the Animalium to the MRI suite and anesthetized using 4.5% isoflurane with 2L/min O₂. Once stable, the sow was maintained between 1.5-2.5% isoflurane with 2L/min O₂ and imaged at 3T (Discovery MR750, GE Healthcare, Waukesha, WI) using a 32-element cardiac coil (In Vivo Corp., Gainesville, FL).

Anatomical T₁-weighted gradient echo (TR/TE = 5.1 ms/2.4 ms, flip angle = 15°, number of averages = 4, slice thickness = 0.9 mm, total scan time ~ 7 min) and T₂-weighted spin echo (TR/TE = 2000 ms/120 ms, number of averages = 2, slice thickness = 0.9 mm, total scan time ~ 7 min) images with 0.875 × 0.875 mm² in-plane resolutions were acquired. Water-fat images were acquired using a modified IDEAL acquisition (TR/ΔTE = 9.4 ms/0.974 ms, echoes = 6, flip angle = 4°, number of averages = 4, slice thickness = 0.9 mm, total scan time ~ 13 min) with a 0.933 × 0.933 mm² in-plane resolution and reconstructed into R2* maps and PDFF images. DWI were acquired using a diffusion-weighted echo-planar imaging acquisition (TR/TE = 3940 ms/61 ms, number of averages = 2, in-plane resolution = 0.6 × 0.6 mm², slice thickness = 1 mm, total scan time ~ 8 min, with the following b-values: 10, 20, 35, 50, 65, 80, 95, 110, 125, 160, 200, 300, 400, 500, 600, 700, 750, 800, 900, and 1000 s/mm² acquired in 3 directions.

Regions of interest (ROIs) were manually segmented by L.S. (5 years of experience) using a digitizing monitor in 3D Slicer (version 4.10.0)²¹⁵ around the placental, fetal, fetal brain, and fetal liver volumes. Placenta, fetal liver, and fetal brain ROIs were then overlaid on R2* maps to calculate the mean T₂* in each volume. A Matlab (The MathWorks, Inc., 2008 version R2020a) IVIM fitting tool^{264,265} was used to produce voxel-wise maps of D, D*, and f within the placenta ROIs and the mean values were recorded. All measurements between the two diet groups were compared using a linear mixed model two-way ANOVA with a *post hoc* Tukey test to account for intra-litter effects, computed in R (R Foundation for Statistical Computing, Vienna, Austria). The mean and standard error of measurements are reported with significance defined at p < 0.05.

4.3 Results

The results are presented in a different sub-section for each type of measurement: volumes, oxygen saturation, and IVIM estimates. Within each sub-section, the results will be grouped by independent variables: gestational age disregarding maternal diet,

maternal diet group disregarding gestational age, and the interaction of gestational age and maternal diet.

4.3.1 Volumes and Volume Ratios

Without considering maternal diet, the fetal, placental, fetal liver, and fetal brain volumes significantly increased with gestational age ($p < 0.001$; Table 4.1). Normalizing fetal organs to fetal body volume, the fetal liver:body and fetal brain:body ratios decreased with gestational age ($p < 0.001$; Figure 4.1A, Table 4.1). The fetal brain:liver volume ratio also decreased with gestational age ($p < 0.001$; Figure 4.1C, Table 4.1) and the fetus:placenta volume ratio increased with gestational age ($p < 0.001$; Figure 4.1D, Table 4.1).

Disregarding gestational age, placental volume was increased in the WD group ($p < 0.05$; Table 4.1). There were no significant differences in absolute fetal, fetal liver, or fetal brain volumes with respect to diet (Table 4.1). The fetal liver:body and fetal brain:body ratios were significantly decreased in the WD group ($p < 0.01$; Figure 4.1A, B, Table 4.1) compared to the CD group. The fetal brain:liver volume ratio did not show any significant differences with respect to maternal diet (Figure 4.1C, 4.1A, Table 4.1). The fetus:placenta volume ratio showed a non-significant trend towards being decreased in the WD group ($p = 0.061$; Figure 4.1D, Table 4.1) compared to the CD group.

When considering the interaction of maternal diet and gestational age, the absolute fetal, placental, fetal liver, and fetal brain volumes were increased with gestational age within both the WD and CD groups ($p < 0.001$). The placental volume was increased in the WD group at NT ($p < 0.05$). There was a non-significant trend towards ($p = 0.061$) a decreased fetal volume in WD-fed sows compared to CD-fed sows at NT. The fetal liver:body and fetal brain:body ratios were decreased with gestational age in the CD group ($p < 0.001$) and decreased in the WD group compared to the CD group at MT ($p < 0.05$; Figure 4.1A, B). The fetal brain:liver volume ratio decreased with gestational age in the CD group (Figure 4.1A, B). The fetus:placenta volume ratio increased with gestational age within both diet groups and was decreased in WD-fed mothers at NT compared to CD-fed mothers at NT (Figure 4.1 D).

Table 4.1: Fetal and placental volumes for each diet and gestational age group.

Volume (mm ³)	CD	WD	p-value	MT	NT	p-value
Fetus	40322 ± 3299	33671 ± 3067	0.512	6234 ± 3459	67760 ± 2907	> 0.001
Placenta	5828 ± 449	6367 ± 418	> 0.05	2873 ± 471	9358 ± 396	> 0.001
Fetal liver	2956 ± 311	2681 ± 287	0.902	709 ± 25	4928 ± 272	> 0.001
Fetal brain	1890 ± 200	1642 ± 177	0.640	653 ± 209	2879 ± 168	> 0.001

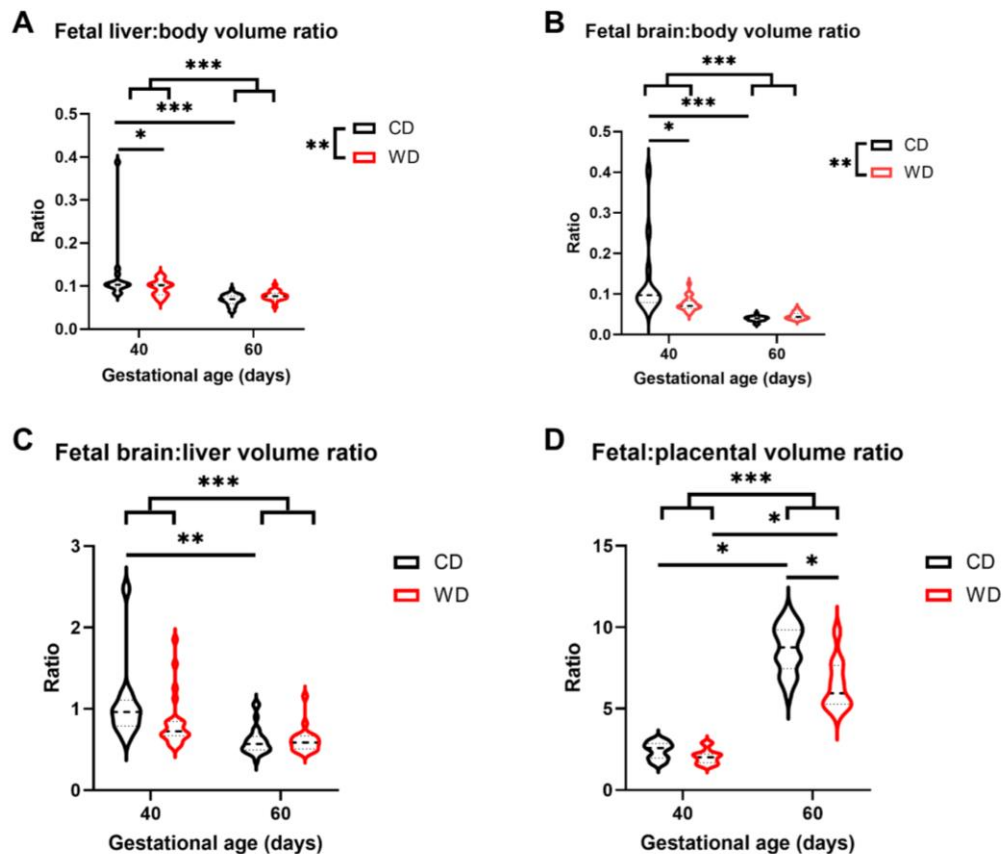


Figure 4.1: Fetal liver to fetal body (A), fetal brain to fetal body (B), fetal brain to fetal liver (C), and placenta to fetus (B) volume ratios measured for animals in each diet and gestational age group. The violin plots show the empirical distribution of the data, with a bold dashed line at the median and dotted lines at the first and third quartile. Horizontal lines indicate measurements that are different

from each other, pronged horizontal lines indicate differences between gestational age disregarding maternal diet, and pronged vertical lines indicate differences between diet groups disregarding gestational age. Significance is denoted by: * $p < 0.05$, ** $p < 0.01$, and *** $p < 0.001$.

4.3.2 Oxygen Saturation

Mean placental T_2^* measurements were significantly reduced with gestational age ($p < 0.001$; Figure 4.2A), not taking into account maternal diet. T_2^* measurements in the fetal liver ($p < 0.001$; Figure 4.2B) and brain ($p < 0.001$; Figure 4.2C) also decreased with gestational age.

Disregarding gestational age, mean placental T_2^* measurements were significantly decreased in WD-fed animals compared to CD-fed animals ($p < 0.05$; Figure 4.2A). T_2^* in the fetal liver and brain was not affected by maternal diet.

T_2^* significantly decreased from MT to NT in the CD-exposed placenta (Figure 4.2A). Decreased T_2^* in the placentae of WD-fed sows compared to CD-fed sows was significant at MT (Figure 4.2A). Mean T_2^* in the fetal liver and fetal brain were significantly decreased with gestational age in both the CD and WD groups (Figure 4.2B, C).

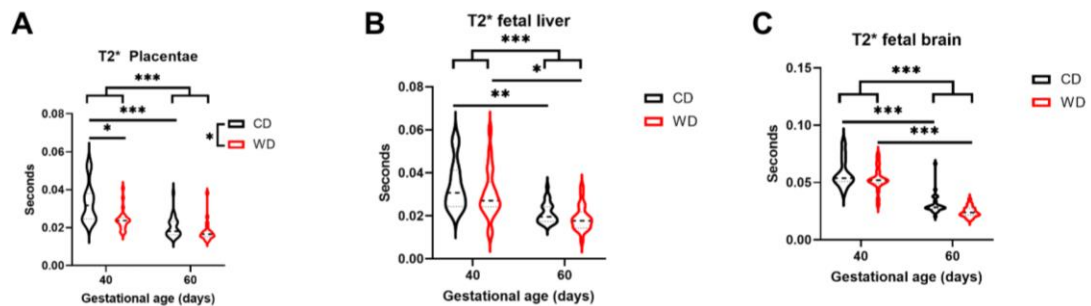


Figure 4.2: Mean T_2^* measurement in placenta (A), fetal liver (B) and fetal brain (C) in each diet and gestational age group. Horizontal lines indicate measurements that are different from each other, pronged horizontal lines indicate differences between gestational age disregarding maternal diet, and pronged vertical lines indicate differences between diet groups disregarding gestational age. Significance is denoted by: * $p < 0.05$, ** $p < 0.01$, and * $p < 0.001$.**

4.3.3 Placental Microstructure

Without considering maternal diet, D decreased over gestational age ($p < 0.01$; Figure 4.3A) and D^* increased with gestational age ($p < 0.001$; Figure 4.3B). The perfusion fraction did not change with gestational age.

Disregarding gestational age, D^* was increased in the WD-fed group ($p < 0.05$; Figure 4.3B). D and f did not differ with respect to maternal diet.

The interaction of gestational age and maternal diet was significant for D^* as it was significantly increased with gestational age in the CD-fed group. D showed a non-significant trend ($p = 0.068$) towards being decreased from MT to NT in the WD-fed animals.

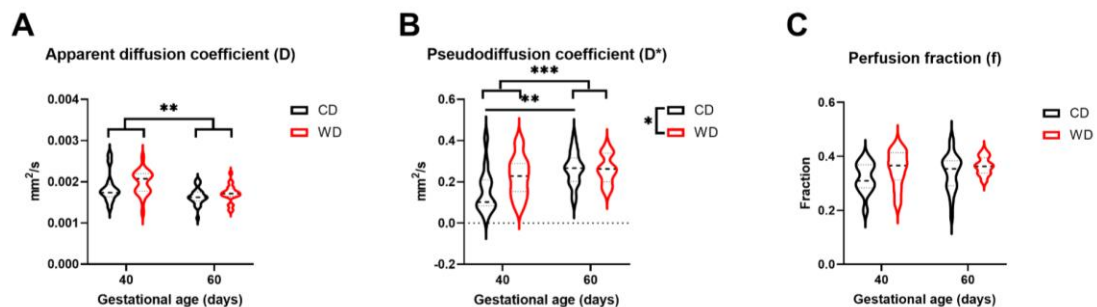


Figure 4.3: Mean diffusion parameters from all placentae: (A) apparent diffusion coefficient, (B) pseudodiffusion coefficient, and (C) perfusion fraction in each diet and gestational age group. Horizontal lines indicate measurements that are different from each other, pronged horizontal lines indicate differences between gestational age disregarding maternal diet, and pronged vertical lines indicate differences between diet groups disregarding gestational age. Significance is denoted by: * $p < 0.05$, ** $p < 0.01$, and * $p < 0.001$.**

4.4 Discussion

This study aimed to investigate the effect of a high-fat, high-sugar WD on placental oxygen saturation and microvasculature at mid- and near-term. IVIM techniques were used to non-invasively assess possible microstructural changes in placentae and T_2^* maps were used to assess oxygen saturation in the placenta, fetal liver, and fetal brain. The most intriguing results were that WD-fed sows produced placentae with lower blood

oxygen saturation and increased blood perfusion compared to their CD-fed counterparts. By NT, the WD-exposed placentae did not have significantly different T_2^* than CD-exposed placentae. It is hypothesized that the increased perfusion in WD animals is an adaptation to the low oxygen environment and results in improved oxygen saturation at NT. Even with this proposed vascular adaptation, the WD-fed animals displayed a lower fetus:placenta volume ratio at late gestation compared to the CD group. The most intriguing results are summarized in Figure 4.4.

A	Measurement	MT	NT	B	Measurement	CD	WD
	T_2^*	↓	≡		T_2^*	↓	≡
	D^*	≡	≡		D^*	↑	≡
	Placental efficiency	≡	↓		Placental efficiency	↑	↑
	Fetal liver:body	↓	≡		Fetal liver:body	↓	≡
	Fetal brain:body	↓	≡		Fetal brain:body	↓	≡

Figure 4.4: Summary of interesting results (A) in the WD group compared to CD group at MT and NT and (B) from MT to NT in CD and WD animals. The red “down” arrows indicate a decrease in the measurement, green “up” arrows indicate an increase in the measurement, and blue equals signs indicate no change in the measurement. All changes presented here are significant.

4.4.1 Volumes and Volume Ratios

Absolute measures of fetal body and placental volume over gestation were not impacted by maternal diet. Interestingly, when normalized to the fetal body volume, the fetal liver:body and fetal brain:body volume ratios were smaller in the WD group than the CD group at MT, indicating that fetal liver and brain growth are negatively impacted by the lifelong WD consumption of the sow. This may be related to the reduced placental T_2^* at MT in MD-fed sows, though the fetal liver and brain T_2^* measurements were not affected by maternal diet. Decreased fetal liver volumes have been previously documented in models of reduced placental blood flow²⁶⁶. Previous work in the pregnant guinea pig using the same WD has shown decreased fetal brain:body volume ratios late in gestation⁸, though here this relationship is only observed at MT.

The fetal brain to liver volume ratio was measured as an indicator of asymmetric FGR due to brain sparing as an adaptation to a poor *in utero* environment⁹⁷. There was no indication that maternal diet is causing FGR in this study.

It is not surprising that the fetus:placenta volume ratio increased with gestational age as the placenta reaches its maximum size early in pregnancy, whereas the fetus grows rapidly and reaches its maximum size in late pregnancy²⁶⁷. The fetus:placenta volume ratio is often used as an indicator of placental efficiency, where a low placental efficiency is associated with fetal death⁹⁸. The placental volume and placental efficiency were impacted by diet, with WD-fed sows having an increased placental volume and decreased fetus:placenta volume at NT. As pregnancy advances, the fetus:placenta ratio increases as a reflection of a more efficient placenta²⁶⁷. While this increase across gestation was observed in both diet groups, on average, the fetus:placental volume ratio increased by 382% in the CD group and increased by only 311% in the WD group. In human pregnancies, overweight and obese mothers have been shown to have heavier placentae^{268,269} and lower placental efficiencies²⁷⁰ compared to mothers with normal BMIs.

4.4.2 Oxygen Saturation

The mean T_2^* in the placenta, a measure related to blood oxygen saturation, significantly decreased from MT to NT in the CD group, while T_2^* was comparatively low in the WD group at both time points. The decrease in placental T_2^* decay with gestational age has been previously documented²⁷¹ and is likely due to a combination of decreasing placental oxygen over gestation^{272–274} and maturation of placental architecture over gestation^{275,276}. As the placenta ages, increased fibrin¹⁷¹ and calcification²⁷⁷ accelerate the T_2 decay, which is closely related to the T_2^* measurement.

Placental T_2^* may be a sensitive marker of placental dysfunction as decreased T_2^* has been associated with placental insufficiency and FGR in human and animal studies²⁷⁶. Diet impacted placental oxygen saturation in this study as T_2^* was significantly reduced in WD-fed sows compared to CD-fed sows at MT. A study in rats found reduced placental tissue oxygen saturation in mothers fed a lifelong high-fat diet compared to

those on a control diet²⁷⁸. Disruptions in oxygen transfer across the placenta may be caused by various factors, including maternal or fetal blood flow, the oxygen-carrying capacity of maternal or fetal blood, oxygen diffusion capacity, or fetoplacental oxygen consumption¹⁷¹. Using T_2^* mapping MRI technology does not allow us to elucidate the mechanism behind this observation, but histological studies may help determine the relationship between the WD and decreased placental oxygen saturation. The oxygen saturation in the fetal organs did not differ with respect to maternal diet, indicating that the fetal oxygen supply was not affected by the decreased placental oxygen saturation in WD-fed animals at MT.

4.4.3 Placental Microstructure

The guinea pig is an excellent model for placental studies as it shares a number of important similarities with the human placenta, including a similar discoidal, haemomonochorial structure and fetal/maternal transport barrier¹²². Even with these similarities, it is vital to consider differences in architecture between the human and guinea pig placenta when interpreting diffusion-weighted measurements, focusing on the labyrinthine structure of the GP placenta. Sections of the GP placenta perfused by both fetal and maternal blood vessels make up the labyrinth and are responsible for the majority of fetal and maternal exchange sites¹²². The maternal and fetal microvasculature run counter-current to each other, in parallel but opposite orientations, facilitating effective diffusion for oxygen and nutrient exchange¹²².

In contrast, the human placenta uses a less efficient immersion fixation for nutrient exchange where the fetal villous trees containing blood vessels are immersed in a slow-moving pool of maternal blood²⁷⁹. This exchange occurs in the cavity between the basal and chorionic plates where villous trees containing fetal microcirculation are bathed in maternal blood released from openings in the basal plate, which percolates through the intervillous space and is eventually drained through the uterine veins²⁷⁹. In human placental IVIM studies, the slow-moving maternal blood mimics free diffusion and contributes to signal loss described by D , while the fetal blood compartment flowing through convoluted villous trees contributes to signal loss described by D^* ²⁸⁰. In the case

of the guinea pig placenta, maternal blood is also moving through vessels, and therefore it cannot be assumed that the D measurement includes a significant contribution from the maternal blood. Instead, we may assume that the D* measurement represents blood perfusion from both the maternal and fetal microvasculature within the labyrinth structure.

D decreased with gestational age, which has been reported previously. This result is likely due to changes in microstructure as the placenta matures^{271,281,282}. D* appears to increase with gestational age in the CD group. Interestingly, WD-exposed pregnancies displayed a trend of elevated D* at mid-term that was maintained through gestation and was not significantly different from D* in the CD group at NT. This observation is unexpected, as placental vascularity has previously been shown to be reduced due to maternal obesity²⁶³ and maternal high-fat diet exposure²⁶² at both mid- and near-term in rodent models. Previous findings from maternal obesity studies have shown placental blood vessel immaturity related to hypoxia, increased inflammation, and cellular stress markers in the placenta¹⁰⁸. It should be noted that both of these studies utilized a high-fat diet and resulted in maternal obesity, whereas our study used a WD that included a high-sugar component in an animal model where WD did not induce maternal obesity.

It is speculated that increased perfusion measured in the placentae of WD-fed animals results from an increased blood volume flowing through the placental capillaries. While it may seem counter-intuitive that WD-fed placentae with lower T₂* values would have more vascular blood movement, we may be observing a placental adaptation to the low-oxygen environment in WD-exposed placentae at mid-term. Guinea pigs exposed to hypoxia have been shown to have increased fetal capillary volume density in the placental labyrinthine areas while still demonstrating reduced fetus:placenta weight ratios compared to guinea pigs in normoxic environments²⁸³. Other studies have supported the claim that hypoxic conditions can result in adaptations to the fetal capillaries in the placenta, manifesting as a dilation of the capillary sinusoids and thinning of the villous membrane²⁸⁴. Placentae with coiled, randomly branched, and dilated placental microvascular architecture have been reported in mice as a compensatory mechanism to facilitate increased oxygen supply to the developing fetus²⁸⁵.

In the current study, there were no changes in the perfusion fraction with respect to diet or gestational age, indicating that the high D^* in WD-fed sows at MT is not a result of any change in placental vascular density or angiogenesis. Instead, this increased perfusion may be explained by the dilation of capillaries previously reported in the literature²⁸⁵ as an adaptation to the low placental oxygen saturation in the WD group at MT. It is hypothesized that chronic maternal WD exposure results in a hypoxic placenta which promotes placental vascular adaptations. Physiologically, this vascular dilation may be related to the placenta growth factor and vascular endothelial growth factor, which are vasodilators known to be upregulated in human and rodent endothelial cells exposed to hypoxia^{286–290}.

4.4.4 Limitations, Future Work, and Conclusions

This study's limitations include a lack of *ex vivo* histology to verify MRI findings and potentially explore differences in the microvascular architecture between CD and WD-fed sows. The range of normal T_2^* ¹⁷¹ and IVIM²⁹¹ measurements has not yet been defined in the placenta, and particularly the guinea pig placenta, limiting our ability to categorize healthy and damaged placentae with quantitative MRI measurements.

Future work may include follow-up studies involving offspring of mothers in both diet groups to determine whether these placental changes resulted in later life metabolic disease. Measurements including body composition, glucose tolerance, liver fat percentage, and TG serum concentrations in the offspring may help determine any heightened risk of metabolic disease based on maternal diet. Diffusion tensor imaging (DTI) provides additional information on the trajectory of perfusion and has been performed in the human placenta to distinguish between normal and non-functional tissue in healthy and FGR pregnancies²⁹². Although it may be challenging to implement in the small guinea pig placenta, DTI may provide more information on the spatial distortion of functional placental tissue and potential changes in microvessel structure with respect to maternal diet¹⁶³. Another future aim of this work is to determine spatial patterns of T_2^* and IVIM measurements as they appear to be heterogeneous across the placenta. It would be fascinating to compare oxygen saturation, diffusion, and perfusion in areas of the

placenta associated with maternal and fetal blood supply to further explore the mechanisms behind observed changes of T_2^* and perfusion. Due to the complex architecture of the guinea pig placenta, methods used to segment maternal and fetal sections of the human placenta would likely not be translatable. Additionally, the small size of the guinea pig placenta makes it difficult to visualize placental substructure at a clinical MRI field strength.

In conclusion, it was found that CD-exposed placentae had increased placental blood perfusion from mid-to near-term while WD-exposed placentae displayed high perfusion at both gestational ages, possibly compensating for low oxygen saturation at mid-term. WD-exposed placentae had lower oxygen saturation and were associated with smaller fetal liver:body and fetal brain:body volume ratios at MT, but these measurements did not differ from the CD group at NT. Despite some improvements at NT, low placental efficiency was observed in the WD group, which may be a "trade-off" for the earlier placental adaptations. Further studies focusing on the WD's effect on placental function should explore the mechanisms behind the observed changes in placental T_2^* and D^* associated with diet. Insight into these WD-related mechanisms may help diagnose and evaluate therapeutic interventions for placental insufficiency in the future.

Chapter 5

5 Conclusions

This chapter will conclude the thesis with suggestions for future work and a summary of the research, highlighting the significance of the scientific contributions presented in this thesis.

5.1 Thesis Summary

The Western diet has a multifaceted impact on physiology, shown in this thesis to manifest as metabolic changes in the liver and vascular adaptations in the placenta. It was demonstrated that lifelong exposure to the WD results in abnormal pyruvate metabolism in the liver in conjunction with fat accumulation typical of NAFLD. The main finding of this work, described in Chapter 2, was the observation of increased lactate production observed in the livers of WD-fed animals and validated by *ex vivo* enzyme activity measurements. In Chapter 4, the effect of a lifelong maternal WD on placental oxygenation and blood perfusion was observed at mid- and near term. The findings from this study indicate that maternal WD exposure results in poor blood oxygen saturation in the placenta at mid-gestation, which was hypothesized to trigger a vascular response that increased placental blood perfusion. This adaptation resulted in increased oxygen saturation in the WD-exposed placentae late in gestation, though low placental efficiency was observed in these animals.

This thesis demonstrates the use of multiple MRI techniques to study metabolic disease, including hyperpolarized ^{13}C MRS, hyperpolarized ^{13}C MRI, chemical shift-encoded imaging, and diffusion-weighted imaging. The variety of information obtained using different MRI techniques and contrast testify to the versatility of MRI and its capability to provide structural and functional information relevant to *in vivo* processes. Although MRI has been in use for biomedical applications since the 1970s¹²⁵, novel techniques such as hyperpolarized MRI are still evolving and being improved upon. This evolution is evidenced in Chapter 3, where a novel RF pulse trajectory was established to improve SNR in HP MRI. This technical improvement was shown to increase SNR in our *in vivo*

experiments and may allow for more precise measurements of metabolic kinetics in future work.

5.1.1 Significance and Impact

The work from Chapter 2 of this thesis demonstrated *in vivo* metabolic changes in the livers of animals with diet-induced NAFLD. These results were validated using *ex vivo* measurements and promote the use of HP [1-¹³C]pyruvate MRS in evaluating liver disease. The increased production of lactate in these livers indicates, alongside other animal studies, that [1-¹³C]lactate may be a useful biomarker of early-stage NAFLD and a non-invasive diagnostic alternative to liver biopsy.

Chapter 3 described a technical improvement in image acquisition for HP [1-¹³C]pyruvate MRI that may be adapted for any probe or application of HP MRI. Improvement in SNR from the msVFA contributes to the overall goal of overcoming difficulties associated with HP MRI and supporting HP MRI as a feasible imaging option in routine clinical use. This work represents a small step towards implementing HP MRI in human studies of pregnancy and metabolic disease.

The findings from Chapter 4 of this thesis demonstrate, for the first time, a placental vascular response to an adverse environment promoted by maternal diet. Although similar adaptations have been reported in cases of hypoxia, studying this response in the context of maternal diet may provide important information on the placenta's role in fetal programming that may impact the later-life health of the offspring. Hopefully, this study will prompt further investigation into the underlying mechanisms connecting maternal diet, placental oxygen saturation, and placental perfusion.

In conclusion, the work in this thesis demonstrated and promoted the benefits of advanced MRI techniques to study metabolic disease, which is not a conventional application of these imaging methods. Further, this thesis has highlighted two examples of an adverse response to a lifelong WD and may inspire future work to investigate the underlying mechanisms of these changes and the efficacy of treatments for metabolic disease.

5.2 Future Directions

5.2.1 Longitudinal Studies

Longitudinal studies would be beneficial in future work related to the research presented in Chapters 2 and 4 of this thesis. In Chapter 2, metabolic changes were observed in conjunction with NAFLD in the guinea pig as a result of a lifelong WD exposure. One of the advantages of HP MRI is its ability to provide information about *in vivo* metabolism without invasive or harmful effects. Repeating this study with imaging experiments at multiple time points would allow us to understand better when these metabolic changes occur during the development of NAFLD and whether these changes remain stagnant over time as the disease progresses. These additional experiments would be especially important to observe in the progression of NAFLD to NASH to pinpoint early biomarkers of the transition from benign steatosis to more harmful hepatitis in the liver.

Related to pregnancy studies focused on maternal diet, the DOHaD hypothesis states that the lifelong health of an offspring is impacted by its *in utero* environment⁸¹. In Chapter 4, evidence that maternal WD consumption impacts placental function was presented, and it would be interesting to perform follow-up studies involving offspring from these mothers to determine if the placental changes resulted in any later life metabolic disease. Further, sex-specific abnormalities in the offspring should be investigated as there is evidence that maternal metabolic health has a sex-specific effect on the placenta¹⁰⁴.

5.2.2 Diet Intervention and Exercise Studies

In this work, adverse effects of WD consumption in the liver and placenta were demonstrated. As with many metabolic diseases, primary treatment typically involves calorie reduction via diet intervention and suggestions for increased physical activity²⁶. It is known that early-stage NAFLD is reversible with gradual weight loss⁵⁶, leading to decreased liver volume and hepatic fat accumulation²³⁴. It is unclear whether the metabolic adaptation of increased lactate production observed in Chapter 2 would revert or persist with these diet and exercise interventions. An HP ¹³C imaging study designed

to induce NAFLD followed by a period of calorie restriction and/or increased exercise is proposed to investigate the impact of these interventions on *in vivo* hepatic metabolism.

Benefits of a healthy diet and exercise have been shown in the placenta to aid in placental growth²⁹³, prevent placental hypoxia²⁹⁴, prevent placental overgrowth, and reverse impaired placental vascularization²⁶³. In Chapter 4, adverse effects in the placenta of WD-fed sows related to vascularization and oxygen saturation were observed. It would be interesting to conduct a study comparing placental oxygenation and blood perfusion between mothers fed a WD with and without diet or exercise intervention. This could also lead to a longitudinal study comparing the metabolic health of the offspring from each group later in life.

5.2.3 HP [2-¹³C]pyruvate MRI/MRS

Chapters 2 and 3 of this thesis focused on MR spectroscopy and imaging of [1-¹³C]pyruvate and its downstream metabolites to study metabolic disease. Abnormal pyruvate metabolism in the livers of WD-fed animals were observed in Chapter 2, indicated by an increased rate of lactate production. Based on related enzyme activity results, it was hypothesized that WD-fed animals also experienced decreased bicarbonate production, suggesting fewer pyruvate molecules undergoing oxidative phosphorylation via the TCA cycle compared to CD-fed animals. Using [1-¹³C]pyruvate as the hyperpolarized probe limits our ability to visualize metabolism within the TCA cycle. A similar study using a hyperpolarized [2-¹³C]pyruvate probe would be useful to determine the metabolic fate of pyruvate in the TCA cycle and determine whether diet influences aerobic metabolism in the liver. HP [2-¹³C]pyruvate is less commonly used as it has a shorter T₁ and less polarization than [1-¹³C]pyruvate¹⁹⁶ but nevertheless is capable of providing information involving the integrity of the TCA cycle in different metabolic states.

Previous research in the McKenzie lab has observed no significant changes with respect to maternal diet and pyruvate placental metabolism using HP [1-¹³C]pyruvate MRI; however, it may be beneficial to repeat this study using [2-¹³C]pyruvate imaging as maternal diet may have an impact on the placental aerobic metabolism within the TCA

cycle which is not detectable using [1-¹³C]pyruvate²⁹⁵. The general RF pulse strategy presented in Chapter 3 may be tailored and implemented to increase SNR of [2-¹³C]pyruvate and its downstream metabolites for HP MRI in these applications.

5.2.4 HP ³¹P MRI

Metabolic dysfunction resulting in the buildup of excess lactate may lead to acidosis, resulting in abnormal changes to local pH in extreme cases⁷⁴. Severe chronic hypoxia, which may be induced by altered metabolism and tissue remodelling in NAFLD, may also lead to pH changes in the liver²⁹⁶. Decreased oxygen saturation in the placenta, demonstrated in Chapter 4, can result in hypoxia over time and may be associated with fetoplacental acidosis, resulting in deviations from normal pH⁷⁴. The ability to detect extracellular pH non-invasively would be beneficial for both of these applications.

Since pH is regulated by the bicarbonate buffer system, the ratio of bicarbonate and CO₂ can be used to estimate pH²⁹⁷. While this is possible to measure with HP ¹³C MRI, images of these metabolites typically have low SNR and are difficult to acquire²⁹⁷. Other compounds such as inorganic phosphate experience chemical shifts at different pH²⁹⁸. Conveniently, ³¹P is NMR-sensitive and 100% abundant, motivating the use of inorganic phosphate's pH-sensitive chemical shift to construct pH maps using MRI. As with most non-proton nuclei, it is difficult to acquire ³¹P MR images due to low concentration and low γ , but it has recently been shown that inorganic phosphate can be hyperpolarized via d-DNP²⁹⁸. This technique has been used to evaluate pH in *ex vivo* samples using MRS, with a hyperpolarized solution of inorganic phosphate with phosphocreatine as a reference²⁹⁸. It is theoretically possible to use this technique for *in vivo* MRI, using chemical shift-encoded imaging to construct maps of extracellular pH. An adaptation to the optimized RF pulse trajectory presented in Chapter 3 can be applied to HP ³¹P MRI to increase image SNR further. This is an area of future research in the McKenzie lab and may be applied in studies of NAFLD and placental insufficiency.

5.2.5 Human studies

The imaging experiments in this thesis made use of a guinea pig model. Animal models provide many advantages, including control of the animals' environment and diet, a short lifespan and gestation, and the ability to extract tissue components for *ex vivo* comparisons. The disadvantage of animal models is their physiological differences to humans and the need for anesthesia in imaging studies which may impact metabolism during imaging. While the guinea pig is an ideal model for studying metabolic disease and pregnancy due to its lipoprotein profile¹¹⁶ and placental structure¹²⁰ being similar to humans, there are also many differences. A major difference between the guinea pig and human is the tendency for humans to become obese when exposed to the WD while the guinea pig remains lean, though still displaying metabolic consequences such as increased visceral adipose tissue²⁹⁹. Regarding pregnancy, the guinea pig produces multiple offspring while humans typically birth one offspring per pregnancy, which may cause differences in resource allocation during gestation¹²². As discussed in Chapter 4, despite the similarities in placental structure between the two animals, there remain differences regarding placental vasculature, with the guinea pig displaying a labyrinthine structure¹²².

To overcome the limitations of an animal model, clinical studies provide more accurate information on human metabolism and disease. The eventual goal of these advanced MRI techniques is their application in clinical settings. All imaging experiments in this thesis were performed on a commercial clinical 3T MRI and are theoretically possible to replicate in human subjects.

HP ¹³C MRI and MRS have been implemented in clinical studies and have demonstrated safety and success in identifying biomarkers for oncologic applications³⁰⁰. To date, only preclinical studies of HP ¹³C MRI/MRS for NAFLD have been published; however, previous work^{205,301} and work presented in Chapter 2 provide evidence of its use for identifying potential metabolic biomarkers of NAFLD and motivation for its use in human studies. Work presented in Chapter 3 that demonstrated improved SNR for HP ¹³C MRI may also be implemented in clinical studies that pose additional challenges of larger

field of view coverage and longer durations for delivery of the hyperpolarized injection into the subject.

Diffusion-weighted imaging and IVIM methods have been implemented in the human placenta^{302,303}, demonstrating safety and adequate sensitivity. These imaging techniques have not yet been implemented to study the effects of maternal diet on placental function in humans, though the work presented in Chapter 4 motivates this investigation. In Chapter 4, an adaptation of the placental vasculature in response to poor oxygenation influenced by maternal diet was demonstrated in the guinea pig. It would be interesting to observe if this placental adaptation is common to the human placenta as well. The human placenta also provides an opportunity to compare changes in different placental compartments, as they are more easily discernable than in a small animal model²⁸⁰. Translation of these MRI techniques to clinical studies may enable us to learn more about physiological changes associated with diet in the human body and potentially lead to improvements in personalized patient care.

References

1. Smith, L. M. *et al.* In Vivo Magnetic Resonance Spectroscopy of Hyperpolarized [1-¹³C]Pyruvate and Proton Density Fat Fraction in a Guinea Pig Model of Non-Alcoholic Fatty Liver Disease Development After Life-Long Western Diet Consumption. *J. Magn. Reson. Imaging* (2021). doi:10.1002/jmri.27677
2. Smith, L. M., Wade, T. P., Friesen-Waldner, L. J. & McKenzie, C. A. Optimizing SNR for multi-metabolite hyperpolarized carbon-13 MRI using a hybrid flip-angle scheme. *Magn. Reson. Med.* **84**, 1510–1517 (2020).
3. Cordain, L. *et al.* Origins and evolution of the Western diet: Health implications for the 21st century. *American Journal of Clinical Nutrition* **81**, 341–354 (2005).
4. Ruiz-Núñez, B., Dijck-Brouwer, D. A. J. & Muskiet, F. A. J. The relation of saturated fatty acids with low-grade inflammation and cardiovascular disease. *Journal of Nutritional Biochemistry* **36**, 1–20 (2016).
5. Christ, A., Lauterbach, M. & Latz, E. Western Diet and the Immune System: An Inflammatory Connection. *Immunity* **51**, 794–811 (2019).
6. Zinöcker, M. K. & Lindseth, I. A. The western diet–microbiome–host interaction and its role in metabolic disease. *Nutrients* **10**, (2018).
7. Varlamov, O. Western-style diet, sex steroids and metabolism. *Biochim. Biophys. Acta - Mol. Basis Dis.* **1863**, 1147–1155 (2017).
8. Sinclair, K. J. *et al.* Quantification of fetal organ volume and fat deposition following in utero exposure to maternal Western Diet using MRI. *PLoS One* **13**, (2018).
9. Osadnik, K. *et al.* Metabolically healthy obese and metabolic syndrome of the lean: The importance of diet quality. Analysis of MAGNETIC cohort. *Nutr. J.* **19**, 1–13 (2020).
10. Elliott, S. S., Keim, N. L., Stern, J. S., Teff, K. & Havel, P. J. Fructose, weight gain, and the insulin resistance syndrome. *Am. J. Clin. Nutr.* **76**, 911–922 (2002).
11. Stanhope, K. L. Sugar consumption, metabolic disease and obesity: The state of the controversy. *Crit. Rev. Clin. Lab. Sci.* **53**, 52–67 (2016).
12. Bray, G. A. Soft drink consumption and obesity: it is all about fructose. *Curr. Opin. Lipidol.* **21**, 51–57 (2010).
13. Ter Horst, K. W. & Serlie, M. J. Fructose consumption, lipogenesis, and non-alcoholic fatty liver disease. *Nutrients* **9**, 1–20 (2017).
14. Gray, L. R., Tompkins, S. C. & Taylor, E. B. Regulation of pyruvate metabolism and human disease. *Cellular and Molecular Life Sciences* **71**, 2577–2604 (2014).
15. Mayes, P. A. Intermediary metabolism of fructose. *American Journal of Clinical Nutrition* **58**, 754S-765S (1993).
16. The World Health Organization. Healthy Diet. *Fact Sheets* (2020). Available at: <https://www.who.int/news-room/fact-sheets/detail/healthy-diet>. (Accessed: 30th November 2020)
17. Huang, P. L. A comprehensive definition for metabolic syndrome. *DMM Dis. Model. Mech.* **2**, 231–237 (2009).
18. Madhu, K., Manjunath, C., Rawal, J. & Irani, P. Atherogenic dyslipidemia. *Indian J. Endocrinol. Metab.* **17**, 969 (2013).
19. Alberti, G., Zimmet, P., Shaw, J. & Grundy, S. M. The IDF consensus worldwide definition

- of the metabolic syndrome. *IDF Communications* (2006). doi:10.1159/000282084
20. Després, J.-P. & Lemieux, I. Abdominal obesity and metabolic syndrome[J] Type 2 diabetes and heart rate variability View project. (2007). doi:10.1038/nature05488
 21. Wildman, R. P. *et al.* The obese without cardiometabolic risk factor clustering and the normal weight with cardiometabolic risk factor clustering prevalence and correlates of 2 phenotypes among the US population (NHANES 1999-2004). *Obstet. Gynecol. Surv.* **63**, 783–784 (2008).
 22. Fox, C. S. *et al.* Abdominal visceral and subcutaneous adipose tissue compartments: Association with metabolic risk factors in the framingham heart study. *Circulation* **116**, 39–48 (2007).
 23. Lebovitz, H. E. The relationship of obesity to the metabolic syndrome. *Int. J. Clin. Pract. Suppl.* 18—27 (2003).
 24. Wang, H., Chen, Y. E. & Eitzman, D. T. Imaging body fat techniques and cardiometabolic implications. *Arterioscler. Thromb. Vasc. Biol.* **34**, 2217–2223 (2014).
 25. Shab-Bidar, S., Golzarand, M., Hajimohammadi, M. & Mansouri, S. A posteriori dietary patterns and metabolic syndrome in adults: A systematic review and meta-analysis of observational studies. *Public Health Nutr.* **21**, 1681–1692 (2018).
 26. Rodríguez-Monforte, M., Sánchez, E., Barrio, F., Costa, B. & Flores-Mateo, G. Metabolic syndrome and dietary patterns: a systematic review and meta-analysis of observational studies. *Eur. J. Nutr.* **56**, 925–947 (2017).
 27. Kim, J. Y., He, F. & Karin, M. From Liver Fat to Cancer: Perils of the Western Diet. *Cancers (Basel)*. **13**, 1095 (2021).
 28. Friedman, S. L., Neuschwander-Tetri, B. A., Rinella, M. & Sanyal, A. J. Mechanisms of NAFLD development and therapeutic strategies. *Nat. Med.* **24**, 908–922 (2018).
 29. Marchesini, G., Petta, S. & Dalle Grave, R. Diet, weight loss, and liver health in nonalcoholic fatty liver disease: Pathophysiology, evidence, and practice. *Hepatology* **63**, 2032–2043 (2016).
 30. Westerbacka, J. *et al.* Dietary fat content modifies liver fat in overweight nondiabetic subjects. *J. Clin. Endocrinol. Metab.* **90**, 2804–2809 (2005).
 31. Salt, W. B. Nonalcoholic fatty liver disease (NAFLD): a comprehensive review. *J. Insur. Med. YORK THEN DENVER--* **36**, 27–41 (2004).
 32. Schwarz, J.-M. *et al.* Effect of a High-Fructose Weight-Maintaining Diet on Lipogenesis and Liver Fat. *J. Clin. Endocrinol. Metab.* **100**, 2434–2442 (2015).
 33. Yang, P. *et al.* Western diet induces severe nonalcoholic steatohepatitis, ductular reaction, and hepatic fibrosis in liver CGI-58 knockout mice. *Sci. Rep.* **10**, 1–13 (2020).
 34. Gabbia, D. *et al.* Western Diet-Induced Metabolic Alterations Affect Circulating Markers of Liver Function before the Development of Steatosis. *Nutrients* **11**, (2019).
 35. Dowman, J. K., Tomlinson, J. W. & Newsome, P. N. Pathogenesis of non-alcoholic fatty liver disease. *QJM An Int. J. Med.* **103**, 71–83 (2010).
 36. Sangüesa, G. *et al.* The Addition of Liquid Fructose to a Western-Type Diet in LDL-R–/– Mice Induces Liver Inflammation and Fibrogenesis Markers without Disrupting Insulin Receptor Signalling after an Insulin Challenge. *Nutrients* **9**, (2017).
 37. Vial, G. *et al.* Effects of a high-fat diet on energy metabolism and ROS production in rat liver. *J. Hepatol.* **54**, 348–356 (2011).

38. Jarukamjorn, K., Jearapong, N., Pimson, C. & Chatuphonprasert, W. A high-fat, high-fructose diet induces antioxidant imbalance and increases the risk and progression of nonalcoholic fatty liver disease in mice. *Scientifica (Cairo)*. **2016**, (2016).
39. Balakumar, M. *et al.* High-fructose diet is as detrimental as high-fat diet in the induction of insulin resistance and diabetes mediated by hepatic/pancreatic endoplasmic reticulum (ER) stress. *Mol. Cell. Biochem.* **423**, 93–104 (2016).
40. Choi, Y., Abdelmegeed, M. A. & Song, B. J. Diet high in fructose promotes liver steatosis and hepatocyte apoptosis in C57BL/6J female mice: Role of disturbed lipid homeostasis and increased oxidative stress. *Food Chem. Toxicol.* **103**, 111–121 (2017).
41. Li, J. *et al.* Accumulation of endoplasmic reticulum stress and lipogenesis in the liver through generational effects of high fat diets. *J. Hepatol.* **56**, 900–907 (2012).
42. Nassir, F. & Ibdah, J. A. Role of mitochondria in nonalcoholic fatty liver disease. *International Journal of Molecular Sciences* **15**, 8713–8742 (2015).
43. Lau, J. K. C., Zhang, X. & Yu, J. Animal models of non-alcoholic fatty liver disease: current perspectives and recent advances. *J. Pathol.* **241**, 36–44 (2017).
44. Loomba, R. & Sanyal, A. J. The global NAFLD epidemic. *Nat. Rev. Gastroenterol. Hepatol.* **10**, 686–690 (2013).
45. Chalasani, N. *et al.* The diagnosis and management of non-alcoholic fatty liver disease: Practice Guideline by the American Association for the Study of Liver Diseases, American College of Gastroenterology, and the American Gastroenterological Association. *Hepatology* **55**, 2005–2023 (2012).
46. Musso, G., Gambino, R., Cassader, M. & Pagano, G. Meta-analysis: Natural history of non-alcoholic fatty liver disease (NAFLD) and diagnostic accuracy of non-invasive tests for liver disease severity. (2010). doi:10.3109/07853890.2010.518623
47. Wong, V. W.-S., Adams, L. A., de Lédinghen, V., Wong, G. L.-H. & Sookoian, S. Noninvasive biomarkers in NAFLD and NASH — current progress and future promise. *Nat. Rev. Gastroenterol. Hepatol.* **15**, 461–478 (2018).
48. Eslam, M. *et al.* MAFLD: A Consensus-Driven Proposed Nomenclature for Metabolic Associated Fatty Liver Disease. *Gastroenterology* **158**, 1999–2014.e1 (2020).
49. Eslam, M. *et al.* A new definition for metabolic dysfunction-associated fatty liver disease: An international expert consensus statement. *Journal of Hepatology* **73**, 202–209 (2020).
50. Lin, S. *et al.* Comparison of MAFLD and NAFLD diagnostic criteria in real world. *Liver Int.* **40**, 2082–2089 (2020).
51. Ameer, F., Scanduzzi, L., Hasnain, S., Kalbacher, H. & Zaidi, N. De novo lipogenesis in health and disease. *Metabolism: Clinical and Experimental* **63**, 895–902 (2014).
52. Wattacheril, J. & Sanyal, A. J. Lean NAFLD: an Underrecognized Outlier. *Curr. Hepatol. Reports* **15**, 134–139 (2016).
53. Fachrureza, M. & Pratomo, B. Lean Non-Alcoholic Fatty Liver Disease (NAFLD). *Clin. Res. J. Intern. Med.* **1**, 46–54 (2020).
54. Vos, B. *et al.* Lean non-alcoholic fatty liver disease (Lean-NAFLD): a major cause of cryptogenic liver disease. *Acta Gastroenterol Belg* **74**, 389–394 (2011).
55. Cruz, A. C. Dela *et al.* 379 characteristics and long-term prognosis of lean patients with nonalcoholic fatty liver disease. *Gastroenterology* **146**, S-909 (2014).
56. Bradbury, M. W. Lipid metabolism and liver inflammation. I. Hepatic fatty acid uptake:

- Possible role in steatosis. *Am. J. Physiol. - Gastrointest. Liver Physiol.* **290**, 194–198 (2006).
57. Medina-Remón, A., Kirwan, R., Lamuela-Raventós, R. M. & Estruch, R. Dietary patterns and the risk of obesity, type 2 diabetes mellitus, cardiovascular diseases, asthma, and neurodegenerative diseases. *Crit. Rev. Food Sci. Nutr.* **58**, 262–296 (2018).
 58. Siega-Riz, A. M., Bodnar, L. M. & Savitz, D. A. What are pregnant women eating? Nutrient and food group differences by race. *Am. J. Obstet. Gynecol.* **186**, 480–486 (2002).
 59. Fuchs, F. *et al.* Impact of maternal obesity on the incidence of pregnancy complications in France and Canada. *Sci. Rep.* **7**, 10859 (2017).
 60. Chu, S. Y. *et al.* Maternal obesity and risk of stillbirth: a metaanalysis. *Am. J. Obstet. Gynecol.* **197**, 223–228 (2007).
 61. Carmichael, S. L. *et al.* Prepregnancy Obesity and Risks of Stillbirth. (2015). doi:10.1371/journal.pone.0138549
 62. Galtier-Dereure, F., Boegner, C. & Bringer, J. Obesity and pregnancy: complications and cost. *Am. J. Clin. Nutr.* **71**, 1242S-1248S (2000).
 63. Ramachenderan, J., Bradford, J. & McLean, M. Maternal obesity and pregnancy complications: A review. *Aust. New Zeal. J. Obstet. Gynaecol.* **48**, 228–235 (2008).
 64. Koebnick, C., Heins, U. A., Hoffmann, I., Dagnelie, P. C. & Leitzmann, C. Folate Status during Pregnancy in Women Is Improved by Long-term High Vegetable Intake Compared with the Average Western Diet. *J. Nutr.* **131**, 733–739 (2001).
 65. Cinquina, V. *et al.* Life-long epigenetic programming of cortical architecture by maternal ‘Western’ diet during pregnancy. *Mol. Psychiatry* **25**, 22–36 (2020).
 66. Pound, L. D., Comstock, S. M. & Grove, K. L. Consumption of a Western-style diet during pregnancy impairs offspring islet vascularization in a Japanese macaque model. *Am. J. Physiol. Metab.* **307**, E115–E123 (2014).
 67. Ray, J. G., Vermeulen, M., Schull, M., McDonald, S. & Redelmeier, D. A. *Metabolic Syndrome and the Risk of Placental Dysfunction. Journal of Obstetrics and Gynaecology Canada* **27**, (2005).
 68. Taylor, P. D. *et al.* Impaired glucose homeostasis and mitochondrial abnormalities in offspring of rats fed a fat-rich diet in pregnancy. *Am. J. Physiol. - Regul. Integr. Comp. Physiol.* **288**, (2005).
 69. Cerf, M. E. *et al.* Islet cell response in the neonatal rat after exposure to a high-fat diet during pregnancy. *Am. J. Physiol. Integr. Comp. Physiol.* **288**, R1122–R1128 (2005).
 70. Grassi, A. E. & Giuliano, M. A. The Neonate With Macrosomia. *Clin. Obstet. Gynecol.* **43**, 340–348 (2000).
 71. Statistics Canada. Live births and fetal deaths (stillbirths), by type of birth (single or multiple). (2021). Available at: <https://www150.statcan.gc.ca/t1/tb11/en/tv.action?pid=1310042801>.
 72. Baschat, A. A. & Hecher, K. Fetal Growth Restriction due to Placental Disease. *Semin. Perinatol.* **28**, 67–80 (2004).
 73. Bendix, I., Miller, S. L. & Winterhager, E. Editorial: Causes and Consequences of Intrauterine Growth Restriction. *Front. Endocrinol. (Lausanne)*. **11**, 205 (2020).
 74. Bobrow, C. S. & Soothill, P. W. Causes and consequences of fetal acidosis.

doi:10.1136/fn.80.3.F246

75. Barker, D. J. P. The fetal and infant origins of adult disease. *British Medical Journal* **301**, 1111 (1990).
76. Inadera, H. Developmental origins of obesity and type 2 diabetes: Molecular aspects and role of chemicals. *Environmental Health and Preventive Medicine* **18**, 185–197 (2013).
77. Barker, D. J. P. The origins of the developmental origins theory. *J. Intern. Med.* **261**, 412–417 (2007).
78. Almond, D. & Currie, J. Killing Me Softly: The Fetal Origins Hypothesis. doi:10.1257/jep.25.3.153
79. Oken, E. & Gillman, M. W. Fetal origins of obesity. *Obesity Research* **11**, 496–506 (2003).
80. Hales, C. N. & Barker, D. J. P. Type 2 (non-insulin-dependent) diabetes mellitus: the thrifty phenotype hypothesis. *Diabetologia* **35**, 595–601 (1992).
81. Hoffman, D. J., Reynolds, R. M. & Hardy, D. B. Developmental origins of health and disease: Current knowledge and potential mechanisms. *Nutr. Rev.* **75**, 951–970 (2017).
82. Shaheen, S. O., Sterne, J. A. C., Montgomery, S. M. & Azima, H. Birth weight, body mass index and asthma in young adults. *Thorax* **54**, 396–402 (1999).
83. Walker, C. L. & Ho, S. M. Developmental reprogramming of cancer susceptibility. *Nature Reviews Cancer* **12**, 479–486 (2012).
84. Suzuki, K. The developing world of DOHaD. in *Journal of Developmental Origins of Health and Disease* **9**, 266–269 (Cambridge University Press, 2018).
85. Eriksson, J. G. The fetal origins hypothesis—10 years on. *BMJ* **330**, 1096–1097 (2005).
86. Chatelain, P. Children born with intra-uterine growth retardation (IUGR) or small for gestational age (SGA): long term growth and metabolic consequences. *Endocr. Regul.* **34**, 33–36 (2000).
87. Yanney, M. & Marlow, N. Paediatric consequences of fetal growth restriction. *Semin. Fetal Neonatal Med.* **9**, 411–418 (2004).
88. van Wassenaer, A. Neurodevelopmental consequences of being born SGA. *Pediatr. Endocrinol. Rev.* **2**, 372–377 (2005).
89. DASHE, J. S., McINTIRE, D. D., LUCAS, M. J. & LEVENO, K. J. Effects of Symmetric and Asymmetric Fetal Growth on Pregnancy Outcomes. *Obstet. Gynecol.* **96**, (2000).
90. Lin, C.-C., Su, S.-J. & River, L. P. Comparison of associated high-risk factors and perinatal outcome between symmetric and asymmetric fetal intrauterine growth retardation. *Am. J. Obstet. Gynecol.* **164**, 1535–1542 (1991).
91. Miller, J., Turan, S. & Baschat, A. A. Fetal Growth Restriction. *Semin. Perinatol.* **32**, 274–280 (2008).
92. Rasmussen, K. M. The “Fetal Origins” Hypothesis: Challenges and Opportunities for Maternal and Child Nutrition. *Annu. Rev. Nutr.* **21**, 73–95 (2001).
93. Henriksen, T. The macrosomic fetus: a challenge in current obstetrics. *Acta Obstet. Gynecol. Scand.* **87**, 134–145 (2008).
94. Oolditch, I. M. & Kirkman, K. The large fetus: Management and outcome. *Obstet. Gynecol.* **52**, 26–30 (1978).
95. Giza, S. A. *et al.* The application of in utero magnetic resonance imaging in the study of the metabolic and cardiovascular consequences of the developmental origins of health and

- disease. *J. Dev. Orig. Health Dis.* 1–10 (2020). doi:DOI: 10.1017/S2040174420001154
96. Anderson, J. M. Increased brain weight/liver weight ratio as a necropsy sign of intrauterine undernutrition. *J. Clin. Pathol.* **25**, 867 LP – 871 (1972).
 97. Boito, S., Struijk, P. C., Ursem, N. T. C., Fedele, L. & Wladimiroff, J. W. Fetal brain/liver volume ratio and umbilical volume flow parameters relative to normal and abnormal human development. *Ultrasound Obstet. Gynecol.* **21**, 256–261 (2003).
 98. Fowden, A. L., Sferruzzi-Perri, A. N., Coan, P. M., Constancia, M. & Burton, G. J. Placental efficiency and adaptation: endocrine regulation. *J. Physiol.* **587**, 3459–3472 (2009).
 99. Haavaldsen, C., Samuelsen, S. O. & Eskild, A. Fetal death and placental weight/birthweight ratio: a population study. *Acta Obstet. Gynecol. Scand.* **92**, 583–590 (2013).
 100. Kim, H. S., Cho, S. H., Kwon, H. S., Sohn, I. S. & Hwang, H. S. The significance of placental ratios in pregnancies complicated by small for gestational age, preeclampsia, and gestational diabetes mellitus. *Obstet. Gynecol. Sci.* **57**, 358–366 (2014).
 101. Huxley, R., Neil, A. & Collins, R. Unravelling the fetal origins hypothesis: Is there really an inverse association between birthweight and subsequent blood pressure? *Lancet* **360**, 659–665 (2002).
 102. Nardoza, L. M. M. *et al.* Fetal growth restriction: current knowledge to the general Obs/Gyn. *Arch. Gynecol. Obstet.* **286**, 1–13 (2012).
 103. Godfrey, K. M. The role of the placenta in fetal programming—a review. *Placenta* **23**, S20–S27 (2002).
 104. Tarrade, A., Panchenko, P., Junien, C. & Gabory, A. Placental contribution to nutritional programming of health and diseases: epigenetics and sexual dimorphism. *J. Exp. Biol.* **218**, 50–58 (2015).
 105. Thornburg, K. L. *et al.* Biological features of placental programming. *Placenta* **48**, S47–S53 (2016).
 106. Bianchi, C. *et al.* The role of obesity and gestational diabetes on placental size and fetal oxygenation. *Placenta* **103**, 59–63 (2021).
 107. Lin, Y. J. *et al.* Maternal high-fat diet sex-specifically alters placental morphology and transcriptome in rats: Assessment by next-generation sequencing. *Placenta* **78**, 44–53 (2019).
 108. Gohir, W. *et al.* High-fat diet intake modulates maternal intestinal adaptations to pregnancy and results in placental hypoxia, as well as altered fetal gut barrier proteins and immune markers. *J. Physiol.* **597**, 3029–3051 (2019).
 109. Roos, S., Powell, T. L. & Jansson, T. Placental mTOR links maternal nutrient availability to fetal growth. *Biochemical Society Transactions* **37**, 295–298 (2009).
 110. Lager, S. *et al.* Diet-induced obesity in mice reduces placental efficiency and inhibits placental mTOR signaling. *Physiol. Rep.* **2**, e00242 (2014).
 111. Jones, H. N. *et al.* High-fat diet before and during pregnancy causes marked up-regulation of placental nutrient transport and fetal overgrowth in C57/BL6 mice. *FASEB J.* **23**, 271–278 (2009).
 112. Gallou-Kabani, C. *et al.* Sex- and Diet-Specific Changes of Imprinted Gene Expression and DNA Methylation in Mouse Placenta under a High-Fat Diet. *PLoS One* **5**, e14398

- (2010).
113. Thakali, K. M., Zhong, Y., Cleves, M., Andres, A. & Shankar, K. Associations between maternal body mass index and diet composition with placental DNA methylation at term. *Placenta* **93**, 74–82 (2020).
 114. Vickers, M. H., Clayton, Z. E., Yap, C. & Sloboda, D. M. Maternal fructose intake during pregnancy and lactation alters placental growth and leads to sex-specific changes in fetal and neonatal endocrine function. *Endocrinology* **152**, 1378–1387 (2011).
 115. Asghar, Z. A. *et al.* Maternal fructose drives placental uric acid production leading to adverse fetal outcomes. *Sci. Rep.* **6**, 1–11 (2016).
 116. Fernandez, M. L. & Volek, J. S. Guinea pigs: A suitable animal model to study lipoprotein metabolism, atherosclerosis and inflammation. *Nutrition and Metabolism* **3**, 1–6 (2006).
 117. Ye, P., Cheah, I. K. & Halliwell, B. High fat diets and pathology in the guinea pig. Atherosclerosis or liver damage? *Biochim. Biophys. Acta - Mol. Basis Dis.* **1832**, 355–364 (2013).
 118. deOgburn, R., Murillo, G. & Luz Fernandez, M. Guinea pigs as models for investigating non-alcoholic fatty liver disease. *Integr. Food, Nutr. Metab.* **3**, 309–313 (2016).
 119. Carter, A. M. Animal Models of Human Placentation – A Review. *Placenta* **28**, S41–S47 (2007).
 120. Morrison, J. L. *et al.* Guinea pig models for translation of the developmental origins of health and disease hypothesis into the clinic. *J. Physiol.* **596**, 5535–5569 (2018).
 121. Grigsby, P. L. Animal models to study placental development and function throughout normal and dysfunctional human pregnancy. in *Seminars in reproductive medicine* **34**, 11 (NIH Public Access, 2016).
 122. Kaufmann, P. Guinea Pig. in *Comparative placentation* (2004).
 123. Hore, P. J. *Nuclear magnetic resonance*. (Oxford University Press, USA, 2015).
 124. Siddiqui, S. *et al.* The Use of Hyperpolarized Carbon-13 Magnetic Resonance for Molecular Imaging. doi:10.1016/j.addr.2016.08.011
 125. Constantinides, C. *Magnetic resonance imaging: the basics*. (CRC press, 2016).
 126. McRobbie, D. W., Moore, E. A., Graves, M. J. & Prince, M. R. *MRI from Picture to Proton*. (Cambridge University Press, 2003).
 127. Plewes, D. B. & Kucharczyk, W. Physics of MRI: a primer. *J. Magn. Reson. imaging* **35**, 1038–1054 (2012).
 128. Brown, R. W., Cheng, Y.-C. N., Haacke, E. M., Thompson, M. R. & Venkatesan, R. *Magnetic Resonance Imaging: Physical Principles and Sequence Design*. (John Wiley & Sons, Inc., 2014).
 129. Eom, H. J. Faraday's Law of Induction. in *Primary Theory of Electromagnetics* 95–111 (Springer, 2013).
 130. Logothetis, N. K. & Wandell, B. A. Interpreting the BOLD signal. *Annu. Rev. Physiol.* **66**, 735–769 (2004).
 131. Chavhan, G. B., Babyn, P. S., Thomas, B., Shroff, M. M. & Mark Haacke, E. Principles, techniques, and applications of T2*-based MR imaging and its special applications. *Radiographics* **29**, 1433–1449 (2009).
 132. Hollas, J. M. *Modern spectroscopy*. (John Wiley & Sons, 2004).
 133. Alger, J. R. Magnetic Resonance Spectroscopy. in (ed. Squire, L. R. B. T.-E. of N.) 601–

- 607 (Academic Press, 2009). doi:<https://doi.org/10.1016/B978-008045046-9.00300-4>
134. Tognarelli, J. M. *et al.* Magnetic resonance spectroscopy: principles and techniques: lessons for clinicians. *J. Clin. Exp. Hepatol.* **5**, 320–328 (2015).
 135. Roberts, G. C. K. Nuclear magnetic resonance spectroscopy. *Adv. Protein Chem.* 447 (1970).
 136. Gallagher, T. A., Nemeth, A. J. & Hacein-Bey, L. An introduction to the Fourier transform: relationship to MRI. *Am. J. Roentgenol.* **190**, 1396–1405 (2008).
 137. van der Graaf, M. In vivo magnetic resonance spectroscopy: basic methodology and clinical applications. *Eur. Biophys. J.* **39**, 527–540 (2010).
 138. Johnson, B. *et al.* The use of magnetic resonance spectroscopy in the subacute evaluation of athletes recovering from single and multiple mild traumatic brain injury. *J. Neurotrauma* **29**, 2297–2304 (2012).
 139. Santos-Díaz, A. & Noseworthy, M. D. Phosphorus magnetic resonance spectroscopy and imaging (31P-MRS/MRSI) as a window to brain and muscle metabolism: a review of the methods. *Biomed. Signal Process. Control* **60**, 101967 (2020).
 140. Ma, J. Dixon techniques for water and fat imaging. *J. Magn. Reson. Imaging An Off. J. Int. Soc. Magn. Reson. Med.* **28**, 543–558 (2008).
 141. Dixon, W. T. Simple proton spectroscopic imaging. *Radiology* **153**, 189–94 (1984).
 142. Viallon, M. *et al.* Chemical-shift-encoded magnetic resonance imaging and spectroscopy to reveal immediate and long-term multi-organs composition changes of a 14-days periodic fasting intervention: a technological and case report. *Front. Nutr.* **6**, 5 (2019).
 143. Glover, G. H. Multipoint Dixon technique for water and fat proton and susceptibility imaging. *J. Magn. Reson. Imaging* **1**, 521–530 (1991).
 144. Reeder, S. B. *et al.* Iterative decomposition of water and fat with echo asymmetry and least-squares estimation (IDEAL): Application with fast spin-echo imaging. *Magn. Reson. Med.* **54**, 636–644 (2005).
 145. Yu, H. *et al.* Multiecho water-fat separation and simultaneous R estimation with multifrequency fat spectrum modeling. *Magn. Reson. Med. An Off. J. Int. Soc. Magn. Reson. Med.* **60**, 1122–1134 (2008).
 146. Peterson, P., Trinh, L. & Månsson, S. Quantitative 1H MRI and MRS of fatty acid composition. *Magn. Reson. Med.* **85**, 49–67 (2021).
 147. Hu, H. H., Smith Jr, D. L., Nayak, K. S., Goran, M. I. & Nagy, T. R. Identification of brown adipose tissue in mice with fat–water IDEAL-MRI. *J. Magn. Reson. Imaging An Off. J. Int. Soc. Magn. Reson. Med.* **31**, 1195–1202 (2010).
 148. Kühn, J. *et al.* Quantitative chemical shift-encoded MRI is an accurate method to quantify hepatic steatosis. *J. Magn. Reson. Imaging* **39**, 1494–1501 (2014).
 149. Reeder, S. B., Hu, H. H. & Sirlin, C. B. Proton density fat-fraction: a standardized MR-based biomarker of tissue fat concentration. *J. Magn. Reson. imaging JMRI* **36**, 1011 (2012).
 150. Yu, H. *et al.* Multiecho reconstruction for simultaneous water-fat decomposition and T2* estimation. *J. Magn. Reson. Imaging An Off. J. Int. Soc. Magn. Reson. Med.* **26**, 1153–1161 (2007).
 151. Tang, A. *et al.* Nonalcoholic fatty liver disease: MR imaging of liver proton density fat fraction to assess hepatic steatosis. *Radiology* **267**, 422–431 (2013).

152. Kühn, J.-P. *et al.* Proton-density fat fraction and simultaneous R2* estimation as an MRI tool for assessment of osteoporosis. *Eur. Radiol.* **23**, 3432–3439 (2013).
153. Colgan, T. J., Hernando, D., Sharma, S. D. & Reeder, S. B. The effects of concomitant gradients on chemical shift encoded MRI. *Magn. Reson. Med.* **78**, 730–738 (2017).
154. van Heeswijk, R. B. *et al.* Chemical shift encoding (CSE) for sensitive fluorine-19 MRI of perfluorocarbons with complex spectra. *Magn. Reson. Med.* **79**, 2724–2730 (2018).
155. Wiens, C. N., Friesen-Waldner, L. J., Wade, T. P., Sinclair, K. J. & McKenzie, C. A. Chemical shift encoded imaging of hyperpolarized ¹³C pyruvate. *Magn. Reson. Med.* **74**, 1682–1689 (2015).
156. Bammer, R. Basic principles of diffusion-weighted imaging. *Eur. J. Radiol.* **45**, 169–184 (2003).
157. Le Bihan, D. What can we see with IVIM MRI? *Neuroimage* **187**, 56–67 (2019).
158. Hagmann, P. *et al.* Understanding diffusion MR imaging techniques: From scalar diffusion-weighted imaging to diffusion tensor imaging and beyond. *Radiographics* **26**, (2006).
159. Baliyan, V., Das, C. J., Sharma, R. & Gupta, A. K. Diffusion weighted imaging: Technique and applications. *World J. Radiol.* **8**, 785 (2016).
160. Carr, H. Y. & Purcell, E. M. Effects of diffusion on free precession in nuclear magnetic resonance experiments. *Phys. Rev.* **94**, 630 (1954).
161. Iima, M. & Le Bihan, D. Clinical intravoxel incoherent motion and diffusion MR imaging: past, present, and future. *Radiology* **278**, 13–32 (2016).
162. Le Bihan, D. Diffusion MRI: what water tells us about the brain. *EMBO Mol. Med.* **6**, 569–573 (2014).
163. Aughwane, R. *et al.* Placental MRI and its application to fetal intervention. (2019). doi:10.1002/pd.5526
164. Koh, D.-M., Collins, D. J. & Orton, M. R. Intravoxel Incoherent Motion in Body Diffusion-Weighted MRI: Reality and Challenges. *Am. J. Roentgenol.* **196**, 1351–1361 (2011).
165. Le Bihan, D. & Breton, E. *Separation of Diffusion and Perfusion in Intravoxel Incoherent Motion MR Imaging.*
166. Turner, R. *et al.* Echo-planar imaging of intravoxel incoherent motion. *Radiology* **177**, 407–414 (1990).
167. Sørensen, A., Hutter, J., Seed, M., Grant, P. E. & Gowland, P. T2*-weighted placental MRI: basic research tool or emerging clinical test for placental dysfunction? *Ultrasound Obstet. Gynecol.* **55**, 293–302 (2020).
168. Pauling, L. & Coryell, C. D. The magnetic properties and structure of hemoglobin, oxyhemoglobin and carbonmonoxyhemoglobin. *Proc. Natl. Acad. Sci.* **22**, 210–216 (1936).
169. Li, D., Wang, Y. & Waight, D. J. Blood oxygen saturation assessment in vivo using T2* estimation. *Magn. Reson. Med.* **39**, 685–690 (1998).
170. Christen, T. *et al.* Is T2* enough to assess oxygenation? Quantitative blood oxygen level-dependent analysis in brain tumor. *Radiology* **262**, 495–502 (2012).
171. Abaci Turk, E. *et al.* Placental MRI: developing accurate quantitative measures of oxygenation. *Top. Magn. Reson. Imaging* **28**, 285–297 (2019).

172. Sørensen, A. *et al.* Changes in human placental oxygenation during maternal hyperoxia estimated by blood oxygen level-dependent magnetic resonance imaging (BOLD MRI). *Ultrasound Obstet. Gynecol.* **42**, 310–314 (2013).
173. Chen, B. H. *et al.* BOLD cardiac MRI for differentiating reversible and irreversible myocardial damage in ST segment elevation myocardial infarction. *Eur. Radiol.* **29**, 951–962 (2019).
174. Christen, T. *et al.* Tissue oxygen saturation mapping with magnetic resonance imaging. *J. Cereb. Blood Flow Metab.* **34**, 1550–1557 (2014).
175. Kurhanewicz, J. *et al.* Analysis of cancer metabolism by imaging hyperpolarized nuclei: Prospects for translation to clinical research. *Neoplasia* **13**, 81–97 (2011).
176. Kubala, E. *et al.* Hyperpolarized¹³C metabolic magnetic resonance spectroscopy and imaging. *J. Vis. Exp.* **2016**, 1–16 (2016).
177. Wang, Z. J. *et al.* Hyperpolarized ¹³ C MRI: State of the Art and Future Directions. *Radiology* **291**, 273–284 (2019).
178. Nikolaou, P., Goodson, B. M. & Chekmenev, E. Y. NMR Hyperpolarization Techniques for Biomedicine. *Chem. – A Eur. J.* **21**, 3156–3166 (2015).
179. Walker, T. G. & Happer, W. Spin-exchange optical pumping of noble-gas nuclei. *RMP Colloq.* (1997).
180. Eisenschmid, T. C. *et al.* Para hydrogen induced polarization in hydrogenation reactions. *J. Am. Chem. Soc.* **109**, 8089–8091 (1987).
181. Atkinson, K. D. *et al.* Spontaneous Transfer of Parahydrogen Derived Spin Order to Pyridine at Low Magnetic Field. doi:10.1021/ja903601p
182. Golman, K. *et al.* Parahydrogen-induced polarization in imaging: Subsecond ¹³ C angiography. *Magn. Reson. Med.* **46**, 1–5 (2001).
183. Bogner, W., Otazo, R. & Henning, A. Accelerated MR spectroscopic imaging—a review of current and emerging techniques. *NMR Biomed.* (2020). doi:10.1002/nbm.4314
184. Ardenkjaer-Larsen, J. H. *et al.* Increase in signal-to-noise ratio of > 10,000 times in liquid-state NMR. *Proc. Natl. Acad. Sci. U. S. A.* **100**, 10158–63 (2003).
185. Miloushev, V. Z., Keshari, K. R. & Holodny, A. I. Hyperpolarization MRI preclinical models and potential applications in neuroradiology. *Topics in Magnetic Resonance Imaging* **25**, 31–37 (2016).
186. Meier, S., Jensen, P. R., Karlsson, M. & Lerche, M. H. Hyperpolarized NMR probes for biological assays. *Sensors (Basel)*. **14**, 1576–1597 (2014).
187. Cherry, S. R. & Dahlbom, M. PET: physics, instrumentation, and scanners. in *PET* 1–117 (Springer, 2006).
188. Kurhanewicz, J. *et al.* Hyperpolarized ¹³C MRI: Path to Clinical Translation in Oncology. *Neoplasia* **21**, 1–16 (2019).
189. Overhauser, A. W. Polarization of nuclei in metals. *Phys. Rev.* **92**, 411 (1953).
190. Ardenkjaer-Larsen, J. H. *et al.* Dynamic nuclear polarization polarizer for sterile use intent. *NMR Biomed.* **24**, 927–932 (2011).
191. Nelson, S. J. *et al.* Metabolic imaging of patients with prostate cancer using hyperpolarized [1-¹³C]pyruvate. *Sci. Transl. Med.* **5**, 198ra108 (2013).
192. Kamide, K. *Cellulose and cellulose derivatives.* (Elsevier, 2005).
193. Zangari, J., Petrelli, F., Maillot, B. & Martinou, J.-C. The Multifaceted Pyruvate

- Metabolism: Role of the Mitochondrial Pyruvate Carrier. *Biomolecules* **10**, 1068 (2020).
194. Melkonian, E. A. & Schury, M. P. Biochemistry, anaerobic glycolysis. (2019).
 195. Chen, A. P. *et al.* Simultaneous investigation of cardiac pyruvate dehydrogenase flux, Krebs cycle metabolism and pH, using hyperpolarized [1,2-¹³C₂]pyruvate *in vivo*. *NMR Biomed.* **25**, 305–311 (2012).
 196. Chung, B. T. *et al.* First hyperpolarized [2-¹³C]pyruvate MR studies of human brain metabolism. *J. Magn. Reson.* **309**, 106617 (2019).
 197. Akram, M. Citric Acid Cycle and Role of its Intermediates in Metabolism. *Cell Biochem. Biophys.* **68**, 475–478 (2014).
 198. Hu, S. *et al.* Use of hyperpolarized [1-¹³C]pyruvate and [2-¹³C]pyruvate to probe the effects of the anticancer agent dichloroacetate on mitochondrial metabolism *in vivo* in the normal rat. *Magn. Reson. Imaging* **30**, 1367–1372 (2012).
 199. Hu, S. *et al.* *In vivo* measurement of normal rat intracellular pyruvate and lactate levels after injection of hyperpolarized [1-¹³C]alanine. *Magn. Reson. Imaging* **29**, 1035–1040 (2011).
 200. Khagai, O. *et al.* Apparent rate constant mapping using hyperpolarized [1-¹³C]pyruvate. (2014). doi:10.1002/nbm.3174
 201. Daniels, C. J. *et al.* A comparison of quantitative methods for clinical imaging with hyperpolarized¹³C-pyruvate. *NMR Biomed.* **29**, 387–399 (2016).
 202. Vander Heiden, M. G., Cantley, L. C. & Thompson, C. B. *Understanding the Warburg Effect: The Metabolic Requirements of Cell Proliferation.*
 203. Lupo, J. M. *et al.* Analysis of hyperpolarized dynamic ¹³C lactate imaging in a transgenic mouse model of prostate cancer. *Magn. Reson. Imaging* **28**, 153–162 (2010).
 204. DeVience, S. J. *et al.* Metabolic imaging of energy metabolism in traumatic brain injury using hyperpolarized [1-¹³C]pyruvate. *Sci. Rep.* **7**, 1907 (2017).
 205. Moon, C. M. *et al.* Metabolic biomarkers for non-alcoholic fatty liver disease induced by high-fat diet: *In vivo* magnetic resonance spectroscopy of hyperpolarized [1-¹³C] pyruvate. *Biochem. Biophys. Res. Commun.* **482**, 112–119 (2017).
 206. Friesen-Waldner, L. J. *et al.* Hyperpolarized [1-¹³C]Pyruvate MRI for Noninvasive Examination of Placental Metabolism and Nutrient Transport: A Feasibility Study in Pregnant Guinea Pigs. *J. MAGN. Reson. IMAGING* **43**, 750–755 (2016).
 207. Hall, M. M., Rajasekaran, S., Thomsen, T. W. & Peterson, A. R. Lactate: Friend or Foe. *PM&R* **8**, S8–S15 (2016).
 208. Xie, B., Waters, M. J. & Schirra, H. J. Investigating Potential Mechanisms of Obesity by Metabolomics. *J. Biomed. Biotechnol.* **2012**, (2012).
 209. Caussy, C., Reeder, S. B., Sirlin, C. B. & Loomba, R. Noninvasive, Quantitative Assessment of Liver Fat by MRI-PDFF as an Endpoint in NASH Trials. *Hepatology* **68**, 763–772 (2018).
 210. Lee, P. *et al.* *In Vivo* hyperpolarized carbon-13 magnetic resonance spectroscopy reveals increased pyruvate carboxylase flux in an insulin-resistant mouse model. *Hepatology* **57**, 515–524 (2013).
 211. Sarr, O. *et al.* Western diet consumption through early life induces microvesicular hepatic steatosis in association with an altered metabolome in low birth weight Guinea pigs. *J. Nutr. Biochem.* **67**, 219–233 (2019).

212. Leary, S. *et al.* *AVMA Guidelines for the Euthanasia of Animals*. (2020).
213. Gomez-Pinilla, P. J. *et al.* Effect of Melatonin on Age Associated Changes in Guinea Pig Bladder Function. *J. Urol.* **177**, 1558–1561 (2007).
214. Mirakhur, R. K. & Dundee, J. W. Glycopyrrolate: pharmacology and clinical use. *Anaesthesia* **38**, 1195–1204 (1983).
215. Fedorov, A. *et al.* 3D Slicer as an image computing platform for the Quantitative Imaging Network. *Magn. Reson. Imaging* **30**, 1323–1341 (2012).
216. Folch, J., Lees, M. & Sloane, G. H. A simple method for the isolation and purification of total lipides from animal tissues. *J. Biol. Chem.* **226**, 497–509 (1956).
217. Assini, J. M., Mulvihill, E. E. & Huff, M. W. Citrus flavonoids and lipid metabolism. *Curr. Opin. Lipidol.* **24**, 34–40 (2013).
218. Hariri, N. & Thibault, L. High-fat diet-induced obesity in animal models. *Nutr. Res. Rev.* **23**, 270–299 (2010).
219. Hoy, A. M. *et al.* Non-invasive assessment of liver disease in rats using multiparametric magnetic resonance imaging: a feasibility study. *Biol. Open* **7**, 1–7 (2018).
220. Ye, Q. *et al.* Global prevalence, incidence, and outcomes of non-obese or lean non-alcoholic fatty liver disease: a systematic review and meta-analysis. *Lancet Gastroenterol. Hepatol.* **5**, 739–752 (2020).
221. Wolf, D. C. Evaluation of the Size, Shape, and Consistency of the Liver. *Clin. Methods Hist. Phys. Lab. Exam.* **62**, 478–481 (1990).
222. Szczepaniak, L. S. *et al.* Magnetic resonance spectroscopy to measure hepatic triglyceride content: Prevalence of hepatic steatosis in the general population. *Am. J. Physiol. - Endocrinol. Metab.* **288**, 462–468 (2005).
223. Unger, R. H. Lipid overload and overflow: Metabolic trauma and the metabolic syndrome. *Trends Endocrinol. Metab.* **14**, 398–403 (2003).
224. Giboney, P. T. *Mildly Elevated Liver Transaminase Levels in the Asymptomatic Patient - American Family Physician.* *American Family Physician* **71**, (2005).
225. Oettl, K. *et al.* Oxidative damage of albumin in advanced liver disease. *Biochim. Biophys. Acta - Mol. Basis Dis.* **1782**, 469–473 (2008).
226. Leveille, G. & Associates, L. Effect of Dietary Fructose on Fatty Acid Synthesis in Adipose Tissue and Liver of the Rat. *Artic. J. Nutr.* (1972). doi:10.1093/jn/102.3.337
227. Bar-On, H. & Stein, Y. Effect of glucose and fructose administration on lipid metabolism in the rat. *J. Nutr.* **94**, 95–105 (1968).
228. De Bandt, J.-P., Jegatheesan, P. & Tennoune-El-Hafaia, N. Muscle Loss in Chronic Liver Diseases: The Example of Nonalcoholic Liver Disease. *Nutrients* **10**, 1195 (2018).
229. Cambri, L. T., Ghezzi, A. C., Ribeiro, C., Dalia, R. A. & Rostom de Mello, M. A. Recovery of rat growth and lipid profiles in adult rats subjected to fetal protein malnutrition with a fructose-rich diet. *Nutr. Res.* **30**, 156–162 (2010).
230. Chen, C.-Y. O. *et al.* Fructose and saturated fats predispose hyperinsulinemia in lean male rat offspring. *Eur J Nutr* **49**, 337–343 (2010).
231. Consoli, A., Nurjhan, N., Reilly, J. J., Bier, D. M. & Gerich, J. E. Mechanism of increased gluconeogenesis in noninsulin-dependent diabetes mellitus. Role of alterations in systemic, hepatic, and muscle lactate and alanine metabolism. *J. Clin. Invest.* **86**, 2038–2045 (1990).

232. Shangraw, R. E., Rabkin, J. M. & Lopaschuk, G. D. *Hepatic pyruvate dehydrogenase activity in humans: effect of cirrhosis, transplantation, and dichloroacetate*. (1998).
233. Brunt, E. M. *et al.* Portal chronic inflammation in nonalcoholic fatty liver disease (NAFLD): A histologic marker of advanced NAFLD - Clinicopathologic correlations from the nonalcoholic steatohepatitis clinical research network. *Hepatology* **49**, 809–820 (2009).
234. Gehrke, N. *et al.* Voluntary exercise in mice fed an obesogenic diet alters the hepatic immune phenotype and improves metabolic parameters – an animal model of life style intervention in NAFLD. *Sci. Rep.* **9**, 1–13 (2019).
235. Wren-Dail, M. A. *et al.* Effect of isoflurane anesthesia on circadian metabolism and physiology in rats. *Comp. Med.* **67**, 138–146 (2017).
236. Siauve, N. *et al.* Functional imaging of the human placenta with magnetic resonance. *Am. J. Obstet. Gynecol.* **213**, S103–S114 (2015).
237. Dekan, S., Linduska, N., Kasprian, G. & Prayer, D. MRI of the placenta – a short review. *Wiener Medizinische Wochenschrift* **162**, 225–228 (2012).
238. Avni, R., Neeman, M. & Garbow, J. R. Functional MRI of the placenta – From rodents to humans. *Placenta* **36**, 615–622 (2015).
239. Hurd, R. E., Yen, Y. F., Chen, A. & Ardenkjaer-Larsen, J. H. Hyperpolarized ¹³C metabolic imaging using dissolution dynamic nuclear polarization. *J. Magn. Reson. Imaging* **36**, 1314–1328 (2012).
240. Atherton, H. J. *et al.* Validation of the in vivo assessment of pyruvate dehydrogenase activity using hyperpolarised ¹³C MRS. *NMR Biomed.* (2011). doi:10.1002/nbm.1573
241. Zhao, L. *et al.* COMMUNICATIONS Gradient-Echo Imaging Considerations for Hyperpolarized ¹²⁹Xe MR. *JOURNAL OF MAGNETIC RESONANCE, Series B* **113**, (1996).
242. Maidens, J., Gordon, J. W., Arcak, M. & Larson, P. E. Z. Optimizing Flip Angles for Metabolic Rate Estimation in Hyperpolarized Carbon-13 MRI. *IEEE Trans. Med. Imaging* (2016). doi:10.1109/TMI.2016.2574240
243. Larson, P. E. Z. *et al.* Multiband excitation pulses for hyperpolarized¹³C dynamic chemical-shift imaging. *J. Magn. Reson.* **194**, 121–127 (2008).
244. Nagashima, K. Optimum pulse flip angles for multi-scan acquisition of hyperpolarized NMR and MRI. *J. Magn. Reson.* (2008). doi:10.1016/j.jmr.2007.10.011
245. Xing, Y., Reed, G. D., Pauly, J. M., Kerr, A. B. & Larson, P. E. Z. Optimal variable flip angle schemes for dynamic acquisition of exchanging hyperpolarized substrates. *J. Magn. Reson.* (2013). doi:10.1016/j.jmr.2013.06.003
246. Cunningham, C. H. *et al.* Pulse sequence for dynamic volumetric imaging of hyperpolarized metabolic products. *J. Magn. Reson.* **193**, 139–146 (2008).
247. Smith, L. *et al.* Optimizing signal-to-noise ratio for hyperpolarized carbon-13 magnetic resonance imaging using a hybrid flip angle scheme. in *Proceedings of the 26th International Society of Magnetic Resonance in Medicine Annual Scientific Meeting & Exhibition 1* (2018).
248. Yen, Y.-F. *et al.* T(2) relaxation times of (¹³C) metabolites in a rat hepatocellular carcinoma model measured in vivo using (¹³C)-MRS of hyperpolarized [1-(¹³C)]pyruvate. *NMR Biomed.* **23**, 414–23 (2010).

249. Menichetti, L. *et al.* Assessment of real-time myocardial uptake and enzymatic conversion of hyperpolarized [1-¹³C]pyruvate in pigs using slice selective magnetic resonance spectroscopy. *Contrast Media Mol. Imaging* **7**, 85–94 (2012).
250. Lim, H., Thind, K., Martinez-Santesteban, F. M. & Scholl, T. J. Construction and evaluation of a switch-tuned ¹³C - ¹H birdcage radiofrequency coil for imaging the metabolism of hyperpolarized ¹³C-enriched compounds. *J. Magn. Reson. Imaging* **40**, 1082–1090 (2014).
251. Moore, M. & Nelson-Piercy, C. Pregnancy and the liver. *Br. J. Hosp. Med.* **72**, (2011).
252. Westbrook, R. H., Dusheiko, G. & Williamson, C. Pregnancy and liver disease. *Journal of Hepatology* **64**, 933–945 (2016).
253. Santyr, G. E., Lam, W. W. & Ouriadov, A. Rapid and Efficient Mapping of Regional Ventilation in the Rat Lung Using Hyperpolarized ³He with Flip Angle Variation for Offset of RF and Relaxation (FAVOR). *Magn Reson Med* **59**, 1304–1310 (2008).
254. Yen, Y.-F. *et al.* Imaging considerations for in vivo ¹³C metabolic mapping using hyperpolarized ¹³C-pyruvate. *Magn. Reson. Med.* **62**, 1–10 (2009).
255. Maidens, J., Gordon, J. W., Arcak, M. & Larson, P. E. Z. Optimizing Flip Angles for Metabolic Rate Estimation in Hyperpolarized Carbon-13 MRI. *IEEE Trans. Med. Imaging* **35**, 2403–2412 (2016).
256. Baschat, A. A. *et al.* Predictors of Neonatal Outcome in Early- Onset Placental Dysfunction. *Obstet. Gynecol.* **109**, 253–261 (2007).
257. Ghosh, G. & Gudmundsson, S. Uterine and umbilical artery Doppler are comparable in predicting perinatal outcome of growth-restricted fetuses. *BJOG An Int. J. Obstet. Gynaecol.* **116**, 424–430 (2009).
258. Cahill, L. S. *et al.* Wave reflections in the umbilical artery measured by Doppler ultrasound as a novel predictor of placental pathology. *EBioMedicine* **67**, 103326 (2021).
259. Murphy, D. J., Aghayev, A. & Steigner, M. L. Vascular CT and MRI: a practical guide to imaging protocols. *Insights Imaging* **9**, 215–236 (2018).
260. Mervak, B. M. *et al.* MRI in pregnancy: Indications and practical considerations. *J. Magn. Reson. Imaging* **49**, 621–631 (2019).
261. Sohlberg, S. *et al.* Placental perfusion in normal pregnancy and early and late preeclampsia: A magnetic resonance imaging study. *Placenta* **35**, 202–206 (2014).
262. Stuart, T. J. *et al.* Diet-induced obesity alters the maternal metabolome and early placenta transcriptome and decreases placenta vascularity in the mouse†. *Biol. Reprod.* **98**, 795–809 (2018).
263. Son, J. S. *et al.* Exercise prevents the adverse effects of maternal obesity on placental vascularization and fetal growth. *Authors. J. Physiol. C* **597**, 3333–3347 (2019).
264. Gustafsson, O., Montelius, M., Starck, G. & Ljungberg, M. Impact of prior distributions and central tendency measures on Bayesian intravoxel incoherent motion model fitting. *Magn. Reson. Med.* **79**, 1674–1683 (2018).
265. Jalnefjord, O. *et al.* Comparison of methods for estimation of the intravoxel incoherent motion (IVIM) diffusion coefficient (D) and perfusion fraction (f). *Magn. Reson. Mater. Physics, Biol. Med.* **31**, 715–723 (2018).
266. Lafeber, H. N., Rolph, T. P. & Jones, C. T. Studies on the growth of the fetal guinea pig. The effects of ligation of the uterine artery on organ growth and development. *J. Dev.*

- Physiol.* **6**, 441–459 (1984).
267. Pardi, G. & Cetin, I. Human fetal growth and organ development: 50 years of discoveries. *Am. J. Obstet. Gynecol.* **194**, 1088–1099 (2006).
 268. Ouyang, F. *et al.* Maternal BMI, gestational diabetes, and weight gain in relation to childhood obesity: the mediation effect of placental weight. *Obesity* **24**, 938–946 (2016).
 269. Berglund, S. K. *et al.* Maternal, fetal and perinatal alterations associated with obesity, overweight and gestational diabetes: an observational cohort study (PREOBE). *BMC Public Health* **16**, 1–12 (2016).
 270. Mando, C. *et al.* Sex specific adaptations in placental biometry of overweight and obese women. *Placenta* **38**, 1–7 (2016).
 271. Hutter, J. *et al.* Multi-modal functional MRI to explore placental function over gestation. *Magn. Reson. Med.* **81**, 1191–1204 (2019).
 272. Soothill, P. W., Nicolaides, K. H., Rodeck, C. H. & Campbell, S. Effect of gestational age on fetal and intervillous blood gas and acid-base values in human pregnancy. *Fetal Diagn. Ther.* **1**, 168–175 (1986).
 273. Ingram, E., Morris, D., Naish, J., Myers, J. & Johnstone, E. MR imaging measurements of altered placental oxygenation in pregnancies complicated by fetal growth restriction. *Radiology* **285**, 953–960 (2017).
 274. Huen, I. *et al.* R1 and R2* changes in the human placenta in response to maternal oxygen challenge. *Magn. Reson. Med.* **70**, 1427–1433 (2013).
 275. Wright, C. *et al.* Magnetic resonance imaging relaxation time measurements of the placenta at 1.5 T. *Placenta* **32**, 1010–1015 (2011).
 276. Sinding, M. *et al.* Placental magnetic resonance imaging T2* measurements in normal pregnancies and in those complicated by fetal growth restriction. *Ultrasound Obstet. Gynecol.* **47**, 748–754 (2016).
 277. Hutter, J. *et al.* T2* relaxometry to characterize normal placental development over gestation in-vivo at 3T. *Wellcome Open Res.* **4**, 166 (2019).
 278. Hayes, E. K. *et al.* Adverse fetal and neonatal outcomes associated with a life-long high fat diet: role of altered development of the placental vasculature. *PLoS One* **7**, e33370 (2012).
 279. Burton, G. J. & Fowden, A. L. The placenta: a multifaceted, transient organ. *Phil. Trans. R. Soc. B* **370**, 20140066 (2015).
 280. Slator, P. J. *et al.* Combined diffusion-relaxometry MRI to identify dysfunction in the human placenta. *Magn. Reson. Med.* **82**, 95–106 (2019).
 281. Manganaro, L. *et al.* MRI and DWI: feasibility of DWI and ADC maps in the evaluation of placental changes during gestation. *Prenat. Diagn.* **30**, 1178–1184 (2010).
 282. Jakab, A. *et al.* Microvascular perfusion of the placenta, developing fetal liver, and lungs assessed with intravoxel incoherent motion imaging. *J. Magn. Reson. Imaging* **48**, 214–225 (2018).
 283. Bacon, B. J. *et al.* Placental anatomy and diffusing capacity in guinea pigs following long-term maternal hypoxia. *Placenta* **5**, 475–487 (1984).
 284. Burton, G. J., Reshetnikova, O. S., Milovanov, A. P. & Teleshova, O. V. Stereological evaluation of vascular adaptations in human placental villi to differing forms of hypoxic stress. *Placenta* **17**, 49–55 (1996).

285. Bairagi, S. *et al.* Maternal environment and placental vascularization in small ruminants. *Theriogenology* **86**, 288–305 (2016).
286. Tudisco, L. *et al.* Epigenetic control of hypoxia inducible factor-1 α -dependent expression of placental growth factor in hypoxic conditions. *Epigenetics* **9**, 600–610 (2014).
287. Tudisco, L., Orlandi, A., Tarallo, V. & De Falco, S. Hypoxia activates placental growth factor expression in lymphatic endothelial cells. *Oncotarget* **8**, 32873 (2017).
288. Odorisio, T. *et al.* Mice overexpressing placenta growth factor exhibit increased vascularization and vessel permeability. *J. Cell Sci.* **115**, (2002).
289. Osol, G. *et al.* Placental growth factor is a potent vasodilator of rat and human resistance arteries. *Am. J. Physiol. Heart Circ. Physiol.* **294**, H1381-7 (2008).
290. Szukiewicz, D., Szewczyk, G., Watroba, M., Kurowska, E. & Maslinski, S. Isolated placental vessel response to vascular endothelial growth factor and placenta growth factor in normal and growth-restricted pregnancy. *Gynecol. Obstet. Invest.* **59**, 102–107 (2005).
291. Nye, G. A. *et al.* Human placental oxygenation in late gestation: experimental and theoretical approaches. *J. Physiol.* **596**, 5523–5534 (2018).
292. Javor, D. *et al.* In vivo assessment of putative functional placental tissue volume in placental intrauterine growth restriction (IUGR) in human fetuses using diffusion tensor magnetic resonance imaging. *Placenta* **34**, 676–680 (2013).
293. Clapp, J. F. Influence of Endurance Exercise and Diet on Human Placental Development and Fetal Growth. *Placenta* **27**, 527–534 (2006).
294. Fernandez-Twinn, D. S. *et al.* Exercise rescues obese mothers' insulin sensitivity, placental hypoxia and male offspring insulin sensitivity. *Sci. Rep.* **7**, 1–11 (2017).
295. Empey, M.-E. E. T. Quantifying Mid-pregnancy Placental Metabolism in Guinea Pigs Fed a Lifelong Western Diet. (2020).
296. Suzuki, T., Shinjo, S., Arai, T., Kanai, M. & Goda, N. Hypoxia and fatty liver. *World J. Gastroenterol. WJG* **20**, 15087 (2014).
297. Scholz, D. J. *et al.* Quantified pH Imaging with Hyperpolarized ¹³C-Bicarbonate. doi:10.1002/mrm.25357
298. Nardi-Schreiber, A. *et al.* Biochemical phosphates observed using hyperpolarized³¹P in physiological aqueous solutions. *Nat. Commun.* **8**, 1–7 (2017).
299. Tveden-Nyborg, P. *et al.* Diet-induced dyslipidemia leads to nonalcoholic fatty liver disease and oxidative stress in guinea pigs. *Transl. Res.* **168**, 146–160 (2016).
300. Vaeggemose, M., F Schulte, R. & Laustsen, C. Comprehensive Literature Review of Hyperpolarized Carbon-13 MRI: The Road to Clinical Application. *Metabolites* **11**, 219 (2021).
301. Moon, C. M. *et al.* Metabolic Changes in Different Stages of Liver Fibrosis: In vivo Hyperpolarized ¹³C MR Spectroscopy and Metabolic Imaging. *Mol. Imaging Biol.* **21**, 842–851 (2019).
302. Bonel, H. M. *et al.* Diffusion-weighted MR imaging of the placenta in fetuses with placental insufficiency. *Radiology* **257**, 810–819 (2010).
303. Slator, P. J. *et al.* Placenta microstructure and microcirculation imaging with diffusion MRI. *Magn. Reson. Med.* **80**, 756–766 (2018).

Appendices

Appendix A: Ethics Approvals

AUP Number: 2010-229
PI Name: Regnault, Timothy
AUP Title: In Utero Origins Of Adult Insulin Resistance
Approval Date: 09/08/2014

Official Notice of Animal Use Subcommittee (AUS) Approval: Your new Animal Use Protocol (AUP) entitled "In Utero Origins Of Adult Insulin Resistance" has been APPROVED by the Animal Use Subcommittee of the University Council on Animal Care. This approval, although valid for four years, and is subject to annual Protocol Renewal.2010-229::5

1. This AUP number must be indicated when ordering animals for this project.
2. Animals for other projects may not be ordered under this AUP number.
3. Purchases of animals other than through this system must be cleared through the ACVS office. Health certificates will be required.

The holder of this Animal Use Protocol is responsible to ensure that all associated safety components (biosafety, radiation safety, general laboratory safety) comply with institutional safety standards and have received all necessary approvals. Please consult directly with your institutional safety officers.

Submitted by: Copeman, Laura
 on behalf of the Animal Use Subcommittee
 University Council on Animal Care



The University of Western Ontario
 Animal Use Subcommittee / University Council on Animal Care
 Health Sciences Centre, • London, Ontario • CANADA – N6A 5C1
 PH: 519-661-2111 ext. 86768 • FL 519-661-2028
 Email: auspc@uwo.ca • <http://www.uwo.ca/animal/website/>



AUP Number: 2015-063
PI Name: Regnault, Timothy
AUP Title: Hyperpolarized 13c Mri Of Placental Metabolic Abnormalities Resulting From The Western Diet
Approval Date: 01/22/2016

Official Notice of Animal Use Subcommittee (AUS) Approval: Your new Animal Use Protocol (AUP) entitled "Hyperpolarized 13c Mri Of Placental Metabolic Abnormalities Resulting From The Western Diet" has been APPROVED by the Animal Use Subcommittee of the University Council on Animal Care. This approval, although valid for four years, and is subject to annual Protocol Renewal.2015-063::1

1. This AUP number must be indicated when ordering animals for this project.
2. Animals for other projects may not be ordered under this AUP number.
3. Purchases of animals other than through this system must be cleared through the ACVS office. Health certificates will be required.

The holder of this Animal Use Protocol is responsible to ensure that all associated safety components (biosafety, radiation safety, general laboratory safety) comply with institutional safety standards and have received all necessary approvals. Please consult directly with your institutional safety officers.

Submitted by: Copeman, Laura
 on behalf of the Animal Use Subcommittee
 University Council on Animal Care



The University of Western Ontario
 Animal Use Subcommittee / University Council on Animal Care
 Health Sciences Centre, • London, Ontario • CANADA – N6A 5C1
 PH: 519-661-2111 ext. 86768 • FL 519-661-2028
 Email: auspc@uwo.ca • <http://www.uwo.ca/animal/website/>



2019-116:1:

AUP Number: 2019-116

AUP Title: Hyperpolarized ¹³C MRI of Placental Metabolic Abnormalities Resulting from the Western Diet
Yearly Renewal Date: 02/01/2022

The YEARLY RENEWAL to Animal Use Protocol (AUP) 2019-116 has been approved by the Animal Care Committee (ACC), and will be approved through to the above review date.

Please at this time review your AUP with your research team to ensure full understanding by everyone listed within this AUP.

As per your declaration within this approved AUP, you are obligated to ensure that:

- 1) Animals used in this research project will be cared for in alignment with:
 - a) Western's Senate MAPPs 7.12, 7.10, and 7.15
http://www.uwo.ca/univsec/policies_procedures/research.html
 - b) University Council on Animal Care Policies and related Animal Care Committee procedures
http://uwo.ca/research/services/animalethics/animal_care_and_use_policies.html
- 2) As per UCAC's Animal Use Protocols Policy,
 - a) this AUP accurately represents intended animal use;
 - b) external approvals associated with this AUP, including permits and scientific/departmental peer approvals, are complete and accurate;
 - c) any divergence from this AUP will not be undertaken until the related Protocol Modification is approved by the ACC; and
 - d) AUP form submissions - Annual Protocol Renewals and Full AUP Renewals - will be submitted and attended to within timeframes outlined by the ACC. http://uwo.ca/research/services/animalethics/animal_use_protocols.html
- 3) As per MAPP 7.10 all individuals listed within this AUP as having any hands-on animal contact will
 - a) be made familiar with and have direct access to this AUP;
 - b) complete all required CCAC mandatory training ([%20%20training@uwo.ca] training@uwo.ca); and
 - c) be overseen by me to ensure appropriate care and use of animals.
- 4) As per MAPP 7.15,
 - a) Practice will align with approved AUP elements;
 - b) Unrestricted access to all animal areas will be given to ACVS Veterinarians and ACC Leaders;
 - c) UCAC policies and related ACC procedures will be followed, including but not limited to:
 - i) Research Animal Procurement
 - ii) Animal Care and Use Records
 - iii) Sick Animal Response
 - iv) Continuing Care Visits
- 5) As per institutional OH&S policies, all individuals listed within this AUP who will be using or potentially exposed to hazardous materials will have completed in advance the appropriate institutional OH&S training, facility-level training, and reviewed related (M)SDS Sheets, <http://www.uwo.ca/hr/learning/required/index.html>.

Submitted by: Copeman, Laura
 on behalf of the Animal Care Committee
 University Council on Animal Care

Curriculum Vitae

Name: Lauren M. Smith

Post-secondary Education and Degrees: McMaster University
Hamilton, Ontario, Canada
2012-2016 B.Sc.

The University of Western Ontario
London, Ontario, Canada
2016-2021 Ph.D.

Honours and Awards: National Sciences and Engineering Research Council of Canada
Post Graduate Scholarship - Doctoral
2020-2021

Province of Ontario
Ontario Graduate Scholarship
2020-2021 (declined)

Child Health Research Institute
Graduate Research Fellowship
2019-2020

Mitacs
Globalink Research Award
2018

Related Work Teaching Assistant

Experience

The University of Western Ontario
2019-2020
Quality Assurance Intern
London Regional Cancer Program
2019
Visiting Research Student
Hadassah-Hebrew University Medical Center
2018
Teaching Assistant
McMaster University
2015-2016
Research Student
The Hospital for Sick Children (SickKids)
2013-2015 summers

Publications:

1. Smith, L., Pitts, C., Friesen-Waldner, L., Prabhu, N., Mathers, K., Sinclair, K., Wade, T., Regnault, T., McKenzie, C. (2021). In vivo magnetic resonance spectroscopy of hyperpolarized [1-¹³C]pyruvate in a guinea pig model of life-long Western diet consumption and non-alcoholic fatty liver disease development. *Journal of Magnetic Resonance Imaging*. DOI: 10.1002/jmri.27677.
2. Giza, S., Sethi, S., Smith, L., Empey, M.E., Morris, L., McKenzie C. (2020) The Application of *In-Utero* Magnetic Resonance Imaging in the study of Developmental Origins of Health and Disease. *Journal of Developmental Origins of Health and Disease*. DOI: 10.1017/S2040174420001154.
3. Smith, L., Wade, T., Friesen-Waldner, L., McKenzie, C. (2020) Optimizing signal-to-noise ratio for multi-metabolite hyperpolarized carbon-13 magnetic resonance imaging using a hybrid flip angle scheme. *Magnetic Resonance in Medicine*. DOI:10.1002/mrm.28194.

4. Vidya, P., Smith, L., Beaudoin, T., Yau, Y., Clark, S., Coburn, B., Guttman, D., Hwang, D., & Waters, V. (2015) Chronic infection phenotypes of *Pseudomonas aeruginosa* are associated with failure of eradication in children with cystic fibrosis. *European Journal of Clinical Microbiology & Infectious Disease*. DOI:10.1007/s10096-015-2509-4.

Conference Proceedings:

1. Morris, L., Delhaes, F., Friesen-Waldner, L., Wade, T., Smith L., Empey, M.E., Sethi, S., Regnault T., McKenzie, C. Fetoplacental and Maternal Body Composition Effects of Life Long Western Diet Consumption at Mid-Gestation Guinea Pig Pregnancy. Imaging Network of Ontario 2021. Power pitch presentation at Imaging Network of Ontario (*virtual*) on March 34-24, 2021.
2. Smith, L., McKenzie, C. Investigating *in vivo* pH mapping using hyperpolarized 31-phosphorus magnetic resonance imaging. Poster at 2020 Virtual Joint AAPM|COMP Meeting on July 12-16, 2020.
3. Empey, M.E., Friesen-Waldner, L., Smith, L., Morris, L., Wade, T., de Vrijer, B., Regnault, T., McKenzie, C. Increase in Mid-pregnancy Placental Pyruvate-to-Metabolite Conversion in Guinea Pigs Fed a Lifelong Western Diet. Power pitch at In-Utero MRI Workshop in Oxford, UK on January 8, 2020.
4. Smith, L., Wade T., Rockel, C., Friesen-Waldner, L., McKenzie, C. Optimizing signal-to-noise ratio for hyperpolarized ¹³C fetoplacental MRI using a hybrid flip angle scheme. Poster at London Health Research Day in London, Canada on April 30, 2019.
5. Smith, L., Wade T., Akbari, A., Rockel, C., Friesen-Waldner, L., McKenzie, C. Optimizing signal-to-noise ratio for hyperpolarized carbon-13 magnetic resonance

imaging using a hybrid flip angle scheme. Electronic poster at *Joint Annual Meeting ISMRM-ESMRMB* in Paris, France on June 18, 2018.

6. Smith, L., Friesen-Waldner, L., Sinclair, K., Wade, T., Regnault, T., McKenzie, C. Hyperpolarized carbon-13 MRS of liver in a high-fat/high sugar diet guinea pig model. Electronic poster at *Joint Annual Meeting ISMRM-ESMRMB* in Paris, France on June 18, 2018.

7. Friesen-Waldner, L., Rockel, C., Sinclair, K., Wade, T., Smith, L., Moselhy, M., Vander Tuin, C., Chen, A., de Vrijer, B., Regnault, T., McKenzie, C. Hyperpolarized [1-¹³C]Pyruvate Magnetic Resonance Imaging of Placentae Associated with Intrauterine Growth Restriction. Power pitch at *Joint Annual Meeting ISMRM-ESMRMB* in Paris, France on June 18, 2018.

8. Pitts C., Smith, L., Mathers, K., Friesen-Waldner, L., Vander Tuin, C., McKenzie, C., Regnault, T. The hepatic metabolic signature and outcomes of lifelong exposure to Western Diet in young adult guinea pigs. Poster presentation at London Health Research Day in London, Canada on May 10, 2018.

9. Smith, L., Wade T., Akbari, A., Rockel, C., Friesen-Waldner, L., McKenzie, C. Optimizing signal-to-noise ratio for hyperpolarized carbon-13 MRI of the placenta. Oral presentation at Imaging Network of Ontario in *Toronto, Canada* on March 29, 2018.

10. Smith, L., Wade T., Akbari, A., Rockel, C., Friesen-Waldner, L., McKenzie, C. Optimizing Hyperpolarized Carbon-13 Magnetic Resonance Imaging of the Placenta using a Hybrid Flip Angle Scheme. Oral presentation at ISMRM Workshop on MRI of the Placenta in Atlanta, USA on February 6, 2018.

11. Friesen–Waldner, L., Rockel, C., Sinclair, K., Wade, T., Smith, L., Moselhy, M., Vander Tuin, C., Chen, A., de Vrijer, B., Regnault, T., McKenzie, C. Hyperpolarized [1- ^{13}C]Pyruvate Magnetic Resonance Imaging of Placentae Associated With Intrauterine Growth Restriction. Oral presentation at ISMRM Workshop on MRI of the Placenta in Atlanta, USA on February 5, 2018.
12. Friesen-Waldner, L., Rockel, C., Sinclair, K., Wade, T., Smith, L., Moselhy, M., Vander Tuin, C., Chen, A., de Vrijer, B., Regnault T., McKenzie, C. Hyperpolarized Carbon-13 Magnetic Resonance Imaging Detects Multiple Pyruvate Metabolism Pathways Simultaneously in Placenta. Poster presentation at the 4th Annual Meeting of The Human Placenta Project in Bethesda, USA on July 24-25, 2017.
13. Smith, L., Akbari, A., Wade T., McKenzie, C. Comparing Constant and Variable Flip Angle Schemes with Error Effects for Hyperpolarized Carbon-13 Magnetic Resonance Imaging. Poster presentation at London Health Research Day in London, Canada on March 28, 2017.
14. Smith, L., Akbari, A., Wade T., McKenzie, C. Optimizing Hyperpolarized Carbon-13 Magnetic Resonance Imaging of Fetoplacental Metabolism. Poster presentation at the 15th Annual Imaging Network of Ontario Symposium in London, Canada on March 15-16, 2017.
15. Fradin, C., Barkley, C., Smith, L., Nadkarni, R., Hashmi, M. Taking the Temperature of Rotating Magnetotactic Bacteria. Oral presentation at 5th Annual International Magnetotactic Bacteria Meeting in Marseille, France on September 13, 2016.